7-12-2014

Development of Novel Synthetic Methods for Size-Tunable Synthesis of Superparamagnetic Iron Oxide Nanoparticles

Erika Vreeland

Erika Cooley Vreeland

Candidate

Chemical Engineering

Department

This thesis is approved, and it is acceptable in quality and form for publication:

Approved by the Thesis Committee:

Plamen B. Atanassov , Chairperson

Abhaya K. Datye

Natalie L. Adolphi

Dale L. Huber

DEVELOPMENT OF NOVEL SYNTHETIC METHODS FOR SIZE-TUNABLE SYNTHESIS OF SUPERPARAMAGNETIC IRON OXIDE NANOPARTICLES

by

ERIKA COOLEY VREELAND

B.S., Animal Physiology and Neuroscience,
University of California at San Diego, 1996

DISSERTATION

Submitted in Partial Fulfillment of the
Requirements for the Degree of

Doctor of Philosophy
Engineering

The University of New Mexico
Albuquerque, New Mexico

May, 2014

DEDICATION

I dedicate this work to my long-suffering husband, David, and to my little daughter Selah, who have steadfastly supported and inspired me for the duration of this journey. This dedication is also shared with my family, especially my parents, who instilled a love of science in me from an early age and taught me to persevere though adversity, or as my father often succinctly put it, “Suffer!”

ACKNOWLEDGEMENTS

I owe a great deal of gratitude to my research advisor at Sandia National Laboratories, Dr. Dale Huber, whose expertise, insights, and patience made this research possible. I am extremely grateful to Dr. Huber for the countless hours he dedicated to helping me develop a thorough understanding of this subject matter and helping me acquire the skills necessary to become an independent scientist.

I would like to thank my advisor at the University of New Mexico and the Chairperson of my dissertation committee, Professor Plamen Atanassov, who convinced me to join the Ph.D. program in Chemical Engineering and has provided unwavering support and guidance ever since. The combination of Professor Atanassov's knowledge and charisma has made him a superior teacher and mentor.

I gratefully acknowledge my committee members, Professor Abhaya Datye, from whom I developed a solid foundation in the underlying thermodynamics that governs much of this body of work, and Professor Natalie Adolphi, whose research in this field has emphasized the need to improve the current state of magnetite nanoparticle synthesis for translation into clinical use.

This research could not have been completed without the cooperation of the members of the Huber lab and its collaborators. I especially want to thank Gretchen Schober, who spent several years as an undergraduate contributing to this project. Gretchen's diligent and meticulous nature helped reveal many

interesting my aspects of this work. Dr. Andrew Price and Dr. John Watt made technical and creative contributions that led to the overall success of this project, and were always willing to lend an ear and provide objective comments at various stages of the research. Ben Fellows put a number of late hours into helping me collect experimental data and provided a constant outlet for my sarcasm and banter. Brad Hance is an all-around Renaissance Man who engineered a number of devices that brought greater efficiency to our laboratory work, including the molten metal bath that I describe in later chapters. Mariah Austin was always willing to help analyze TEM images. Rachel, Grant, Jolie, and Chet – thank you for your friendship. I want to thank Dr. Todd Monson for his friendship and for the time spent teaching me the fundamentals and interpretation of SQUID magnetometry. Dr. Monson and Paula Provencio taught me a great deal about TEM imaging, and even in retirement, Paula has always been willing to provide support. I also want to thank Dr. Sergei Ivanov and Dr. Jeffrey Crisp for their mentorship and for sharing their knowledge of synthetic methods, characterization techniques, and data interpretation.

Prior to joining the Huber lab, the National Science Foundation provided me with an Integrative Graduate Education Research and Training (IGERT) fellowship that gave me the opportunity to work at Sandia National Laboratories and the University of New Mexico through a series of laboratory rotations, and the University of Texas at Austin for a six month internship.

At Sandia National Laboratories, I had the privilege of working under the mentorship of Dr. Darren Branch, Dr. Conrad James, and Dr. Susan Brozik, where I learned how device engineering could address issues relevant to biomedical research, such as disease detection, the development of neural pathways, and developing models of infectious disease. At the University of New Mexico, I worked under the guidance of Professor Jim Brozik where I first learned the principles of Raman and FTIR spectroscopy for probing the properties of organic compounds. In a separate lab rotation, I worked under the combined guidance of Dr. Kimberly Leslie and Professor Charlotte Mobarak at the Cancer Research Facility, where I gained experience with proteomic techniques being developed for rapid screening of endometrial cancer.

At the University of Texas at Austin, I worked under the supervision of Professor Stanislav Emelianov in the Ultrasound Imaging and Therapeutics Research Laboratory. Professor Emelianov's research in photoacoustic imaging showed me the enormous potential of nanotechnology in developing new diagnostic and therapeutic modalities. I will always be grateful to the Professor Emelianov and the members of the lab, especially Dr. Kimberly Homan and Pieter Kruizinga, for their friendship, guidance, and support during my internship. Ultimately, my experience at UT Austin shaped my desire to develop new nanomaterials for biomedical applications.

Finally, I want to thank my friends, who supported me through all of the ups and downs of this process!

The body of research described in this dissertation was supported by the U.S. Department of Energy, Office of Basic Energy Sciences, Division of Materials Science and Engineering. HRTEM imaging and XRD/SAXS measurements were performed courtesy of the Center for Integrated Nanotechnologies, a U.S. Department of Energy, Office of Basic Energy Sciences user facility. Sandia National Laboratories is a multi-program laboratory managed and operated by Sandia Corporation, a wholly owned subsidiary of Lockheed Martin Corporation, for the U.S. Department of Energy's National Nuclear Security Administration under Contract DE-AC04-94AL85000.

DEVELOPMENT OF NOVEL SYNTHETIC METHODS FOR SIZE-TUNABLE GROWTH OF HIGH QUALITY SUPERPARAMAGNETIC IRON OXIDE NANOPARTICLES

by

Erika Cooley Vreeland

B.S., Animal Physiology and Neuroscience,
University of California at San Diego, 1996

Ph.D., Engineering, University of New Mexico, 2014

ABSTRACT

The properties of magnetic nanoparticles vary dramatically with size, so reproducibly controlling size is critical for practical applications. This is particularly true when moving into clinical settings, where regulatory approval requires demonstrated reproducibility in efficacy that can only be achieved with excellent size control.

A number of methods for the synthesis of magnetic nanoparticles have been published, although the thermal decomposition of iron(III) precursors in organic solvents has been shown to yield high quality particles with low shape and size dispersity. Currents methods lack reproducibility resulting from non-stoichiometric starting materials, and reliance on reaction parameters, such as temperature ramp rate, that are nearly impossible to replicate between syntheses. Limited control of

particle size has been demonstrated, though no truly size-tunable synthetic method has been proposed. Here, we endeavor to remove the sources of reproducibility in the existing methods and achieve size control of synthesized particles while maintaining narrow shape and size dispersity. Further, we endeavor to understand the physical mechanisms by which the control of size is achieved.

Here, we detail two alternative approaches to the synthesis of an iron(III) precursor containing a known quantity of iron. These materials are further evaluated for use in the preparation of high quality iron oxide nanoparticles with high magnetic saturation values. Existing synthesis methods are also evaluated, leading to the development of a novel synthetic method that yields tunability of sizes over a broad range with nanometer precision and nearly uniform size and shape dispersity. By manipulating reaction parameters such as temperature and reagent concentration, the kinetics of the reaction can be controlled, revealing new insights into the growth of particles in a highly supersaturated monomer solution.

We expect that our approach will resolve the challenges associated with the reproducible synthesis of spherical magnetite nanoparticles with low shape and size dispersity, and provide scalability required to meet commercial demand.

TABLE OF CONTENTS

LIST OF FIGURES

LIST OF TABLES

SYMBOLS AND ABBREVIATIONS

Symbol	Unit	Property
a	Å	lattice parameter
A		the pre-exponential factor in the Arrhenius equation
B	T	magnetic induction
χ	dimensionless	volume susceptibility
χ_ρ	cm^3/kg	mass susceptibility
C	$cm^3 \cdot K/g$	Curie constant per unit mass
C	mol/L	concentration
	C_0	the equilibrium concentration of the monomer species in the bulk crystal
	C_b	the concentration of monomer in bulk solution
	C_i	the concentration of the monomer species at the liquid/solid interface
	C_∞	the solubility of a bulk crystal with infinite dimensions
	C_{max}	In the LaMer mechanism, this is supersaturation limit
	C_{min}	In the LaMer mechanism, this represents the critical supersaturation limit required for nucleation to occur
	C_r	the solubility of a particle with radius r
	C_s	In the LaMer mechanism, this is the lower solubility limit of the monomer species
δ	nm	diffusion layer thickness
d	nm	diameter
d_p	μm	in ATR, the penetration depth of the evanescent wave into the sample

Symbol	Unit	Property
D	cm^2/s	temperature dependent diffusion coefficient
E_a	J	activation energy
γ	J/m^2	surface energy per unit area of a particle surface
ΔG	J/mol	the free energy change within a system
	ΔG_V	the difference between the free energy of the monomer in the nucleus and in the solution
η	Pa·s	dynamic viscosity
H	A/m	magnetic field (strength), sometimes given as $\mu_0 H$ in tesla (T)
	H_C	coercive field
I	various units	intensity
J	mol/m^2	in Fick's law, this is the flux of monomer through the diffusion layer
k_B	J/K	Boltzmann constant
k_d	s^{-1}	rate constant for a simple first order deposition reaction
K	J/m^3	anisotropy constant
K_D	m^3/s	in the LSW theory describing diffusion controlled growth, this is a constant given by $\frac{8\gamma D V_m^2 C_\infty}{9RT}$
K_r	m^2/s	in the LSW theory describing surface reaction limited growth, this is a constant given by $\frac{2\gamma V_m^2 C_\infty}{RT}$
λ	Å	electromagnetic wavelength
μ	J/mol	chemical potential
	$\mu°$	the chemical potential of the bulk crystal
	$\mu(r)$	chemical potential of a particle with radius r

Symbol	Unit	Property
μ_0	dimensionless in cgs units	permeability
m	A·m^2	magnetic moment
M	A/m, G	magnetization
	M_R	remnant magnetization
	M_S	saturation magnetization
ν	cm^{-1}	vibrational frequency, wavenumber
n		refractive index
N		nuclei
θ	degrees	angle of incidence
	θ_C	critical angle in ATR
q	1/Å	scattering vector
ρ	g/mL	density
r	nm	radius
	$\bar{r}$	mean particle radius
	r^*	the critical nucleus size
	r_b	the particle radius in equilibrium with the bulk solution
R	J/mol·K	universal gas constant
σ	A·m^2/kg	magnetization per unit mass
	σ_{sat}	saturation magnetization per unit mass
τ_0	s	attempt time
τ_B	s	Brownian relaxation time

Symbol	Unit	Property
τ_N	s	Neel relaxation time
t	s, min, h	time
T	K, °C	temperature (K)
	T_B	blocking temperature
	T_C	Curie temperature
	T_N	Neel temperature
V	nm^3, m^3	volume
	V_h	hydrodynamic volume
V_m	m^3/mol	Molar volume of a monomer species
x	nm	distance

Abbreviation	Meaning
ATR	attenuated total reflectance
CVD	chemical vapor deposition
DC	direct current
DTGS	deuterated triglycine sulfate pyroelectric IR detector
FC	field-cooled magnetization
$Fe_{1-x}O$	wüstite
γ-Fe_2O_3	maghemite
Fe_3O_4	magnetite
$Fe(acac)_3$	Iron(III) acetylacetonate

Abbreviation	Meaning
FTIR	Fourier transform infrared spectroscopy
GATR	grazing angle attenuated total reflectance
HRTEM	high resolution transmission electron microscopy
ICDD	International Center for Diffraction Data
IR	infrared
LSW	Lifshitz-Slyozov-Wagner theory
MCT	mercury cadmium telluride photoconductive IR detector
MRI	magnetic resonance imaging
PID	proportional-integral-derivative controller
SAXS	small angle X-ray scattering
SQUID	superconducting quantum interference device
TEM	transmission electron microscopy
XRD	X-ray diffraction
ZFC	zero-field cooled magnetization

Chapter 1 – Fundamental Aspects

1.1 Introduction

Nanoscience encompasses an emerging area of research concerning the study of objects with dimensions ranging from 1 – 100 nanometers[1]. Nanoscale phenomena are not new to either nature or science, but recent advances in instrumentation and analytical techniques have provided scientists with the tools required to understand and exploit their behavior. In essence, these phenomena are based on quantum effects that reflect the properties of atoms and molecules that are obscured by classical behavior of materials at the macroscopic level[2]. These effects, combined with physical effects such as a high surface-to-volume ratio, produce chemical, mechanical, electronic, optical, and magnetic properties unique with respect to those seen in the bulk material[3-7]. Thus, a great deal of research has been devoted to controlling the size, morphology, structure, and composition of nanomaterials as a mechanism for tuning their unique properties[4, 8, 9]. Nanomaterials have found broad applications in catalysis[10], fuel cells[11], photonics[12], pollution remediation[13], and biotechnology[14-16], among others.

In spite of the implications of nanotechnology, an increasing amount of attention has been focused on the lack of standards in place for characterizing nanomaterials, their purity, and synthetic reproducibility[17-20]. This body of research aims to address these challenges as they apply to magnetite nanoparticle synthesis.

Nanoscale magnetite possesses unique magnetic properties that have found particular utility in biomedical research[21-23]. Ultimately, the physicochemical properties and resulting usefulness of the particles depends strongly on their size. Achieving precise shape and size control of the particles presents a challenge, but improvements to the state of the art have the potential to significantly improve their practical use, particularly in biomedical diagnostics[24].

In this chapter, current methods of magnetite nanoparticle synthesis and classical models of nanoparticle nucleation and growth are presented. The classes of magnetism are reviewed, followed by a brief discussion of the properties of iron oxides encountered in this research. The chapter is concluded with a description of specific biomedical applications.

1.2 Synthetic methods

A number of routes for the synthesis of magnetic nanoparticle have been published, although only the most representative examples will be presented here. The methods generally fall into one of three categories: particle size reduction in the solid phase, vapor phase synthesis, or liquid phase synthesis. Particular focus will be given to those methods that are reported to yield nanomaterials with uniform shape and size dispersity. For clarity, NIST defines a population of nanoparticles as monodisperse if at least 90% of the distribution lies within 5% of the median size[25]. However, the Polymer Division of IUPAC regards the term “monodispersed” as a self-contradictory term and “polydisperse” as redundant[26].

For this research, the description of particle size distribution will be referred to as size dispersity, in accordance with the IUPAC recommendations.

1.2.1 Solid phase synthesis

In the solid phase, high-energy ball milling has been used for the generation of magnetic[27], catalytic[28], and structural nanoparticles[29]. While this process benefits from scalability for large scale manufacturing of nanoparticles, common drawbacks include low surface area, high size dispersity, and the partially amorphous state of the as-prepared powders[30].

1.2.2 Vapor phase synthesis

Vapor phase syntheses include chemical vapor deposition (CVD) and aerosol spray methods such as spray pyrolysis. CVD synthesis is used to deposit thin films of Fe_3O_4 for use in spintronic devices such as magnetic tunnel junctions and magnetoresistive sensors[31]. In the spray pyrolysis technique, a precursor solution is dispersed as droplets into a carrier gas and then sprayed into a drying chamber. The drying chamber is heated above the vaporization temperature of the carrier solvent, and solid particles are collected. A number of ordered porous metal oxide particles have been prepared using this method, including iron oxides[32], silica, titania, alumina, zirconia, and yttria[33]. The scalability and high purity yield make spray pyrolysis an attractive option for high throughput manufacturing applications, but because the rate of particle formation cannot be easily controlled, aggregation of particles and a large size dispersity often result[34].

1.2.3 Liquid phase synthesis

Several solution methods have been reported for synthesis of high quality magnetite nanoparticles, some of the most common being aqueous co-precipitation, microemulsion, hydrothermal synthesis, and thermolysis. A brief discussion of each method is presented, with the merits of each approach summarized in Table 1-1.

1.2.3.1 Aqueous co-precipitation

Aqueous co-precipitation offers a facile, room temperature method for synthesizing iron oxide nanoparticles by aging a stoichiometric mixture of ferrous and ferric salts in aqueous media under basic conditions. This synthesis can yield a large amount of material, and some control over particle size and shape has been demonstrated by adjusting pH, ionic strength and the concentration of the growth solution. However, particles prepared in this fashion tend to have a high degree of asphericity and large size dispersity[35], making this approach unattractive for the purposes described previously.

1.2.3.2 Microemulsion

The microemulsion technique offers synthesis of nanoparticles in a controlled manner. Microemulsions are stable dispersions containing two immiscible phases that are separated by an interfacial surfactant layer[36]. A water-in-oil microemulsion is made up of water droplets surrounded by a surfactant and dispersed in oil, forming an inverse micelle. The size of the inverse micelle is determined by the

molar ratio of water to surfactant, and can form spherical, oblate, or tubular shapes[36, 37]. For the synthesis of nanoparticles, two water-in-oil microemulsions, one containing a metal salt and the other a reducing agent, are combined. Upon mixing, the continuous collision, coalescence, and separation causes precipitation of the metal salt, the formation of nuclei, and the growth of particles. The primary drawbacks of the microemulsion technique are the inability to systematically control nanoparticle size and the low product yield[35].

1.2.3.3 Solvothermal

Under thermolytic conditions, particles are synthesized by combining the precursor, solvent, and a stabilizing surfactant in a Teflon-lined, stainless-steel autoclave and performing a high temperature, high pressure reaction. The reaction is conducted above the boiling point of the solvent and the temperature, and typically maintained for 8 – 72 hours[38]. Shape and size control can be accomplished by altering the surfactant used, but synthesized particles generally suffer from high size dispersity[38-40].

1.2.3.4 Thermolysis

Formation of metal oxide nanoparticles by thermolysis provides an approach by which very good shape and size control, along with narrow size dispersity, can be achieved. The precursor is either an inorganic metal salt or an organometallic compound such as a metal carboxylate or acetylacetonate[41, 42]. Thermal decomposition of the metal precursor occurs in a high boiling point solvent, often

at temperatures at or above 300°C. Control of nanoparticle morphology, size, and size dispersity is determined by the surfactant used in the system[43]. Typically, long-chain fatty acid molecules prevent agglomeration during synthesis and result in good colloidal stability of the product in organic solvents. There are a number of advantages to thermolytic synthesis, including good crystallinity, narrow size distribution, and shape control[43-45].

Table 1-1. Summary of liquid-phase synthetic methods. Adapted from [35].

Method	Reaction Temp. (°C)	Solvent	Shape Control	Size Control	Size Dispersity
Co-precipitation	20 – 90	Water	Poor	Poor	Large
Hydrothermal	220	Water-Ethanol	Very good	Poor	Very narrow
Microemulsion	20 – 50	Organic	Good	Good	Relatively narrow
Thermolysis	200 - 350	Organic	Very good	Very good	Very narrow

1.3 Homogeneous nucleation and growth of nanoparticles

1.3.1 LaMer mechanism

In 1950, LaMer and Dinegar introduced a mechanistic pathway to explain the formation and growth of elemental sulfur colloids[46]. The 'LaMer mechanism' describes a closed system where nanoparticle formation and growth depends on monomer concentration. Distinct stages, corresponding to pre-nucleation, nucleation, and growth, can be identified.

In phase I, the monomer species increases until a critical supersaturation limit (C_{min}) is reached. In phase II, burst nucleation occurs, partially relieving the supersaturation condition and reducing the concentration of the monomer below the threshold for nucleation. In phase III, growth proceeds by diffusion of the monomer to the particle surface until the concentration of the monomer species reaches the lower limit of solubility.

The importance of the LaMer mechanism was that it established the requirement for temporal separation of the elementary steps of nucleation and growth to ensure low size dispersity. In other words, if the nuclei form in a single event of finite duration, and the system is well-mixed so that all nuclei experience the same concentration of monomer species as they grow, the system will have low size dispersity.

Stage IV in Figure 1-1 incorporates the Ostwald ripening into the LaMer mechanism, illustrating the change in the particle suspension over time, whereby

smaller particles dissolve and redeposit onto larger particles. The Ostwald ripening phenomenon describes the minimization of total interfacial energy that drives the competitive growth between particles of different sizes. The relation between the chemical potential of a particle and its radius is given by the Gibbs-Thomson equation. If μ° represents the chemical potential of the bulk crystal and $\mu(r)$ the chemical potential of a particle with radius r, their difference is $\Delta\mu$:

$$\Delta\mu = \frac{2\gamma V_m}{r} \tag{1-1}$$

γ is the surface energy per unit area of the particle surface and V_m is the molar volume of the monomer species.

Equation (1-1) demonstrates mathematically the dominant role of surface energy with decreasing particle size, thus driving the dissolution of smaller particles in favor of growth of larger particles. While Ostwald ripening is one technique to increase the average size of particles in a sample, it is often undesirable compared to growth from a continuous flux of molecular precursors, as will be explored in the following sections.

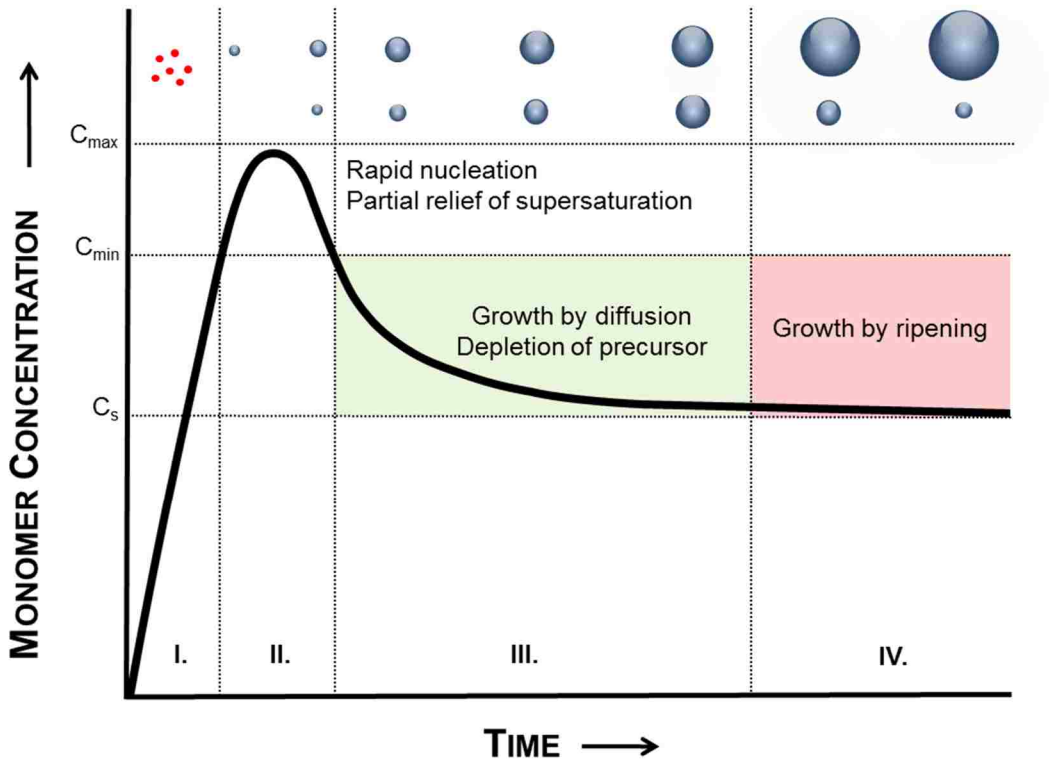

Figure 1-1. The LaMer mechanism. In phase I, the concentration of monomer species increases until a critical supersaturation concentration (C_{min}) is reached. Burst nucleation occurs in phase II, which partially relieves the supersaturation condition, and the concentration of monomer species drops below the nucleation threshold. In phase III, growth of the nuclei takes place by diffusion of the monomer species to the surface of the particle, until it is depleted, indicated by C_s, the lower limit of solubility of the monomer in solution. In phase IV, additional particle growth takes place by ripening processes. The spheres above the diagram represent the evolution of particle size dispersity. Adapted from [46].

1.3.2 Classical Nucleation Theory

In a supersaturated solution, nucleation can be considered as the phase transition of a monomer from a supersaturated solution to a crystal. Because a supersaturated solution possesses a high Gibbs free energy, the overall energy of the system can be reduced by segregating the solute from solution by forming a second, solid phase and maintaining an equilibrium concentration in the solution. The change in free energy is based on two competing factors: the creation of surface energy, γ, per unit area of the particle surface and the change free energy per unit volume of the particle[47, 48]:

$$\Delta G = 4\pi r^2\gamma + \frac{4}{3}\pi r^3 \Delta G_V \tag{1-2}$$

The first term in equation (1-2) is always positive, while the second term is negative under conditions of supersaturation, providing the driving force for nucleation. ΔG_V can be expressed as the difference between the free energy of the monomer in the nucleus and in the solution[48, 49]:

$$\Delta G_V = \frac{RT(lnC_b - lnC_0)}{V_m} \tag{1-3}$$

where C_b represents the concentration of the monomer in solution, C_0 is the equilibrium concentration in the bulk crystal, and V_m is the molar volume of the monomer. When the concentration of the solute is not supersaturated ($C \leq C_0$), ΔG_V is ≤ 0, and nucleation does not occur. When $C > C_0$, ΔG_V is negative and nucleation can take place spontaneously. However, the nucleus is only stable when its size

is greater than the critical nucleus size, r^*, with the following relationship between r^*, ΔG_V, and γ[47]:

$$r^* = \frac{2\gamma}{\Delta G_V} \tag{1-4}$$

In the synthesis and preparation of nanoparticles by nucleation from a supersaturated solution, the critical size (r^*) represents the lower limit of a stable nanoparticle. By increasing the temperature and particularly the supersaturation the minimum size of the nuclei can also be decreased.

The rate of nucleation can then be written in the form of Arrhenius kinetics[48]:

$$\frac{dN}{dt} = Aexp\left[-\frac{\Delta G_V}{k_B T}\right] \tag{1-5}$$

where N is the number of nuclei, A is the pre-exponential factor, k_B is the Boltzmann constant, and T is the temperature.

1.3.3 Growth of nanoparticles

Following the nucleation event, the critical nuclei must gather monomer species from the surrounding matrix, requiring long-range diffusion from the solution to particle surface. When the kinetics of diffusion are the slowest step in the growth of the nanoparticles, the process is considered diffusion limited. The particle can then grow by incorporating atoms or molecules into its solid structure over a short range of molecular motion. In the case where the surface reaction kinetics are slower than the diffusion process, the growth of particles can be considered reaction limited. Here, a model for nanoparticle growth is developed using Fick's

law of diffusion. Appropriate boundary conditions can then be applied to describe the growth kinetics in either diffusion or reaction limited growth.

In a supersaturated solution, assuming the monomer species is present in uniform concentration (C_b), it will diffuse from the bulk liquid phase to the surface of a particle with radius r through a diffusion layer to the liquid/solid interface (C_i)[48, 50], as shown in Figure 1-2.

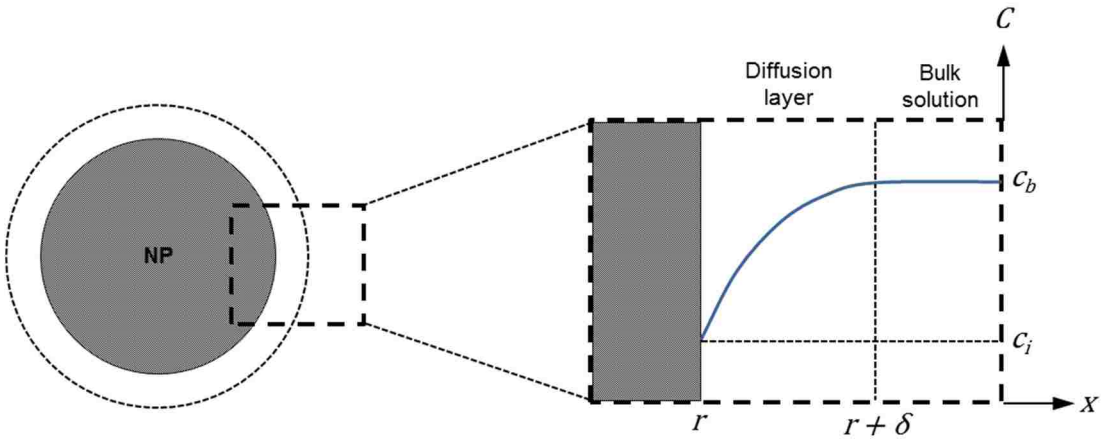

Figure 1-2. Left: schematic illustration of the diffusion layer near a nanoparticle (NP) with the dashed line indicating the diffusion layer of thickness δ. Right: The plot of the monomer concentration as a function of x. Adapted from [48, 50].

The flux of the monomer species through the diffusion layer can be described by Fick's law[48, 50, 51]:

$$J = -D\frac{dC}{dx} \tag{1-6}$$

where J is the monomer flux and D is the temperature dependent diffusion coefficient given by $D_0 \exp(-E_A/k_bT)$ in cm^2/s.

The rate of diffusion of the monomer through a spherical surface with radius x within the diffusion layer is:

$$J = -4\pi x^2 D \frac{dC}{dx} \tag{1-7}$$

At steady state, J is constant for all x. Dividing both sides by x^2, equation (1-7) can be integrated from r to $r + \delta$ and from C_i to C_b for the left and right hand sides, respectively gives[48, 50, 51]:

$$J = \frac{4\pi D r(r+\delta)}{\delta}(C_b - C_i) \tag{1-8}$$

This consumption rate of the monomer at the surface of the particle with solubility C_r is equal to the monomer flux, as expressed by:

$$J = 4\pi r^2 k_d (C_i - C_r) \tag{1-9}$$

where k_d is the rate constant for a simple first order deposition reaction. By equating (1-8) with (1-9), C_i can be eliminated and a linear expression for the growth rate can be obtained assuming that $dr/dt = JV_m/4\pi r^2$:

$$\frac{dr}{dt} = \frac{\frac{D}{r}\left(1+\frac{r}{\delta}\right)V_m(C_b - C_r)}{1+\frac{D}{k_d r}\left(1+\frac{r}{\delta}\right)} \tag{1-10}$$

where V_m is the molar volume of the monomer species.

The terms C_b and C_r are related to the particle radius, r, by the Gibbs-Thomson equation:

$$C_r = C_\infty \exp\left(\frac{2\gamma V_m}{rRT}\right) \approx C_\infty\left(1+\frac{2\gamma V_m}{rRT}\right) \tag{1-11}$$

where C_∞ is the solubility of a bulk crystal with infinite dimensions. R is the universal gas constant and T is the temperature. The expression on the right is obtained from the expansion of the exponential function and retention of the first two terms, assuming of a small value of $2\gamma V_m/rRT$[51].

Similarly, C_b can be expressed as:

$$C_b = C_\infty \exp\left(\frac{2\gamma V_m}{r_b RT}\right) \approx C_\infty \left(1 + \frac{2\gamma V_m}{r_b RT}\right) \quad (1\text{-}12)$$

where r_b is the particle radius in equilibrium with the bulk solution.

Diffusion layers are typically on the order of microns, so the assumption can be made that $r \ll \delta$[48, 50, 51]. Substituting (1-11) into (1-12) gives:

$$\frac{dr}{dt} = \frac{2\gamma V_m^2 C_\infty}{RT\left(\frac{1}{D} + \frac{1}{k_D r}\right)} \frac{\left(\frac{1}{r_b} - \frac{1}{r}\right)}{r} \quad (1\text{-}13)$$

Equation (1-13) can now be modified to develop a model of nanoparticle growth in the diffusion limited or reaction limited growth regime.

1.3.3.1 Diffusion limited growth

In 1961, Lifshitz and Slyozov and Wagner developed a mathematical approach to account for the effect of Ostwald ripening on the evolution of particle size distribution where diffusion of the monomer species is the rate limiting step[52, 53]. Their combined work is well known as the Lifshitz-Slyozov-Wagner (LSW) theory, which describes the growth of non-interacting, spherical clusters in a

supersaturated solution. In the diffusion limited growth regime, $D \ll k_D r$ in equation (1-13), reducing it to[50, 51]:

$$\frac{dr}{dt} = \frac{2\gamma V_m^2 C_\infty}{RT} \frac{\left(\frac{r}{r_b} - 1\right)}{r^2} = K_D \frac{\left(\frac{r}{r_b} - 1\right)}{r^2} \quad (1\text{-}14)$$

where K_D is a constant, given by $2\gamma D V_m^2 C_\infty / RT$. The LSW theory assumes that the mass of the clusters is conserved, making r/r_b a constant, giving[52]:

$$\frac{dr}{dt} = \frac{K_D * \text{constant}}{r^2} \quad (1\text{-}15)$$

which can be solved to determine the dependence of particle size on time. Applying the boundary conditions that $x = r_0$ at $t = 0$ and $x = r$ at $t_\infty = t$. This relationship is given by[51, 52]:

$$r^3 - r_o = K_D t \quad (1\text{-}16)$$

where K is given by:

$$K_D = \frac{8\gamma D V_m^2 C_\infty}{9RT} \quad (1\text{-}17)$$

The LSW theory provides a straightforward, yet robust approach to model the kinetics of particle growth, and has been applied to a diverse range of systems. This includes precipitate hardening in in Cu-Co[54] and Ni-Fe[55] alloys, growth of TiO_2[56] and ZnO semiconductor[57] nanoparticles in solution, and sintering of supported Pd[58, 59] and Ni[60] catalysts.

1.3.3.2 Reaction limited growth

When incorporation of the monomer species into the structure of the particles is the slowest step in the growth process, $k_D r \ll D$ and equation (1-13) becomes[50, 51]:

$$\frac{dr}{dt} = \frac{2\gamma k_d V_m^2 C_\infty}{RT} \frac{\left(\frac{r}{r_b} - 1\right)}{r^2} = K_R \frac{\left(\frac{r}{r_b} - 1\right)}{r} \quad (1\text{-}18)$$

Applying the same assumption that mass of the monomer is conserved, r/r_b = 1, and equation (1-18) can be reduced as before to give the dependence of particle size on time[50, 51]:

$$r^2 \approx K_r t \quad (1\text{-}19)$$

where K_r is a constant, given by:

$$K_r = \frac{2\gamma V_m^2 C_\infty}{RT} \quad (1\text{-}20)$$

1.3.3.3 Evolution of the size distribution

Since the diffusion-controlled growth is observed when the surface reaction rate constant is so high that the growth rate is limited by the diffusion rate of the solute to the particle, it is the growth mode with the maximum conceivable growth rate.

The diffusion limited growth rate of the nanoparticle radius derived in equation (1-14) can expressed in an equivalent form as:

$$\frac{dr}{dt} = \frac{K_D}{r}\left(\frac{1}{r_b} - \frac{1}{r}\right) \quad (1\text{-}21)$$

Under the assumption of a constant r_b, the rate of change of the standard deviation of the size distribution, $d(\Delta r)/dt$, is[61]:

$$\frac{d(\Delta r)}{dt} = \frac{K_D \Delta r}{\bar{r}^2}\left(\frac{2}{\bar{r}} - \frac{1}{r_b}\right) \tag{1-22}$$

where $\bar{r}$ is the mean particle radius. From this equation, it is apparent that the Gibbs-Thomson effect becomes negligible as particle size increases.

We then arrive at:

$$\begin{aligned} \frac{d(\Delta r)}{dt} &> 0 \quad \text{for} \quad \frac{\bar{r}}{r_b} < 2, \\ \frac{d(\Delta r)}{dt} &\leq 0 \quad \text{for} \quad \frac{\bar{r}}{r_b} \geq 2. \end{aligned} \tag{1-23}$$

Thus, under conditions of low supersaturation, the size distribution becomes broader, even when the growth of particles is occurring in the diffusion controlled mode. If supersaturation is kept sufficiently high, focusing of the size distribution will occur. For low size-dispersity in the diffusion controlled growth mode, supersaturation should be set as high as possible without exceeding the threshold for nucleation[61].

For the case of simple, first-order reaction-controlled growth of particles, equation (1-18) can be expressed as:

$$\frac{dr}{dt} = K_R\left(\frac{1}{r_b} - \frac{1}{r}\right) \tag{1-24}$$

and,

$$\frac{d(\Delta r)}{dt} = \frac{K_D \Delta r}{\bar{r}^2} \tag{1-25}$$

From (1-25), it is apparent that $d(\Delta r)/dt$ is positive for all r, so that an increase of the size distribution results from the Gibbs-Thomson effect, although it becomes less pronounced as $\bar{r}$ increases. The size distribution is independent of r_b, so the broadening effect will occur regardless of the level of supersaturation[50, 61].

Clearly, it is preferable to choose the diffusion controlled growth mode for a given system, since a sharpening of the size distribution can be expected as long as a high level of supersaturation is maintained. In practice, however, particle growth may result from a combination of diffusion and reaction limited growth[51].

1.4 Magnetism

To understand the unique magnetic properties of materials at the nanoscale, it is important to review the general forms and magnetism and the associated nomenclature that will be referred throughout this study.

When a material is placed within a magnetic field, the magnetic forces of the electrons within a material will be affected, as described by Faraday's Law of magnetic induction. However, materials will respond quite differently to the external field based on their atomic and molecular structure. For instance, in most atoms, electrons occur in pairs. Because paired electrons spin in opposite directions, their magnetic fields cancel each other and little net magnetic moment exists. Alternatively, in materials with unpaired electrons, there will be a net magnetic moment and the material will have a greater response to an external field. Based on their behavior in an applied magnetic field, materials can be

classified as diamagnetic, paramagnetic, ferromagnetic, antiferromagnetic, ferrimagnetic and superparamagnetic. Table 1-2 lists common magnetic units useful for this study. SI units will be used to describe magnetic properties in this work, but because cgs units are often reported in the literature, their equivalent units are also shown.

Table 1-2. Magnetic properties, the symbols used to represent them, and the SI and CGS units with the corresponding conversion factors. From [62].

Magnetic Term	**Symbol**	**SI Unit**	**CGS Unit**	**Conversion Factor**
Magnetic induction	B	Tesla (T)	Gauss (G)	1 T = 10^4 G
Magnetic field	H	A/m	Oersted (Oe)	1 A/m = $4\pi/10^3$ Oe
Magnetization	M	A/m	emu/cm^3	1 A/m = 10^{-3} emu/cm^3
Mass Magnetization	σ	A·m^2/kg	emu/g	1 A·m^2/kg = 1 emu/g
Magnetic moment	m	A·m^2	emu	1 A·m^2 = 10^3 emu
Permeability	μ	dimensionless	H/m, Wb/(A·m)	4π x 10^{-7}
Volume susceptibility	χ	dimensionless	dimensionless	4π (SI) = 1 (cgs)
Mass susceptibility	χ_ρ	m^3/kg	emu/Oe·g	1 m^3/kg = $10^3/4\pi$ emu/Oe·g

1.4.1 Classes of magnetism

1.4.1.1 Diamagnetism

Diamagnetism results from the orbital motion of electrons; consequently, it occurs in all materials. However, the magnitude of the susceptibility (χ) is weak, and becomes insignificant in materials that exhibit other types of magnetism. For materials with closed electron shells, such as inert gases, many metals, most nonmetals, and many organic compounds, diamagnetic behavior is prominent. There is no permanent magnetic dipole moment in these materials, and they possess a small, negative χ that is caused by repulsion of an applied field by the orbital motion of the electrons, independent of temperature (Figure 1-3 and Figure 1-5)[63].

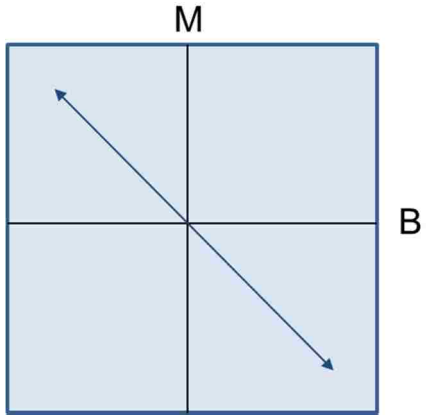

Figure 1-3. The magnetic moment of a diamagnetic material will slightly repel an applied field at all field strengths.

1.4.1.2 Paramagnetism

Paramagnetism is observed in materials with unpaired electrons. Paramagnetic materials have a small, positive χ and some of the molecular moments will be slightly attracted to a magnetic field. However, there is no long-range ordering, and the material does not retain its magnetic properties upon removal of the field (Figure 1-4 and Figure 1-5). Unlike diamagnetism, the χ of paramagnetic materials varies inversely with temperature as described by the Curie law, where *C* is the Curie constant per gram[63].

$$\chi = \frac{C}{T} \tag{1-26}$$

Paramagnetic materials include liquid O_2, rare earth salts, and ferro- and ferrimagnetic materials above the Curie temperature, as described below.

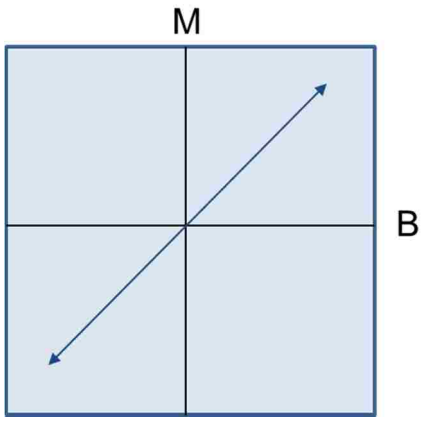

Figure 1-4. The magnetic moment of a paramagnetic material is slightly attracted to an applied field.

1.4.1.3 Ferromagnetism

Ferromagnetic materials have a large, positive susceptibility to magnetic fields. They exhibit a strong attraction to magnetic fields and unlike diamagnetic and paramagnetic materials, are able to maintain long-range ordering after the external field is removed. Ferromagnetic materials have some unpaired electrons, so their atoms have a net magnetic moment. Under an applied field below the Curie temperature (T_C), the magnetic moments align in parallel, resulting in a strong net magnetic moment (Figure 1-5). Above T_C, the spins possess the thermal energy to overcome their long range ordering and assume random orientation, yielding paramagnetic behavior. Iron, nickel, and cobalt are some examples of ferromagnetic materials.

1.4.1.4 Antiferromagnetism

Antiferromagnetic materials have a small, positive susceptibility that varies as a function of temperature with a maximum at the Néel temperature (T_N). Below T_N, the magnetic moments align in a more or less antiparallel arrangement. The tendency to assume the antiparallel arrangement becomes stronger as the temperature is lowered below T_N, until at 0K, the antiparallel arrangement is perfect, as depicted in Figure 1-5[63]. Antiferromagnetic ordering disappears above T_N, where there is sufficient thermal energy to allow the spins to orient randomly, and the material exhibits paramagnetic behavior. There are a large number of antiferromagnetic materials that are often ionic compounds of oxides, sulfides, chlorides, etc.

1.4.1.5 Ferrimagnetism

Ferrimagnetism is similar to antiferromagnetism, in that the magnetic spins oppose each other. However, because the moments of the spins have different magnitudes, they only partially cancel each other out and the material has a net magnetic moment (Figure 1-5). As observed in ferromagnetic and antiferromagnetic materials, above T_C, thermal energy permits randomization of the spins, and the material becomes paramagnetic. Ferrites have the general formula $MO{\cdot}Fe_2O_3$, where M represents Fe, Ni, Mn, Cu, or Mg.

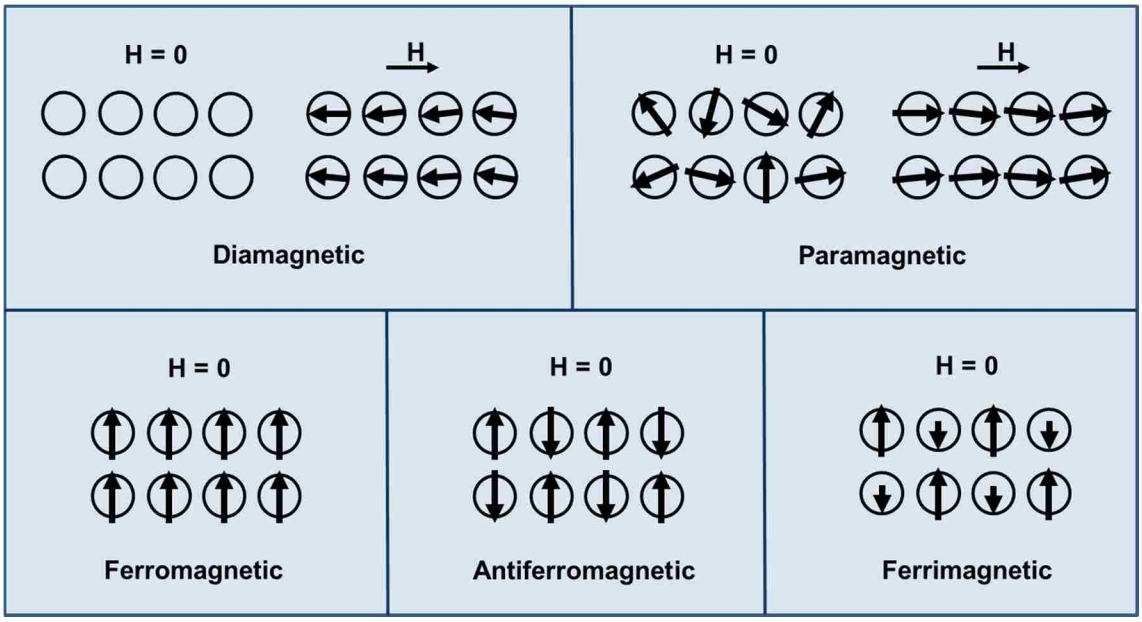

Figure 1-5. Illustration of the magnetic dipole alignments described in the text in the presence or absence of an external magnetic field (H). Adapted from [64].

1.4.1.6 Superparamagnetism

Superparamagnetism differs from ferro- and ferrimagnetism in that is purely a nanoscale effect. It is observed only particles that are small enough to have a

single magnetic domain, unlike the corresponding bulk material, which is made up of many magnetic domains. The maximum size of the magnetic domain depends on the material, but is generally on the order of tens of nanometers[7].

Superparamagnetism describes the state when there is sufficient thermal energy to overcome the energy barrier to reversal of the magnetic moment on the timescale of the experiment. When the energy barrier is large with respect to the thermal energy, the magnetization is "blocked" and the probability of a spontaneous reversal is negligible. When the energy barrier is low, thermal excitations can result in the reversal of magnetization on very short timescales.

Assuming a uniaxial particle, there are two energy minima with antiparallel orientation separated by an energy barrier, E_a (Figure 1-6). The crystallographic axis that represents these energy minima is referred to as the easy axis. The magnetic energy is minimized when the particle's magnetization vector is aligned with the easy axis, and increases with the tilt angle between the magnetization vector and the easy axis[63, 65].

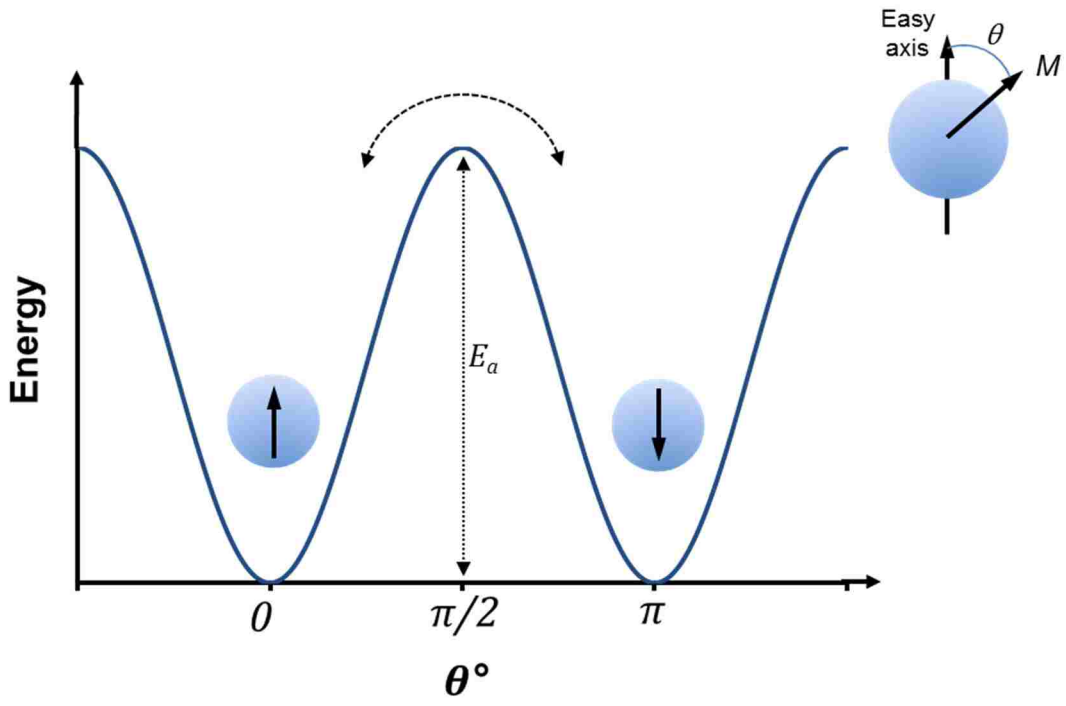

Figure 1-6. The magnetic anisotropy energy of a single domain particle with uniaxial anisotropy as a function of magnetization direction. E_a is the energy barrier to reversal of the magnetization and θ is the tilt angle between the magnetization vector and the easy axis. Adapted from [65].

The energy barrier, E_a, separating the energy minima at θ = 0 and $\theta = \pi$ is termed the anisotropy energy (E_a), and is proportional to the product of the nanoparticle volume V, and the anisotropy constant, K:

$$E_a = KV \tag{1-27}$$

The timescale on which particle or ensemble of particles can experience a magnetization reversal follows Arrhenius kinetics and is given by the Neel-Brown equation[66]:

$$\tau_N = \tau_0 \exp\left(\frac{E_a}{k_B T}\right) \tag{1-28}$$

where τ_N is referred to as the Néel relaxation time, τ_0 is the attempt time, generally taken to be 10^{-9} seconds[67], k_B is the Boltzmann energy, and T is the absolute temperature. τ_N is very sensitive to the size of the nanoparticle, so with increasing particle size, the energy barrier to magnetic reversal, E_a, will be dominant over thermal contributions, k_BT. For small nanoparticles, thermally activated reorientation of the spins away from the easy axis is no longer negligible. Equation (1-28) can be rearranged to solve for the critical temperature that defines the point at which thermal energy allows random reorientation of the spins:

$$T_B = \frac{KV}{\ln\left(\frac{\tau}{\tau_0}\right) k_B} \tag{1-29}$$

T_B is the blocking temperature, and is the transition point between ferro- or ferri-magnetic behavior and superparamagnetism. The "super" part of superparamagnetism arises from the net magnetic dipole of the entire particle that is actually greater than the sum of its individual electrons in response to an applied external field. This is in contrast to paramagnetism, as described previously, where only the small moments of single ions align with an applied field. Superparamagnetic materials lack remnant magnetization, so when the external field is removed, the spins relax to a random state and the net magnetic moment is zero.

1.4.2 Iron Oxides

Iron oxides are varied and widespread in nature. They have served as pigments, catalysts, and precursors in the formation of iron and steel[68]. A brief review of the iron oxide compounds encountered most frequently in this body of research is presented here.

1.4.2.1 Wüstite ($Fe_{1-x}O$)

Wüstite contains only divalent Fe cations and crystallizes in the sodium chloride structure. The unit cell edge length is a = 0.430 nm, with four formula units per cell. Vacancies in the Fe site result in a non-stoichiometric compound with the general formula $Fe_{1-x}O$. $Fe_{1-x}O$ is antiferromagnetic below its T_N of ~198 K[63]. Under ambient conditions, $Fe_{1-x}O$ exists as a metastable compound that can be converted to α-Fe and magnetite (Fe_3O_4) through disproportionation or oxidation[68].

1.4.2.2 Magnetite (Fe_3O_4)

Fe_3O_4 is the most magnetic of all the naturally occurring minerals on Earth. At room temperature and standard atmospheric pressure, magnetite has a face-centered cubic inverse spinel structure with 32 O^{2-} ions in a cubic close packed arrangement, with divalent and trivalent Fe cations occupying interstitial tetrahedral and octahedral sites. 16 Fe^{3+} ions are equally divided between the tetrahedral, or “A” sites and octahedral, or “B” sites. 8 Fe^{2+} ions occupy the octahedral or “B” sites[63, 68]. At room temperature, an electron can hop between

Fe^{2+} and Fe^{3+} ions in the octahedral sites, imparting a half-metallic property to magnetite. The magnetic moment of the unit cell is contributed only by Fe^{2+} ions[69].

The unit cell edge length is *a* = 0.839 nm, with eight formula units per cell[20, 22]. Above temperatures of about 122K, Fe_3O_4 undergoes a Verwey transition, characterized by a lattice distortion as well as an increase in conductivity attributed to electron hopping processes between Fe^{2+} and Fe^{3+} ions[70, 71]. Fe_3O_4 is a ferrimagnetic material that can exhibit superparamagnetism on the nanoscale where particles with single magnetic domains can be synthesized. The upper limit for superparamagnetism in spherical Fe_3O_4 particles with uniaxial anisotropy is approximately 80nm[72]. The mass saturation magnetization for bulk Fe_3O_4 is at 92 $A{\cdot}m^2/kg$ at 293K[63].

1.4.2.3 Maghemite (γ-Fe_2O_3)

γ-Fe_2O_3 has a structure very similar to Fe_3O_4, with a cubic unit cell length of *a* = 0.834 nm. γ-Fe_2O_3 is made by oxidizing magnetite:

$$2Fe_3O_4 + \frac{1}{2}O_2 \rightarrow 3Fe_2O_3$$

The primary difference between γ-Fe_2O_3 and Fe_3O_4 is that the iron in γ-Fe_2O_3 is present only in the trivalent state. Like Fe_3O_4, γ-Fe_2O_3 is ferrimagnetic, and at the nanoscale, single magnetic domain nanoparticles also display superparamagnetism. However, the mass saturation magnetization for bulk γ-Fe_2O_3 is significantly lower than that of Fe_3O_4 at 76.0 $A{\cdot}m^2/kg$ at 293K[63, 68].

1.5 Selected biomedical applications of iron oxide nanoparticles

As discussed previously, magnetite nanoparticles have been studied extensively in a number of biomedical research applications. However, they are currently in clinical use as contrast agents for magnetic resonance imaging as well as potential use for emerging modalities such as Semiconductor Quantum Interference Device (SQUID) relaxometry, a promising technique for providing early detection of breast and ovarian cancer, transplant rejection, and Alzheimer's disease[24, 73, 74].

1.5.1 Magnetic Resonance Imaging (MRI)

Fe_3O_4 nanoparticles have found clinical use as magnetic resonance contrast agents, including use for imaging of the bowel, liver and spleen, lymph node, bone marrow, perfusion imaging, and magnetic resonance angiography[75]. Their low toxicity has made Fe_3O_4 nanoparticles attractive for use as contrast agents[76]. The nanoparticles are metabolized by lysozymes, where after the liberated iron enters the body's plasma iron pool. Eventually, it is excreted from the body as the iron stores turn over[75]. These nanoparticles have been marketed commercially with sizes specific to their particular use (Table 1-3). Because they have gained FDA approval for clinical use, there is obvious potential for translating their use to other clinical modalities.

Table 1-3. Commercial formulations of Fe_3O_4 nanoparticles approved for use as MRI contrast agents. Adapted from [75]

Generic name	Trade name	Developing Company	Size (nm)	Use
Ferumoxsil	Lumirem	Guerbet	~300	Bowel contrast
	Gastromark	Advanced Magnetics		
	Abdoscan	Nycomed		
Ferumoxide	Endorem	Guerbet	80 – 150	Liver/spleen imaging
	Feridex IV	Berlex Laboratories		
	Resovist	Schering	60	
Ferumoxtran	Sinerem	Guerbet	20 – 40 nm	Lymph node, bone marrow imaging
	Combidex	Advanced Magnetics		
	Clariscan	Nycomed	20 nm	Perfusion imaging, angiography

1.5.2 Superconducting Quantum Interference Device (SQUID) relaxometry

This technique relies on the mechanism of relaxation of an ensemble of superparamagnetic nanoparticles following the alignment in an external DC magnetic field. Relaxation of the particle moments into a randomly oriented state can occur by either a Brownian or Néel mechanism.

When a particle undergoes Brownian relaxation, it physically rotates in the surrounding medium, so that the time constant for relaxation (τ_B) is proportional to

the hydrodynamic volume of the particle and the dynamic viscosity of the carrier liquid:

$$\tau_B = \frac{3\eta V_h}{k_B T} \tag{1-30}$$

where η is the dynamic viscosity of the medium, V_h is the hydrodynamic volume, k_B is the Boltzmann constant, and T is the absolute temperature. Revisiting the previous discussion of the Néel relaxation process, and substituting equation (1-27) into (1-28) gives:

$$\tau_N = \tau_0 \exp\left(\frac{K\mathrm{V}}{k_B T}\right) \tag{1-31}$$

For most particle diameters, Brownian and Néel relaxation occur on very different time scales, allowing the specific mode of relaxation to be distinguished. τ_N and τ_B for Fe_3O_4 particles in water over the range of diameters from 10 – 28 nm are plotted in Figure 1-7. It can be seen that for diameters less than 18 nm, τ_N occurs faster than τ_B. However, as discussed previously, τ_N is very sensitive to particle size and increases rapidly as particle diameter increases.

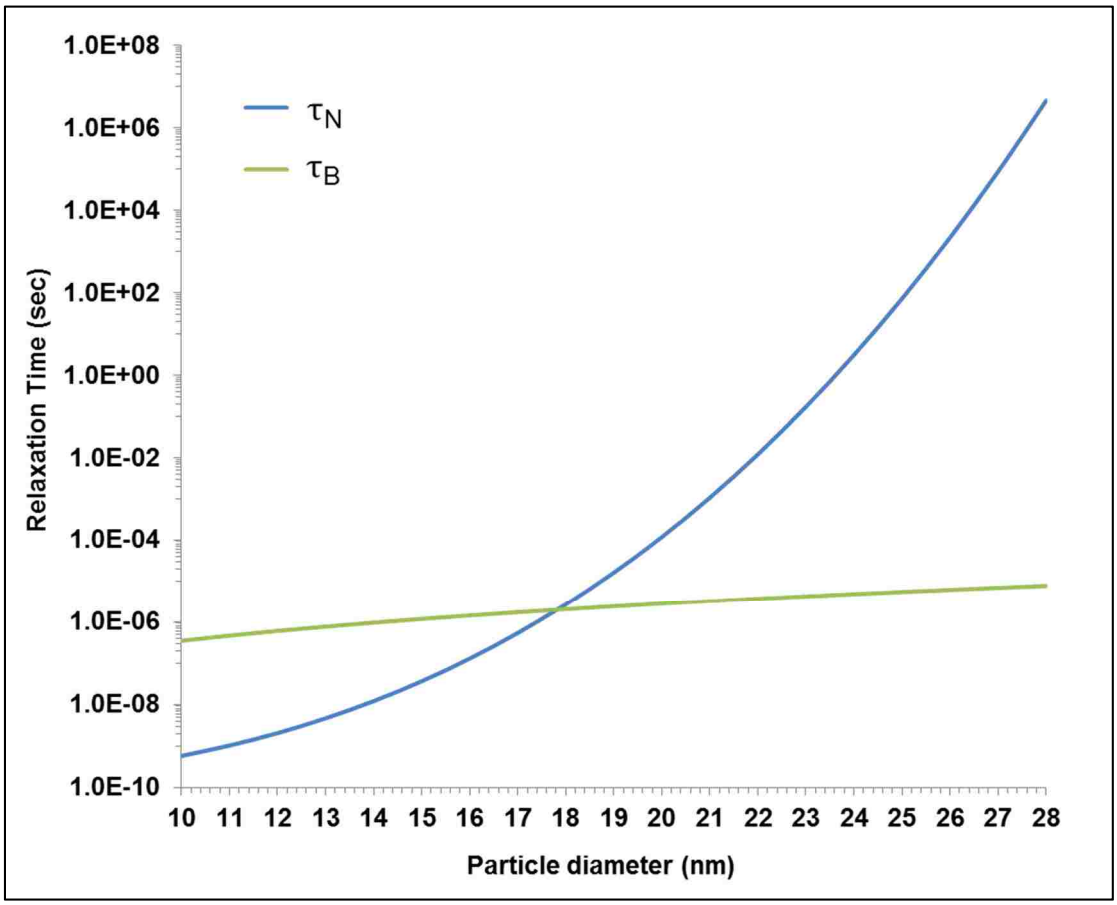

Figure 1-7. Néel relaxation (τ_N) and Brownian relaxation (τ_B) for Fe_3O_4 nanoparticles in water. τ_N increases rapidly with respect to τ_B because of the $\exp(r^3)$ dependence on particle size.

From a clinical perspective, magnetic relaxometry offers a method for detecting and quantifying small populations of cancer cells[24, 77]. The nanoparticles are first functionalized with antibodies or other molecules that selectively bind to antigens expressed on the surface of pathogenic cells. When the labeled nanoparticles are introduced to a sample containing the target cancer cells, some particles will attach to the cells, while others will remain unbound. Particles that do not attach to their target will be able to move freely and thus experience Brownian relaxation. Particles that attach to the target cells will be physically immobilized and will

undergo Néel relaxation. Because the timescale for these two processes is significantly different, sensitive quantification of bound nanoparticles can be achieved, even with a high background of unbound particles[78].

The relaxometry experiment proceeds as follows: the particles are subject to a 0.3 second DC pulse followed by a 50 millisecond delay. Magnetic dipole relaxation is detected by a superconducting quantum interference device (SQUID) for 2 seconds. Particles that relax too quickly, e.g., during the delay, as well as particles that relax too slowly, e.g., after the measurement has completed, will not be detected (Figure 1-8)[24].

Figure 1-9 illustrates the strong dependence of τ_N on particle volume, emphasizing the stringent particle requirements for optimized SQUID relaxometry. Only a narrow range of particle diameters possess a τ_N detectable within the 50 millisecond – 2 second timescale of the measurement. For a system of Fe_3O_4 nanoparticles suspended in water at 293K with K equivalent to that of bulk Fe_3O_4 (1.35×10^4 J/m^3)[79], the suitable range of particle diameters is 21.7 – 23.2 nm, as depicted in Figure 1-9. Furthermore, maximum signal can be obtained only when an ensemble of particles has a low size and shape dispersity[78].

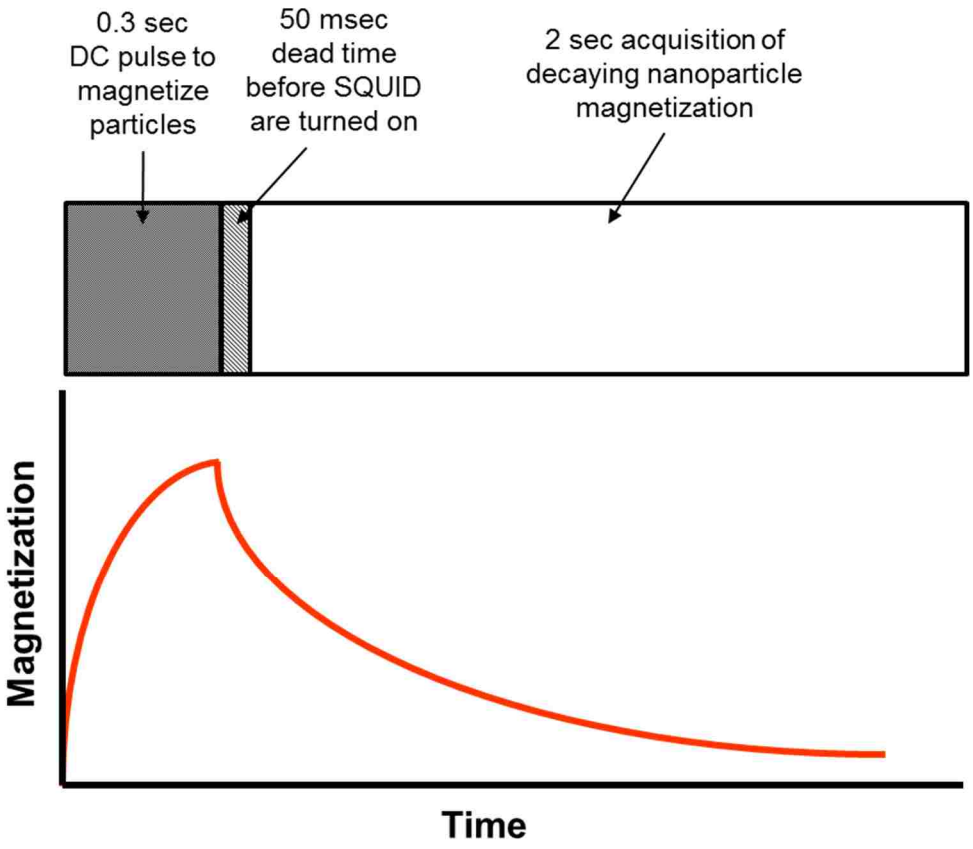

Figure 1-8. The SQUID relaxometry experiment. Particles that decay too quickly (during the 50 ms dead time) are not detected. Particles that decay too slowly (≫ 2 seconds) are also not detected. Adapted from [24].

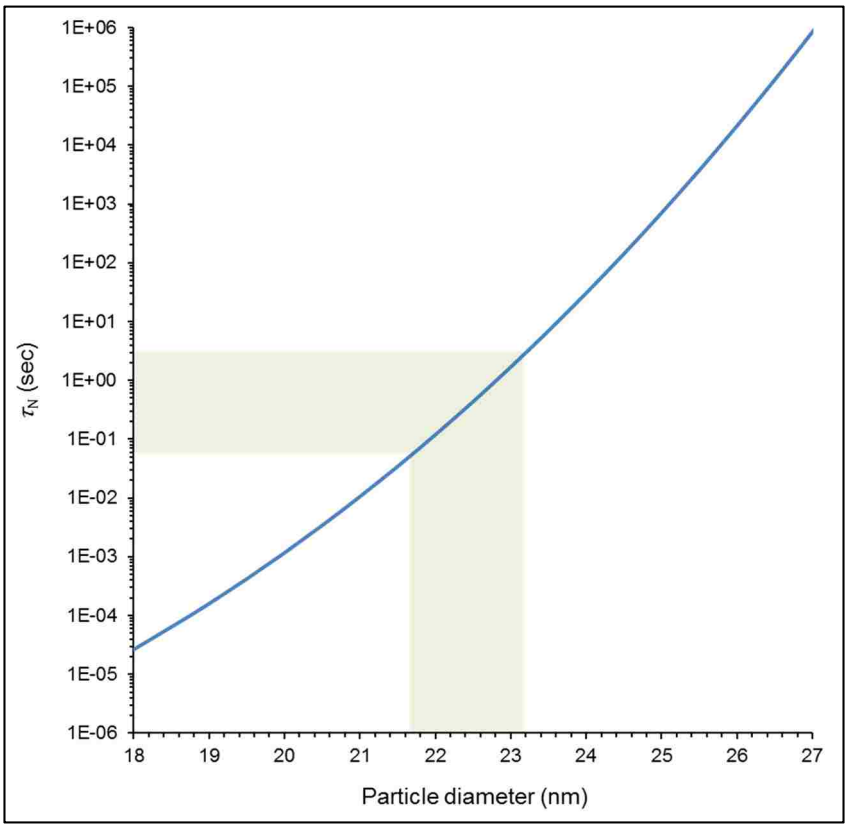

Figure 1-9. τ_N as a function of Fe_3O_4 nanoparticle diameter. The highlighted area shows the range of particle diameters that would be suitable for use with the timescale of a SQUID relaxometry measurement.

Preliminary in vitro experiments suggest that this technology will be capable of detecting just a few thousand cells located several centimeters from the sensors, enabling the early detection of cancer or other diseases in human subjects with far greater sensitivity than current clinical methods[80]. Identifying the early stages of tumor growth has the potential to dramatically improve diagnostic capabilities and survival outcomes for cancer patients.

Chapter 2 – Goals and Objectives

2.1 Problem Statement

The previous discussion has underscored the need for high quality, size controlled nanoparticles if their potential in both research and commercial applications is to be realized. Several claims of size control have been reported in the literature, but to date, only a few discrete sizes over a limited range have been achieved[44, 81, 82]. Equally important is the need to maintain reproducibility between syntheses, which currently presents a serious challenge. For example, a number of magnetite synthesis protocols have adopted the use of a custom-synthesized iron carboxylate precursor designed by the Hyeon group to achieve particles with low shape and size dispersity[44]. However, the nature of the compound and batch-to-batch variability in the preparation method leads to variation in the synthesized nanoparticles[83]. Specific reaction heating ramp rates have also been reported as a critical parameter for induction of nucleation and control of particle size[44, 84]. Variable performance can be observed not only between commercial temperature controllers, but with the same temperature controller from experiment to experiment, which is a significant source of irreproducibility in this system.

2.2 Hypothesis

The goal of this body of work is to develop a completely novel approach to magnetite nanoparticle synthesis that will reproducibly provide precise size control of synthesized nanoparticles with low size dispersity that are critical requirements

for clinical applications. Further, such a process will need to be scalable if it is to meet commercial production demands. If these goals are met, there is potential for broad impact for a number of applications.

2.3 Objectives and Specific aims

The scientific objectives of this work primarily involve the development of a comprehensive understanding of the materials properties, structure-property relationships, and the proposal of a mechanism for the formation and growth processes of the synthesized nanomaterials. Identifying such a mechanism will contribute to an overall understanding of kinetic growth mechanisms for solution-based nanoparticle synthesis. The aims listed below detail the plan of research.

Aim 1: Identify an iron precursor that will allow reproducible synthesis of iron oxide nanoparticles removing batch-to-batch irreproducibility introduced by non-stoichiometric starting materials.

Aim 2: Develop a reaction scheme that will eliminate the temperature ramp rate as a potential source of variability between reactions.

Aim 3: Design a novel synthetic method to achieve reproducible, systematic size control of thermolytically synthesized magnetite nanoparticles. The size of the particles will be controlled with nanometer precision and nearly uniform size dispersity.

Aim 4: We will establish a mechanism for growth of the synthesized magnetite nanoparticles. Elucidating a mechanism will allow rational size control to be established, which will have positive implications for commercial scalability.

Chapter 3 – Fundamentals of Characterization Techniques

3.1 Introduction

A number of techniques were used to characterize the reaction intermediates and products. To provide a comprehensive understanding of their physical properties, complimentary techniques were chosen to study the crystalline structure, composition, and magnetic behavior of the synthesized nanoparticles at different length scales.

3.2 Fourier transform infrared (FTIR) spectroscopy

Almost every organic or inorganic compound containing covalent bonds absorbs wavelengths in the infrared region of the electromagnetic spectrum. Of greatest interest for studying chemical compounds is the vibrational portion of the infrared region (2.5 μm – 25 μm). Radiation in the vibrational infrared region is usually referred to in units of wavenumbers and expressed in reciprocal cm (cm^{-1}). These units are useful since wavenumbers are directly proportional to vibrational energy[85]. Bonds that possess a permanent dipole moment are capable of absorbing infrared energy that matches their natural bending and stretching vibrational frequencies. While each molecule can be identified by its own unique spectrum, structural information about the material can be determined since each type of bond is generally found in a particular range of the infrared spectrum.

For the measurements in this study, a Bruker IFS 66/S nitrogen purged or IFS 66/vS vacuum evacuated FTIR spectrophotometer was used. Data collected on

the FTIR are output in the form of an interferogram, a spectrum of intensity versus distance for all frequencies. A Fourier transform of the data then produces a plot of intensity versus frequency (cm^{-1}).

Typically, liquid organic samples, such as those analyzed in this study, can be measured neat by pressing a drop between two polished potassium bromide (KBr) plates, as KBr is transparent to IR frequencies from 4000 – 400 cm^{-1}. However, for some aspects of our analysis, we sought to use FTIR as a semi-quantitative technique, in which the peak intensities of different samples could be compared directly. The small differences in the path length introduced by preparing a sample with even slightly variable thickness made this type of comparison difficult. Attenuated total reflectance (ATR) was an alternative technique to measuring the samples that ensured a constant path length between sample measurements. In the ATR technique, the IR beam is directed into a crystal with a refractive index much larger than the sample. The IR beam reflects from the internal surface of the crystal and creates an evanescent wave that projects orthogonally into the sample. The intensity of the generated evanescent wave decays exponentially as a function of the distance from the boundary between the crystal and the sample. In the region where the sample absorbs energy, the evanescent wave will be attenuated. The reflected beam, some of which has been absorbed by the sample, is returned to the detector. The ATR phenomenon is illustrated in Figure 3-1.

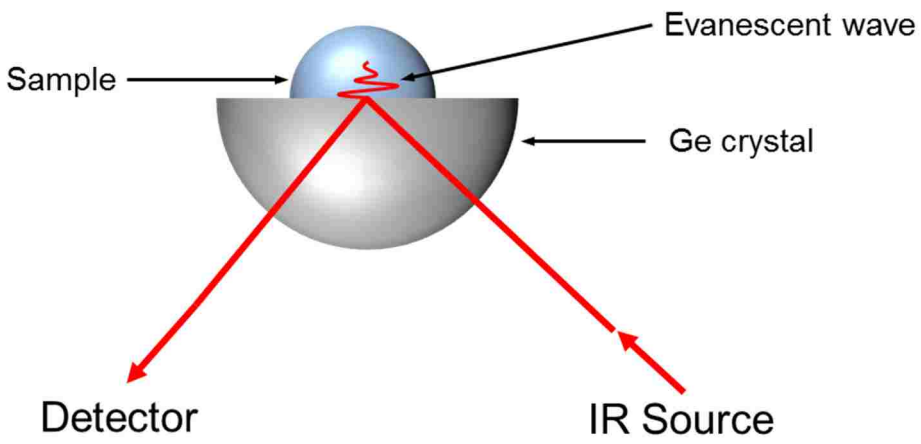

Figure 3-1. Illustration of the ATR effect.

The refractive indices of the crystal and the sample govern the ATR phenomenon as described by the following equation:

$$\theta_c = sin^{-1}\left(\frac{n_2}{n_1}\right) \tag{3-1}$$

where n_2 is the refractive index of the sample, n_1 is the refractive index of the crystal, and θ_c is the critical angle. When the critical angle requirement is satisfied, total internal reflection of the light wave occurs and an evanescent wave is created. The depth of penetration (d_p) of the evanescent wave into the sample is the distance required for its intensity to decay to e^{-1} of its value at the surface and can be calculated by:

$$d_p = \frac{\lambda}{2\pi(n_1^2 sin^2\theta - n_2^2)^{\frac{1}{2}}} \tag{3-2}$$

where λ is the wavelength of light and θ is the angle of incidence of the IR beam. For our measurements, a grazing angle attenuated total reflectance (GATR) accessory with $\theta = 65°$ and a Ge crystal with $n_1 = 4.01$ was used (Harrick Scientific

Products Inc., Pleasantville, NY). We assume a refractive index (n_2) of 1.5 for our samples, characteristic of many organic materials. The calculated θ_c is then 22.0°, and d_p is approximately 0.5 μm, and the theoretical effective path length is 0.096 μm. The penetration depth is significantly less than the height of a small drop of sample, so the effective path length for measurement can be maintained between samples.

A room-temperature DTGS detector is suitable for most transmission measurements, although the intensity of the signal emerging from the GATR is reduced to the extent that a higher sensitivity, liquid nitrogen cooled MCT detector is required. Prior to measurements, the MCT detector was cooled for at least one hour. A background spectrum was acquired immediately prior to each sample. The sample spectrum was acquired after depositing a droplet of neat sample, several mm in diameter, on the crystal surface. For all measurements, a 180 second delay between closing the sample compartment and collection of the spectrum was used to ensure removal of atmospheric gases such as CO_2 and water vapor that can interfere with the sample spectrum. Background and sample measurements were taken from 3400 cm^{-1} to 700cm^{-1} using an average of 256 scans with a resolution of 2 cm^{-1}. Because the penetration depth of the crystal varies with the infrared frequency, extended ATR correction was performed on the collected spectra using Opus 6.5 software assuming an index of refraction of 1.5 for the aliquots. No additional baseline corrections were performed.

3.3 X-Ray techniques

The scattering of waves by a crystal can be used to study its structure, as explained by English physicist Sir W. H. Bragg and his son, Sir W. L. Bragg[86] (Figure 3-2):

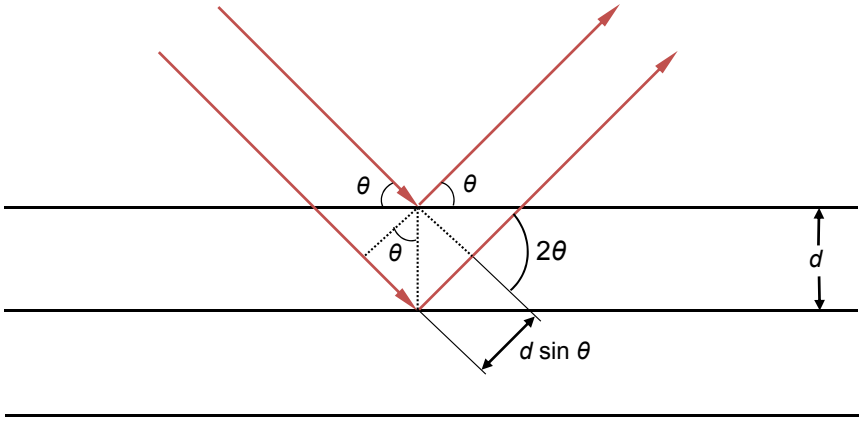

Figure 3-2. Diffraction of incident waves from parallel atomic planes in a crystal. θ is the angle of incidence and d is the spacing of planes.

In a lattice structure, with planes at a spacing of d, incident waves reflect specularly from parallel atomic planes in the crystal. In specular reflection, the angle of incidence is equal to the angle of reflection, with the diffracted beams interfering constructively. For simplicity, the scattering of waves is assumed to be elastic, in which the energy of the wave is not altered upon reflection. The path difference for radiation reflected from adjacent places is $2d \sin \theta$, with constructive interference of the radiation from successive planes occurring when the path difference is an integral number n of wavelengths λ. This phenomenon is summarized by the Bragg Law[87]:

$$2d \sin \theta = n\lambda \qquad (3\text{-}3)$$

Because Bragg reflection can only occur when the wavelength of the radiation is comparable to or smaller than the lattice constant ($\lambda < 2d$), visible light cannot be used. For this reason, scattering of X-rays by the electrons in a material can be used to measure the average spacing between planes of atoms, determine crystal orientation, identify crystal structure, and measure crystallite size and shape.

To satisfy Bragg's Law, θ must change as d changes; e.g., θ decreases as d increases. Using a CuKα X-ray source (λ = 1.541Å), 2θ and the scattering vector, q, can be calculated for various values of d (Table 3-1).

Table 3-1. Values of the angle of X-ray scattering (2θ) and the scattering vector, q, calculated for different values of lattice spacing, d.

d (Å)	2θ (degrees)	$q = (4/\lambda)\sin\theta = 2\pi/d$ (1/ Å)
10	8.87	0.628
50	1.77	0.126
100	0.88	0.063
500	0.176	0.0126
1000	0.088	0.0063

Table 3-1 shows that high-angle X-ray diffraction (XRD) gives information on the crystal structure on the atomic scale, and can be used to determine crystallite size from the width of the diffraction peaks[88]. Conversely, small angle X-ray scattering (SAXS) is not sensitive to the structure of the crystal, but provides structural information on a larger scale, such as the size of a nanoparticle. For our studies, XRD was employed to determine the phase of the material, and SAXS was used

to determine the average size of an ensemble of nanoparticles. For all XRD and SAXS measurements, a Rigaku SmartLab® X-ray diffraction system was used with CuKα radiation (Figure 3-3).

3.3.1 X-ray diffraction (XRD)

The diffraction pattern generated from the samples was analyzed using PDXL X-ray powder diffraction software for phase identification. Powder samples were prepared by placing several drops of concentrated colloidal suspension on a silicon substrate and allowing the solvent to evaporate. Phase was determined by matching the diffraction peaks of the sample with those in a database provided by the International Center for Diffraction Data (ICDD).

3.3.2 Small angle X-ray scattering (SAXS)

X-ray scattering occurs when nanoparticles with electron density that differs from the electron density of the surrounding matrix are irradiated[89]. In order to extract information on the nanoparticle size distribution, a model of the particle shape is assumed and fit to the data using a least-squares fitting process. For our analysis, NANO-Solver software was used to fit the scattering profile. SAXS is a robust technique for characterizing particle size distributions as an ensemble of particles is measured, thus providing more comprehensive statistics than can be reasonably attainable by electron microscopy.

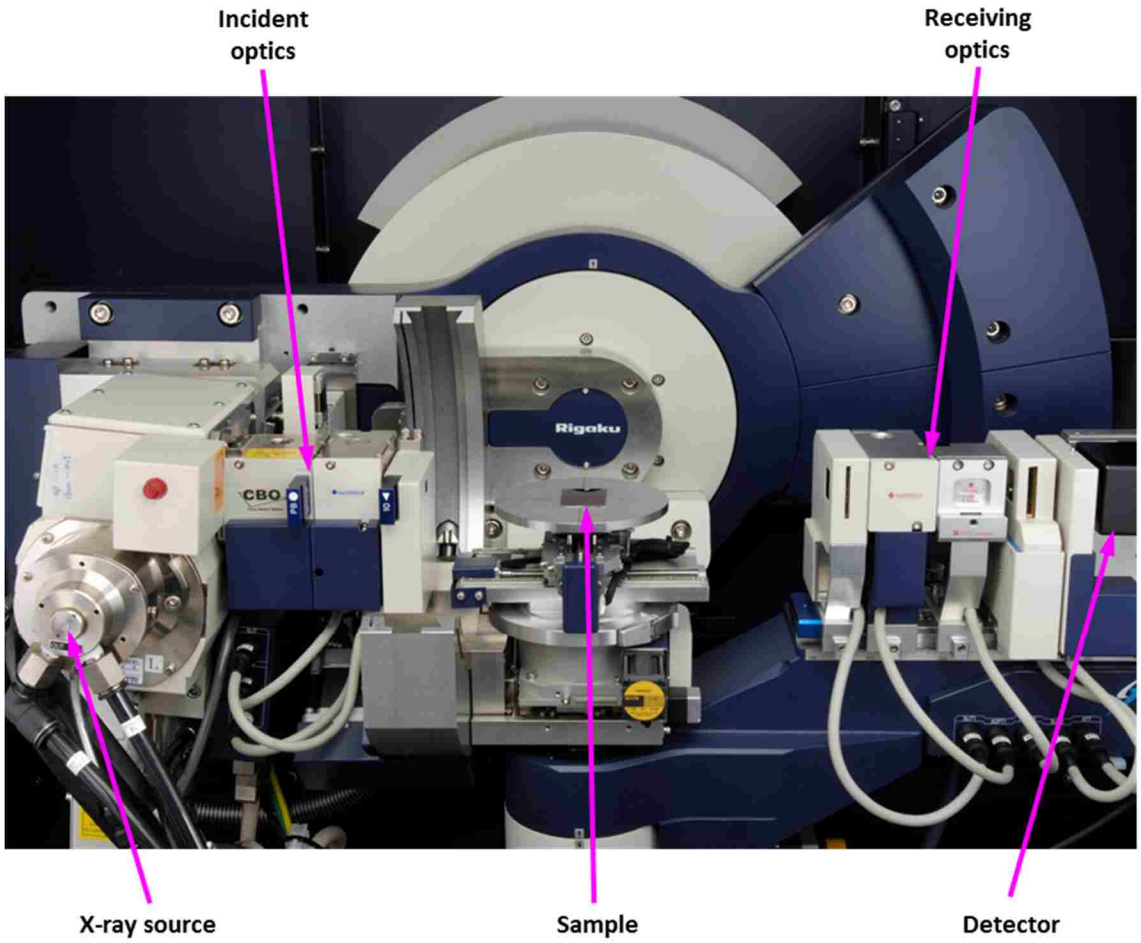

Figure 3-3. Rigaku SmartLab X-ray diffractometer with parallel beam optics. Image courtesy of Rigaku Americas Corporation.

3.4 Transmission Electron microscopy (TEM)

Transmission electron microscopes use a high energy electron beam transmitted through a very thin sample to image and analyze the microstructure of materials. In the case of a high resolution TEM, atomic scale resolution can be achieved. The electron beam is focused with electromagnetic lenses and the resulting image is observed on a phosphorescent screen, or recorded digitally. The electrons in the beam are accelerated at several hundred keV, generating wavelengths much

smaller than that of visible light. For example, an electron with a 300 keV accelerating voltage has a wavelength of 0.02 Å. Unlike optical microscopy, where the spatial resolution is limited by the wavelength of light, spatial resolution in the electron microscope is limited by aberrations inherent in electromagnetic lenses. Like X-rays, when electrons pass through the TEM sample, diffraction will occur following Bragg's Law, as discussed previously. The basic difference between electron diffraction and X-ray diffraction is that very small specimen areas can be studied using electron diffraction, such as a small group of isolated nanoparticles.

3.4.1 JEOL 1200 EX TEM

The JEOL 1200 EX has a tungsten hairpin filament with approximately 0.5 nm spatial resolution (JEOL USA, Inc., Peabody, MA). Images for size analysis were acquired in bright field mode at an acceleration voltage of 120 keV.

3.4.2 FEI Tecnai G^2 Twin F30 High Resolution Transmission Electron Microscope (HRTEM)

The Tecnai G^2 Twin F30 is a field emission gun TEM with a spatial point-to-point resolution of 0.20 nm (FEI, Hillsboro, OR). This instrument was operated in bright-field mode to image the crystalline lattice structure of several samples at an acceleration voltage of 300 keV.

3.5 Superconducting Quantum Interference Device (SQUID) Magnetometry

An MPMS SQUID magnetometer was used for sample measurements (Quantum Design, San Diego, CA). The SQUID is one of the most sensitive devices available for detecting magnetic fields, and when used as a magnetometer can detect a magnetic moment of 10^{-10} A·m^2 [63]. The components of the MPMS include a superconducting magnet wound in a solenoid that can generate magnetic fields up to 7 T. A transport mechanism controls the movement of the sample through superconducting detection coils, which are in turn connected to the SQUID, located 11 cm below the magnet. A superconducting shield protects the SQUID from ambient magnetic fields and from the large magnetic field produced by the superconducting magnet. Temperature control allows sample measurements from 2–400K. Although the SQUID provides the high sensitivity of the instrument, the sample's magnetic field is not detected by the SQUID directly. Rather, the sample passes through the superconducting pickup coils, which are connected to the SQUID by superconducting wires. The magnetic moment of the sample induces an electric current in the pickup coils, which is detected by the SQUID and converted to an output voltage that is proportional to the sample's magnetic moment[90]. Some of the major features of the device are presented schematically in Figure 3-4.

Figure 3-4. Schematic drawing of the major components surrounding the sample in the SQUID

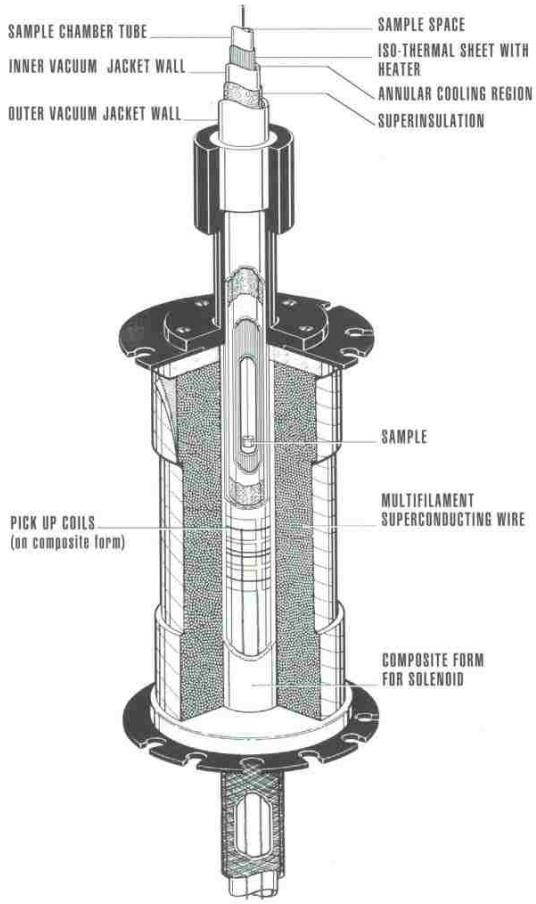

MPMS. Image courtesy of Quantum Design, Inc.

The magnetic properties of the synthesized materials were characterized using DC magnetometry. In a DC measurement, the magnetic response of a material to the applied field, $M(H)$, or temperature, $M(T)$, can be studied.

3.5.1. Magnetization vs. field

A typical hysteresis curve reflecting the change in magnetization of a sample (M) with respect to the applied field (H) is diagrammed in Figure 3-5. The most common type of hysteresis curve *M(H)*, called a major loop, is generated by starting from a positive saturating magnetic field (M_S), decrease the field to

negative saturation, and then back to positive saturation. M_R represents the material's remnant magnetization when $H = 0$. H_C is the coercive field required to return the magnetization of the sample to 0. The DC susceptibility (χ_{DC}) is the slope of the magnetization curve near the origin:

$$\chi_{DC} = \frac{dM}{dH_{DC}} \tag{3-4}$$

Hysteresis in magnetic materials is a kinetic effect; at a given temperature, the individual magnetic moments don't have the thermal energy to reorient on the timescale of the measurements. Therefore, hysteresis and coercivity are only observed for ferro- or ferrimagnetic materials. Superparamagnetic materials above T_B, have a high initial susceptibility with no observed hysteresis or coercivity.

Figure 3-5. An *M(H)* curve that shows the magnetization of the sample versus the applied magnetic

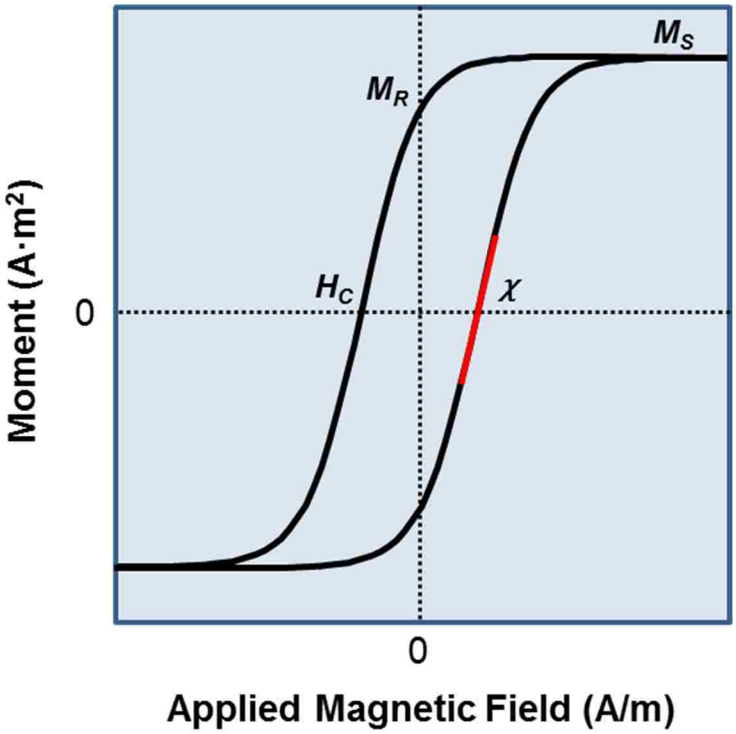

field. *Ms* is the saturation magnetization, M_R is the remnant magnetization, H_C is the coercive field, and χ is the susceptibility of the material.

3.5.2 Magnetization vs. temperature

For superparamagnetic samples, measuring the magnetization of a sample as a function of temperature *M(T)* can provide information on the blocking temperature of the sample. In this type of measurement, the sample is first cooled in the absence of an applied field. A small field is then applied (796 A/m = 10 Oe) and the magnetization of the sample is recorded as the temperature is increased. This is referred to as the zero-field cooled (ZFC) measurement. The field cooled (FC) measurement sample is then taken by cooling the sample to the starting temperature under the small applied field. The maximum of the ZFC curve

represents the blocking temperature, T_B. Above T_B, the ZFC and FC curves converge, and decrease as $1/T_B$.

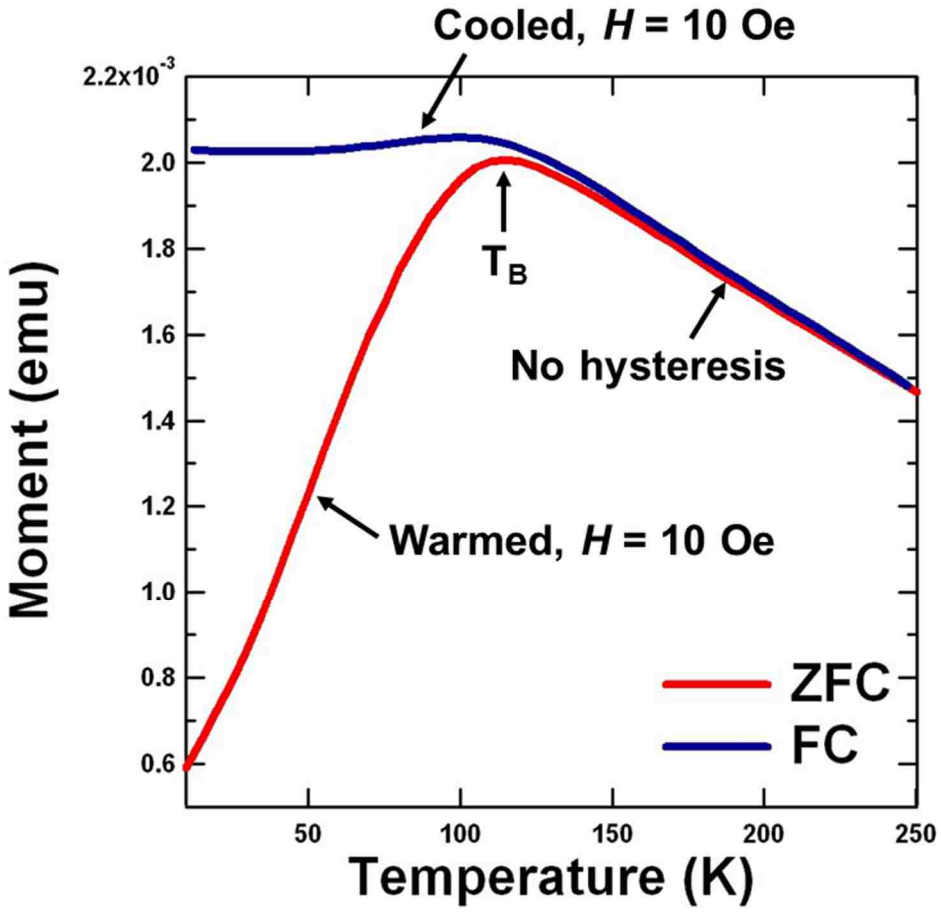

Figure 3-6. An *M(T)* measurement of a superparamagnetic sample. The ZFC curve is obtained by applying a small magnetic field and measuring the magnetization of the sample as it is warmed. The FC curve is obtained as the sample is cooled under the small applied field. The peak of the ZFC curve, and the point of divergence of the ZFC and FC curves is the blocking temperature, T_B.

Chapter 4 – The 'Hot Injection' Method Using Anhydrous Iron Oleate

4.1 Introduction

Iron(III) carboxylates have been used as catalysts for the degradation of plastics[91] and more recently, these compounds have been studied as precursors to the synthesis of magnetite nanoparticles[92, 93]. Due to the low costs of starting materials and relative ease of synthesis, magnetite nanoparticles have been among the most commonly selected magnetic materials for the development of ferrofluids[94, 95]. As discussed in Chapter 1, their biocompatibility makes these magnetic nanomaterials highly desirable as MRI contrast agents and in early stage cancer detection.

Multiple aspects of the nanoparticles, such as size, shape, dispersity, phase, and surfactant coating determine their efficacy in the aforementioned applications. Controlling these parameters at the nanoscale has been executed using a number of precursors and reaction conditions[96, 97]. For clinical applications, it is of the utmost importance that the methods used to prepare the nanoparticles maintain reproducibility between batches, as well as laboratories. Following the currently published techniques for the synthesis of magnetite, we have discovered a significant flaw in the consistent production of nanoparticles in size, shape, and dispersity: exposure of the precursor to water.

Most recent publications describing the synthesis of these particles use an iron(III) carboxylate as the precursor to iron oxide particles[44, 45, 83, 97, 98]. The carboxylate ligand has the ability to form an ionic bond, as well serve as bridging or terminal ligands (Scheme 4-1)[99, 100]. In combination with the oxophilicity of iron(III), the formation and isolation of homoleptic species of iron(III) carboxylates has proven difficult to achieve[83].

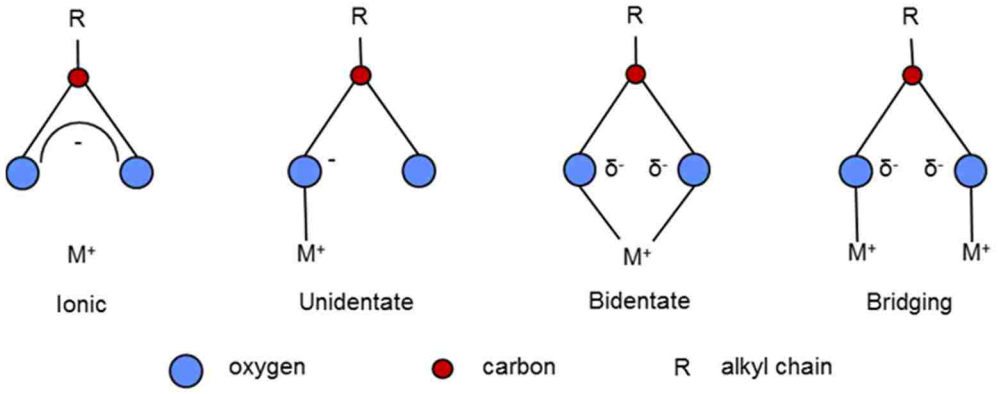

Scheme 4-1. The primary coordination modes between a carboxylate anion and a metal cation. Adapted from [83].

In literature preparations, the synthesis of iron(III) carboxylates often produces trimeric iron clusters with μ-O^{2-} centers as evidenced by elemental analysis[101]. Products are assumed to range from dimeric to polymeric[83], rather than the single molecules desired for reproducibility. This is thought to result from the synthesis of the iron carboxylate compound in the presence of air and water. In addition, slight variations in the preparation, such as reaction temperature, solvent, or synthetic procedure will often incur stoichiometric changes to the Fe:O ratio in the product[91, 102].

In a more recent publication, iron(III) oleate was synthesized by combining iron(III) chloride and three molar equivalents of sodium oleate in a water, ethanol, and hexane slurry[83]. Given the Lewis acidity of Fe^{3+}, its ability to complex with water may lead to the liberation of oleate as oleic acid and the formation of an iron-hydroxide bond. The poor solubility of an iron hydroxide species would shift the equilibrium of this process in favor of free oleic acid. This scenario would only be exacerbated by the subsequent washing steps of the iron(III) oleate product, leading to a quantitatively unknown composition of the resulting material (Scheme 4-2). It has been shown that slight variations in the ratio of iron to surfactant can have material impacts on the size of the resultant particles. For this reason, this material, while well-suited to produce magnetic nanoparticles of various sizes with low size dispersity, is wholly incompatible with precise reproduction desired between batches. It is our intention to utilize a new, anhydrous synthesis of iron(III) oleate, eliminating issues with reproducibility in the synthesis of iron oxide nanoparticles.

Here, we examine the quality of synthesized nanoparticles and reaction reproducibility using the 'hot injection method,' which has been previously been demonstrated to produce high quality semiconductor nanoparticles[103-106]. In the hot injection process, the rapid introduction of reactive precursors into a hot solution creates a condition of high supersaturation. Burst nucleation immediately follows, reducing the supersaturation condition and ending the nucleation event. Additional growth of particles follows by diffusion of monomer species to the particle surface. We propose to apply the hot injection method to the synthesis of

iron oxide nanoparticles for reproducible synthesis of high quality iron oxide nanoparticles. Because the iron precursor is injected directly into a heated solvent, this method removes the temperature ramp rate dependence that has previously been cited as important for control of particle nucleation[44, 84]. Further, we intend to examine the effect of varying the oleic acid ligand to iron precursor ratio in the reaction, which has been previously been demonstrated as a means by which particle nucleation and growth can be controlled[81, 105, 107].

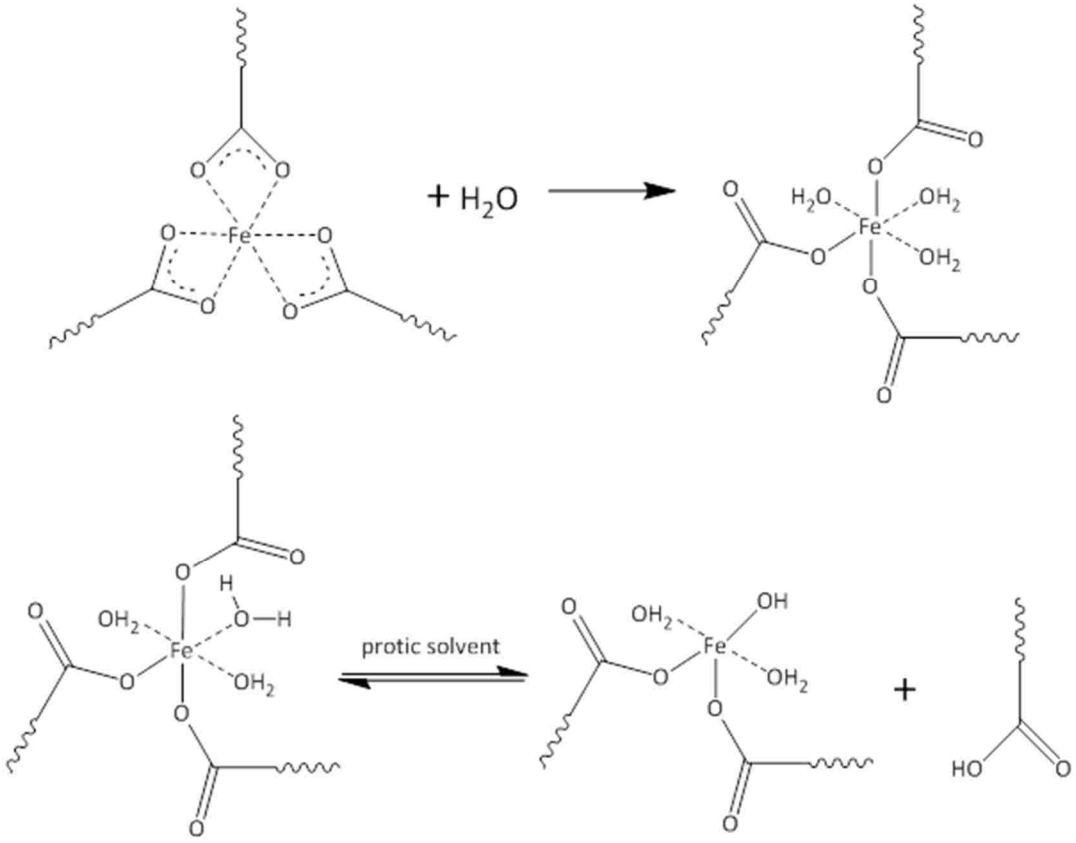

Scheme 4-2. The effect of water on the stoichiometry of iron(III) carboxylate, where ∿∿∿ represents a hydrocarbon chain.

4.2 Experimental

All chemical transformations were carried out with the rigorous exclusion of air and water using standard glovebox and Schlenk-line techniques. Pentane, acetonitrile, and toluene were purchased as anhydrous solvents from Sigma-Aldrich (St. Louis, MO) and used as received. Oleic acid (99%) was purchased from Alfa Aesar (Ward Hill, MA) and dried at 70°C under vacuum for 24 h. Octadecene was purchased from Acros Organics (Pittsburgh, PA) and degassed prior to use. Anhydrous iron(III) chloride was purchased from Strem Chemicals (Newburyport, MA) and Alfa Aesar and used as received. Sodium oleate was purchased from Sigma-Aldrich and dried under vacuum (20 mTorr) at 70 °C for approximately 3 days. To ensure dryness, FTIR spectroscopy was used to confirm the disappearance of the broad –OH peak contributed by water at 3400 cm^{-1}.

4.2.1 Precursor synthesis

The conventional material was prepared according to a literature procedure[108]. Specifically, 1.62 g of anhydrous $FeCl_3$ (10.0 mmol) was dissolved in 10 mL of distilled water. Added to this solution were 9.13 g (30 mmol) of sodium oleate, 20 mL of ethanol, 5 mL of distilled water, and 30 mL of hexane. This mixture was vigorously stirred while the temperature was maintained between 50°C and 70°C for 4 hours under an inert gas environment. At that time, the reaction was allowed to cool to room temperature and the deep red organic layer was separated from the aqueous layer. The organic phase was washed three times with 10 mL of distilled water in a separation funnel, followed by evaporation of the hexane solvent

under vacuum. The product (a dark red-brown material with a semi-solid consistency) was fully dried under vacuum (20 mTorr) at a temperature below 50°C for 24 hours.

The anhydrous iron(III) oleate was prepared by the very slow (over 72 hrs), incremental addition of three equivalents of sodium oleate to a magnetically stirred solution of one equivalent of anhydrous iron(III) chloride in toluene. As small amounts of sodium carboxylate dissolved, the solutions became dark green. The solutions were allowed to stir for an additional 24 hours, after which the toluene was completely removed in vacuo over a 12 hour period. Pentane was added to the remaining material with stirring to dissolve the iron(III) oleate. The mixture was centrifuged and decanted to remove any precipitated NaCl. The solution was thoroughly washed with anhydrous acetonitrile to remove all traces of NaCl. After removing the pentane under vacuum, the anhydrous iron(III) oleate was characterized using FTIR spectroscopy. Three separate samples were prepared in this fashion to test the batch-to-batch variation in synthetic method.

4.2.2 Nanoparticle synthesis

Reproducibility of the iron(III) oleate precursors was tested by three separate nanoparticle synthesis experiments. To briefly describe the reaction methodology, a flask containing solvent was heated to the desired temperature, at which point the iron precursor solution was rapidly injected. The first three experiments tested three prepared anhydrous iron(III) oleate compounds, while the following three

experiments looked at the effect of varying oleic acid concentration in the reaction. The details of the reaction set up are described below.

4.2.2.1 Preparation of iron precursor solution for injection

Iron (III) oleate, as prepared, is a semi-solid compound that is not amenable to injection by a syringe. Therefore, it was necessary to use a carrier solvent that the iron oleate compound could be suitably dispersed in for injection. For these reactions, oleic acid was chosen as the carrier. In a typical reaction, a stock solution was prepared that contained approximately 200 mg (0.22 mmol) of iron(III) oleate in 0.5 mL (1.59 mmol) of oleic acid. Any deviance from these exact quantities was compensated for by maintaining the oleic acid to iron oleate molar ratio of 7.07:1. The iron oleate was fully dispersed in oleic acid with magnetic stirring and gentle heating (60°C).

4.2.2.2 Reaction set up

For the first series of experiments, 3.47 g (11.11 mmol) of docosane solvent (4.0 mL volume) was added to a 100 mL 3-neck flask (Table 4-1). In the subsequent set of experiments testing the effect of oleic acid in solution, a 2.0 mL reaction volume with different amounts of docosane and oleic acid were added to the flask (Table 4-2).

Table 4-1. Reproducibility study: iron oxide nanoparticle synthesis conditions using anhydrous iron oleate precursors.

Anhydrous Iron Oleate Sample	Reaction Flask		Precursor	
	Docosane (mmol)	Oleic acid (mmol)	Iron oleate (mmol)	Oleic acid (mmol)
1	11.11	-	0.222	1.57
2	11.11	-	0.226	1.59
3	11.11	-	0.223	1.58

Table 4-2. Size control study: Increasing the concentration of oleic acid in solution.

Anhydrous Iron Oleate Sample	Reaction Flask		Precursor		Total oleic acid (mmol)
	Docosane (mmol)	Oleic acid (mmol)	Iron (III) oleate (mmol)	Oleic acid (mmol)	
1 05-83	4.96	-	0.224	1.58	1.58
1 05-85	3.72	1.57	0.223	1.58	3.15
1 05-91	2.48	3.15	0.223	1.58	4.73

The experimental apparatus is shown in Figure 4-1. One neck of the reaction flask was fitted with a Claisen adapter to provide connection of a flow adapter for inflow of N_2 gas and a port sealed with a rubber stopper for later injection of iron precursor. The opposite neck of the flask was fitted with a jacketed condenser, on top of which, a second, high efficiency coil condenser was added, and a hose adapter for connection to a bubbler for outflow of N_2 from the reaction. The center neck of the reaction flask was fitted with a stirrer bearing, through which a precision

ground glass stir rod with a Teflon stir blade was attached. To ensure a rigorously air-free atmosphere during synthesis, the reaction vessel was assembled in a glovebox, sealed, and rapidly connected to a Schlenk line with flowing N_2. The ground glass stir rod was connected to a compact overhead stirrer (Caframo,) and stirring was set to 350 RPM. The condensers were connected in series to a recirculating water reservoir heated to 58°C to allow docosane vapors to reflux while preventing solidification in the condenser. The reaction flask was rapidly heated to 360°C using a molten metal bath (Bolton 175F low melting point alloy) heated by cartridge heaters using a custom designed National Instruments temperature control interface. As soon as the molten metal temperature was stable, 0.5 mL of the prepared iron precursor solution was rapidly injected into the reaction flask. Nucleation of nanoparticles was observed by a darkening of the reaction solution from dark brown to black, and the reaction was allowed to age for several minutes before an aliquot was withdrawn for characterization. Aliquots withdrawn from the reaction vessel were suspended in hexanes and loaded into borosilicate glass capillaries for size analysis using SAXS.

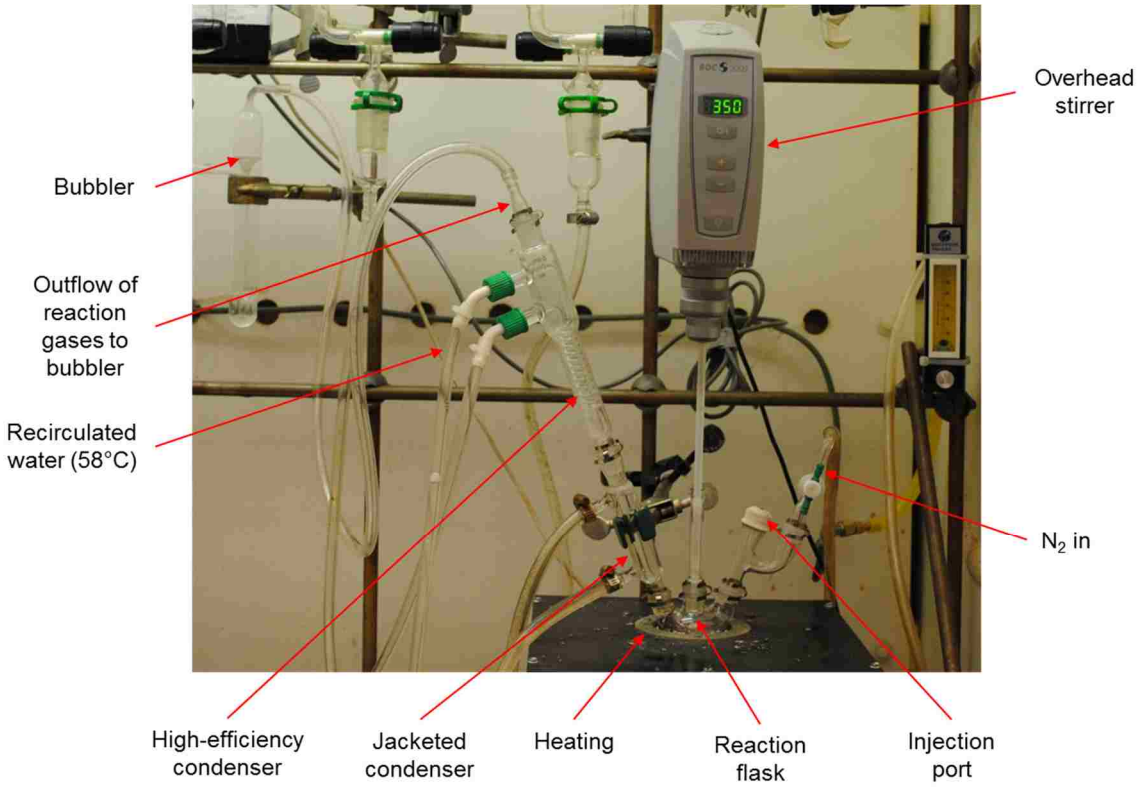

Figure 4-1. Experimental setup for all reactions.

4.2.3 FTIR Spectroscopy

Infrared spectra of anhydrous iron oleate samples were collected on a Bruker IFS 66/S nitrogen-purged infrared spectrophotometer (Bruker Optik GmbH, Germany). Anhydrous KBr pellets or CCl_4 solutions of the iron carboxylates were prepared and measured with 4 cm^{-1} resolution using a room temperature DTGS detector.

4.2.4 Small Angle X-Ray Scattering (SAXS)

Concentrated solutions of samples suspended in hexanes were injected into glass capillary tubes with a 1.0 mm diameter (Charles Supper Company, Natick, MA). Samples were analyzed using a Rigaku SmartLab diffractometer system with the SmartLab Guidance system control software. Cu-K-alpha radiation (40 kV, 44 mA) was used in transmission geometry with a scintillation detector. Data analysis was performed using Rigaku NANO-Solver v.3.5 software, applying a spherical model, and calculating a volume average diameter.

4.3 Results and discussion

4.3.1 Iron Oleate Precursor

To better understand the role of the iron oleate precursor in the formation of iron oxide nanoparticles, it was necessary to prepare homoleptic iron(III) oleate. This material would have to be anhydrous, unlike the conventionally prepared material, to prevent the influence of water on the stoichiometry and decomposition pathways of the pure compound. Different binding modes of the carboxylate ligand in the conventional and anhydrous iron(III) oleate are expected, and can be used to differentiate between two compounds.

4.3.1.1 FTIR Spectroscopy

From Figure 4-2a, the FTIR spectrum of conventional iron(III) oleate reveals three areas of interest: first, there is a wide band at 3440 cm^{-1} that can be assigned to ν(O–H) vibrations, five bands in 1400 – 1700 cm^{-1} region due to ν(C–O) vibrations

coupled to ν(C–C) vibrations, and the small band at 604cm^{-1} assigned to δ(Fe_3O) or δ(FeOH) vibrations[109]. In addition, there are expected peaks from ν(C–H) vibrations at 2856cm^{-1} and 2927cm^{-1} [110]. The ν(O–H) vibrations at 3440cm^{-1} manifest the presence of water in the material[111], whereas the peak at 1711cm^{-1} is indicative of the presence of free oleic acid[112].

FTIR of the anhydrous iron(III) oleate could only be performed under rigorously dry conditions. This green material would quickly become yellow-orange on nominally dry KBr plates, necessitating extensive drying of the KBr. The spectrum of this material, shown in Figure 4-2b ,demonstrates the absence of ν(O–H) vibrations and simpler pattern of ν(C–O) stretches, including the absence of 1711cm^{-1} band, implying that no unbound oleic acid is present in the sample.

The anhydrous material would rapidly change color upon exposure to air and the resulting FTIR spectrum was compared to that of the conventional material (Figure 4-2c). These spectra are remarkably similar, suggesting the same metal-ligand bonding modes for both materials. It is therefore critical to prevent the exposure of the anhydrous iron(III) oleate to air/moisture, as it rapidly undergoes the transformation to the conventional material.

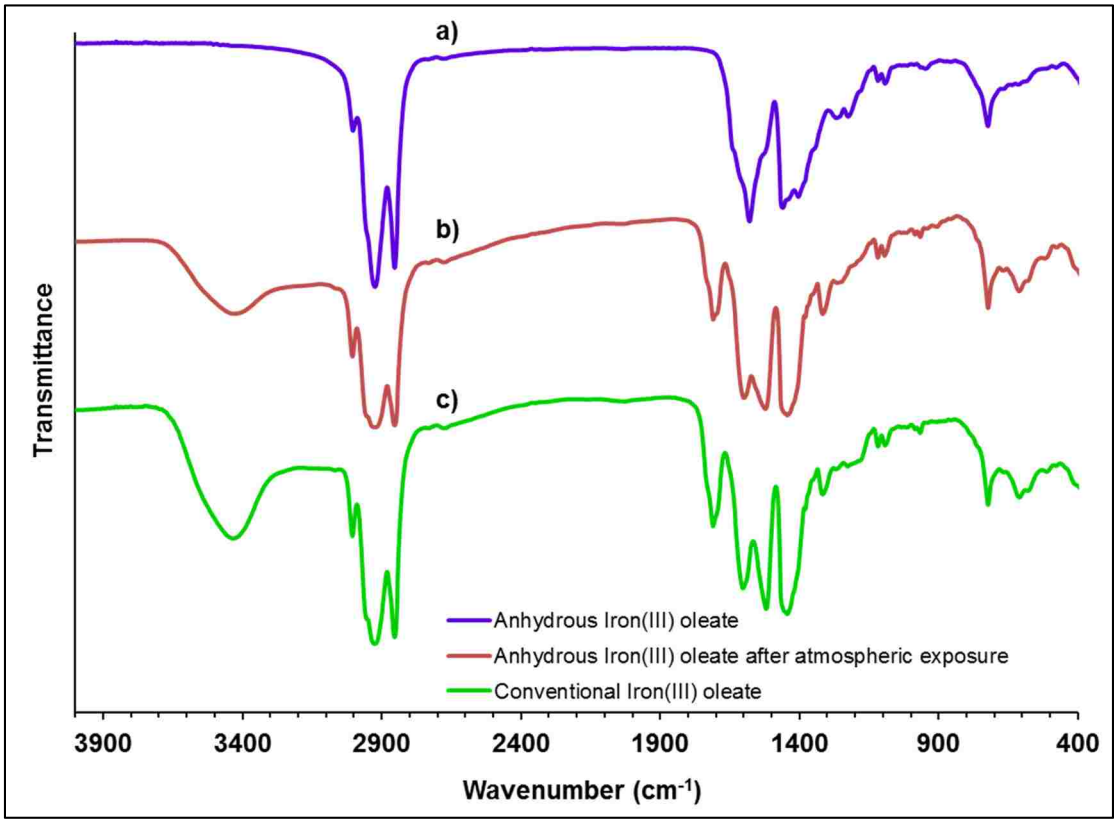

Figure 4-2. FTIR spectra of a) *conventional* iron(III) oleate, and anhydrous iron (III) oleate b) before and c) after atmospheric exposure.

4.3.2 Nanoparticle syntheses

Three anhydrous iron oleate samples, labeled '1,' '2,' and '3' were used for all studies. The first set of experiments was performed to determine the batch-to-batch reproducibility of iron oxide nanoparticle synthesis by injecting 0.5 mL precursor solution into 4.0 mL of docosane solvent. The results of these experiments as characterized by SAXS are presented in Table 4-3. The raw SAXS data and fits are given in Figure 4-3, and the corresponding TEM images in Figure 4-4. There is a 15 – 20% difference between the volume average diameter calculated using SAXS and the volume average diameter calculated from TEM

measurements. This number would be expected to be in better agreement if more particles were sampled using TEM image analysis.

Table 4-3. Reproducibility study: Summary of SAXS data for nanoparticle synthesis using anhydrous iron oleate precursors.

Sample (Experiment)	**Observed nucleation (min)**	**Aliquot withdrawal (min)**	**SAXS Diameter (nm)**	**Size Dispersity**
1	10	11.5	7.8	15.1%
2	13.5	15	12.0	12.8%
3	12.5	15	10.9	12.3%

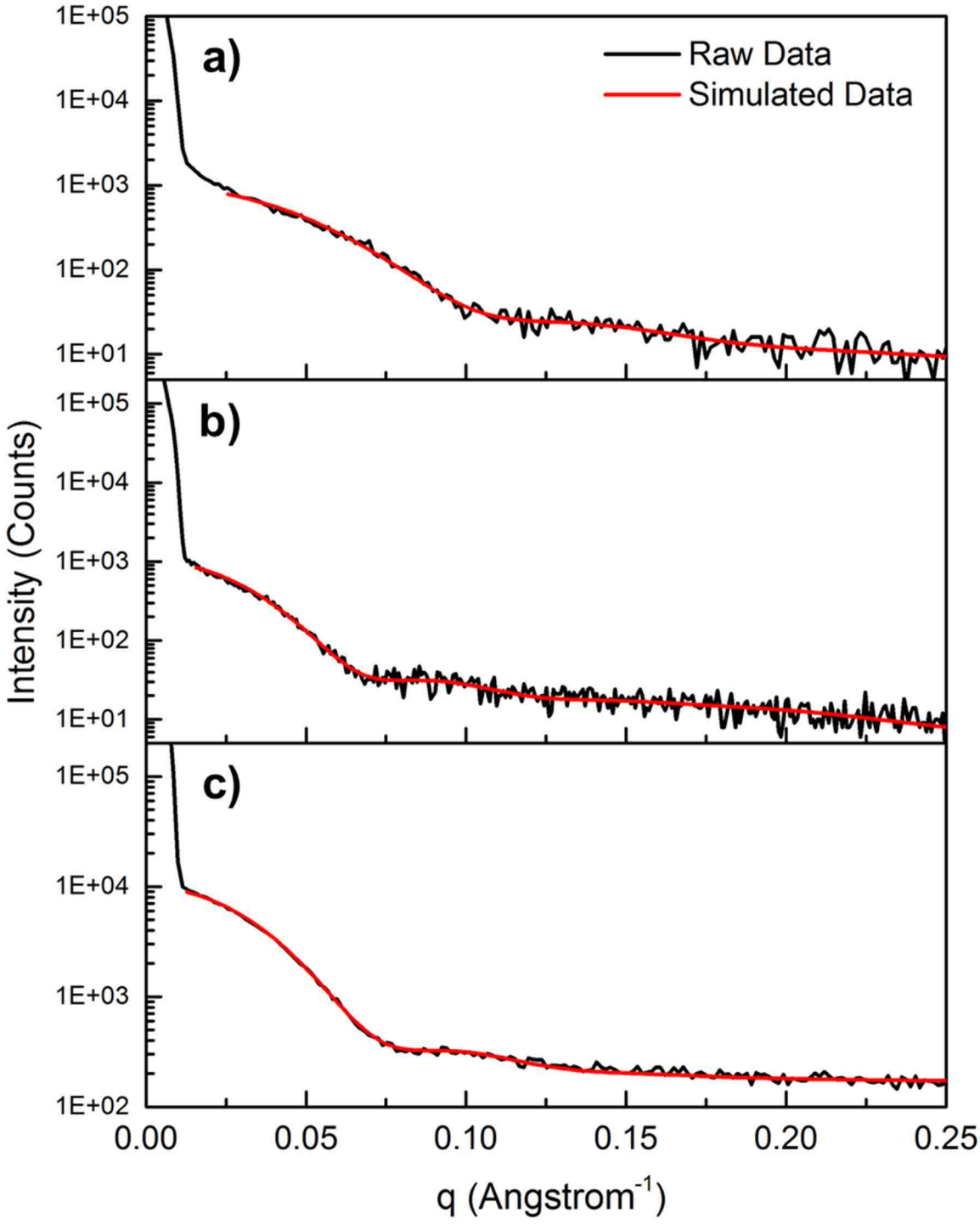

Figure 4-3. Raw SAXS data and fits for samples corresponding to Table 4.3. a) Sample 1, b) Sample 2, c) Sample 3.

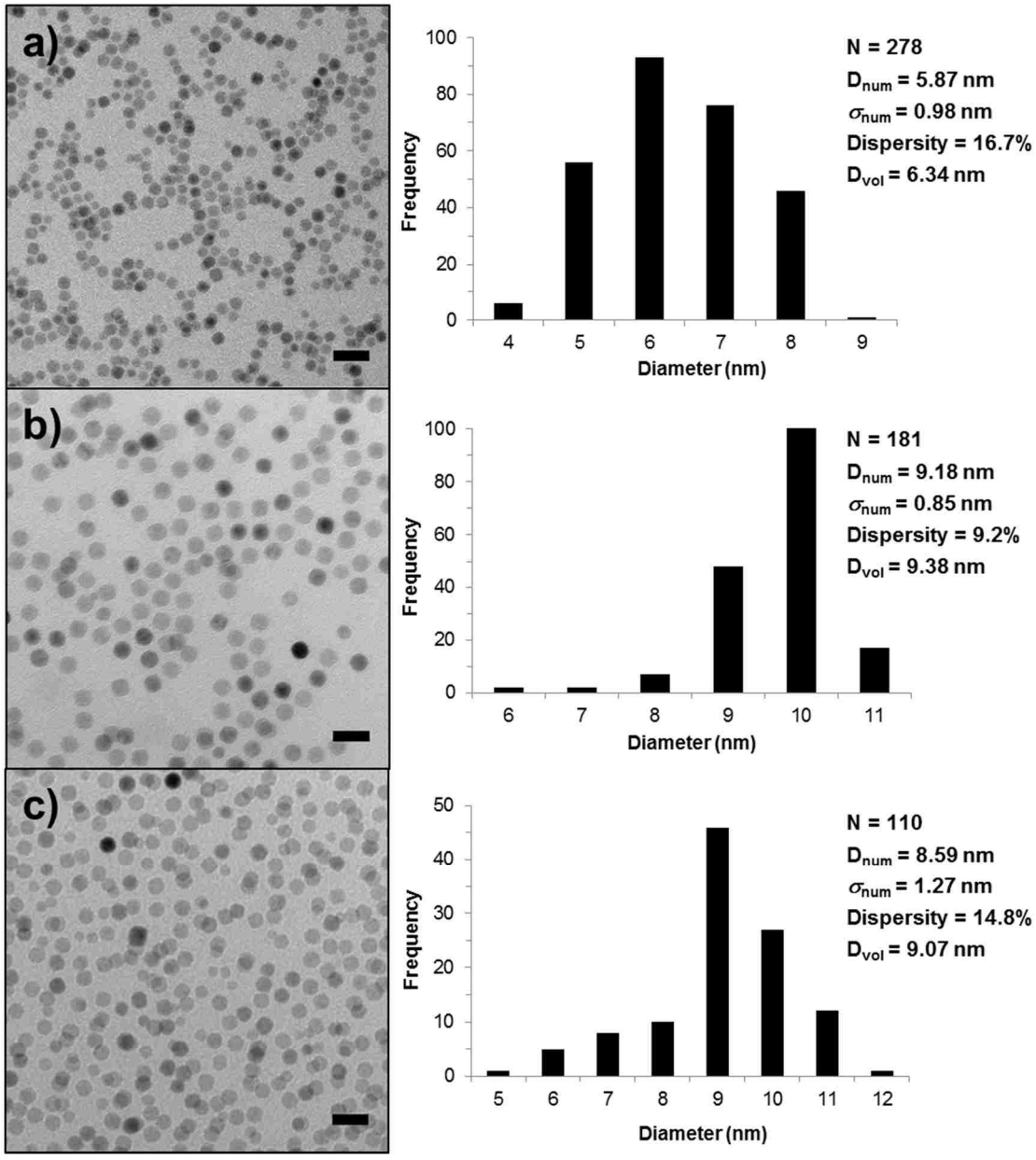

Figure 4-4. TEM images and accompanying histograms for samples corresponding to Table 4.3. a) Sample 1, b) Sample 2, c) Sample 3. The scale bars represent 20 nm.

Table 4-3 illustrates that the time required for particles to nucleate is significantly different for each sample, with an apparent correlation between nucleation time and particle size at the time the aliquot was withdrawn. The earliest nucleation time was observed for Sample 1, which produced particles of the smallest size and the highest size dispersity. The longest nucleation time was observed for Sample 2, which produced the largest particles with reduced size dispersity.

Each anhydrous precursor and nanoparticle synthesis were carried out in the same manner, so it is not clear why such a variation in nucleation times and resulting particle sizes should be observed. One possibility is that by mixing the anhydrous iron oleate with oleic acid prior to injection, the structure of the synthesized iron oleate complex changed in a non-reproducible way (e.g., the number and binding of oleate molecules to an iron ion or ions). The stability of the overall precursor complex could ultimately result in variation of nucleation times. A less ambiguous study of iron(III) oleate decomposition might be accomplished if a non-interacting solvent, such as octadecene, was used to prepare the stock solution for injection.

The second series of experiments used the same iron(III) oleate sample to demonstrate the effect of oleic acid concentration on the properties of the synthesized particles. The volume for all reactions was decreased from 4 mL in the previous set of experiments to 2 mL in the current set of experiments, effectively increasing the molarity of oleic acid in the reaction. The results of those experiments as characterized by SAXS are presented in Table 4-4. The raw SAXS

data and fits are given in Figure 4-5, and the corresponding TEM images in Figure 4-6.

Table 4-4. Size control study: Summary of SAXS data showing the effect of increasing concentration of oleic acid in solution.

Sample (Experiment)	Total oleic acid (mmol)	Observed nucleation (min)	Aliquot withdrawal (min)	SAXS Diameter (nm)	Size Dispersity
1(a)	1.58	20	24.5	8.0	15.4%
1(b)	3.15	39	42	10.2	10.2%
1(c)	4.73	82.5	86	14.9	9.2%

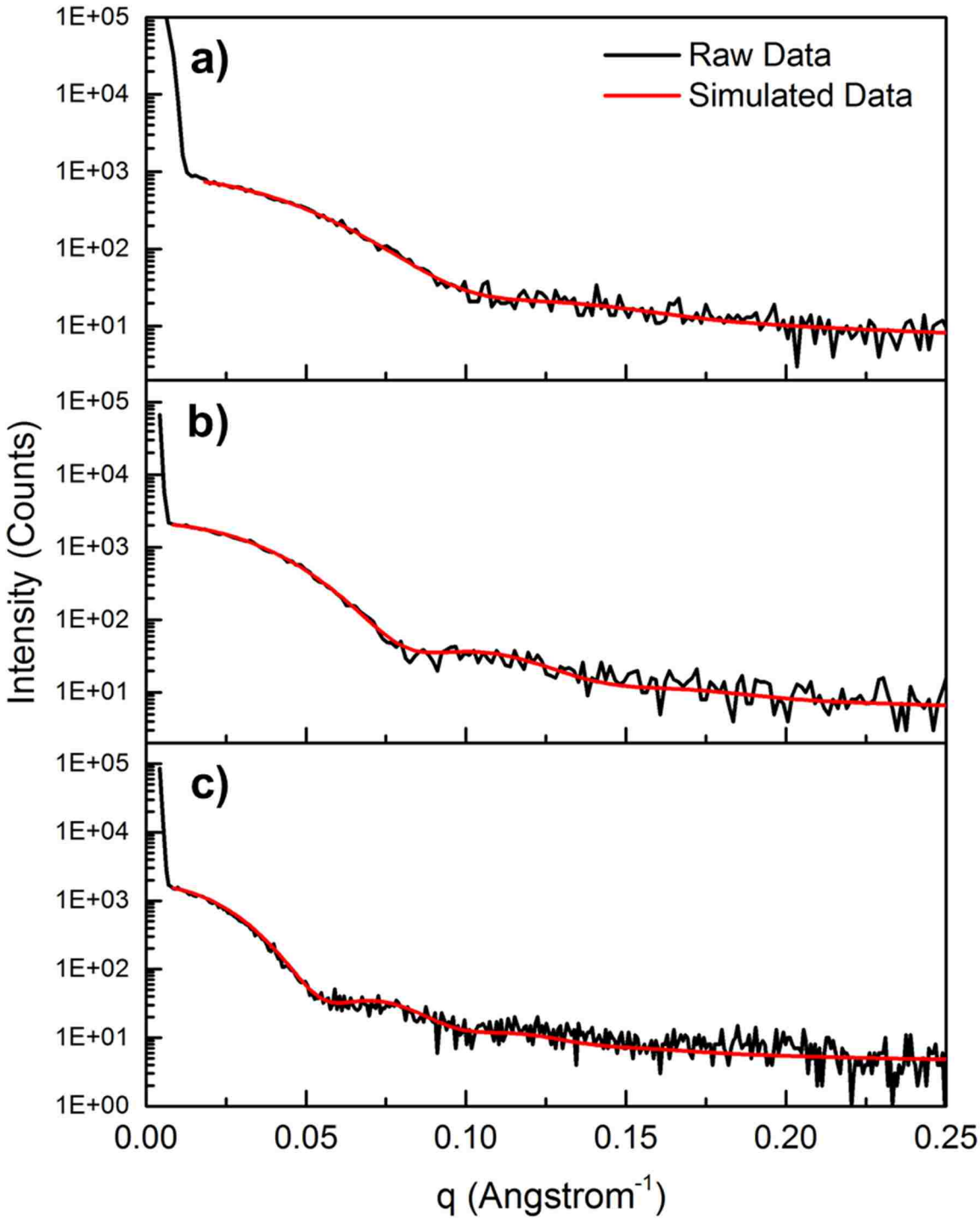

Figure 4-5. Raw SAXS data and fits for samples corresponding to Table 4.4. a) Sample 1(a), b) Sample 1(b), c) Sample 1(c).

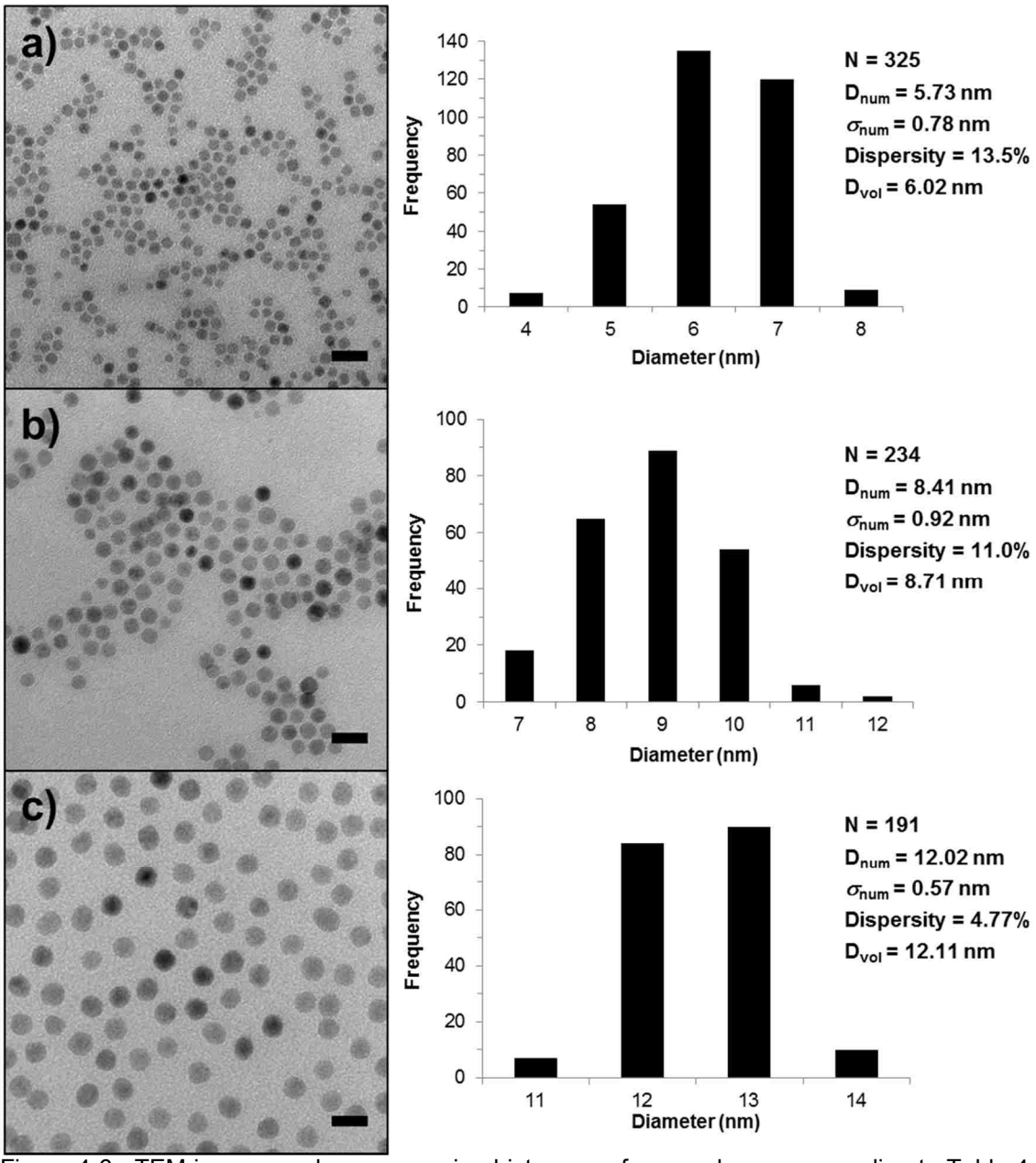

Figure 4-6. TEM images and accompanying histograms for samples corresponding to Table 4.4. a) Sample 1(a), b) Sample 1(b), c) Sample 1(c). The scale bars represent 20 nm.

From Table 4-4, it is clear that each increase in oleic acid resulted in a doubling of nucleation time and an increase in the resulting particle size. This is indicative of the role oleic acid has in increasing the energy barrier to nucleation. The presence of excess oleic acid likely increases the equilibrium solubility of the iron species in solution. This could, in turn, require an increase in the minimum size of the critical nucleus that can resist dissolution. Increasing the oleic acid concentration also appears to have a favorable effect on size dispersity, which decreased significantly from over 15% to nearly 9% as confirmed by SAXS measurements. Additional studies with increased oleic acid concentration would confirm the trend seen in these experiments. However, the results imply that the concentration of free oleic acid in solution is important for achieving size control in this system.

4.4 Conclusions

The purity of the precursor used to synthesize magnetite nanoparticles has been shown to be crucially important to achieving reproducibility in nanoparticle synthesis. Iron(III) oleate prepared by any method that has included atmospheric exposure results in the formation of a non-stoichiometric compound. As a result, published results of magnetite nanoparticles using this material as a precursor are certainly less reproducible than those using a stoichiometric precursor. True, stoichiometric iron(III) oleate was prepared using an air- and moisture-free procedure. The hot injection method, previously applied to semiconductor nanoparticle synthesis, was used to synthesize iron oxide nanoparticles. The iron(III) oleate precursor was demonstrated to be sensitive to mixing with oleic acid

prior to injection, making the results of the reproducibility study difficult to interpret. However, there was a demonstrable effect of excess oleic acid in the reaction solution on the size and resulting size dispersity of synthesized nanoparticles. Oleic acid concentration can be used tune the size of spherical particles with low shape and size dispersity important for controlling the resulting magnetic properties.

Chapter 5 – In Situ Generation of Iron Oleate for Synthesis of High Quality Iron Oxide Nanoparticles

5.1 Introduction

Iron oxide nanoparticles have been studied extensively and are among a small class of nanomaterials that have found utility outside of the laboratory. Owing to their unique magnetic properties at the nanoscale and ease of synthesis, iron oxide nanoparticles have found a number of novel applications in industrial and biomedical applications[77, 113]. However, reproducibly maintaining control of particle size, morphology, and magnetic properties between reactions limits their potential in applications sensitive to these attributes[24]. A number of synthetic approaches for nanoparticle iron oxide have been reported, with thermolysis of iron-containing precursors yielding nanoparticles with superior properties (e.g., low size dispersity, single crystal, shape control)[42-44, 114]. Thermolytic synthesis of iron oxide nanoparticles involves the decomposition of an iron-containing precursor in a high boiling point solvent. The morphology, size, and colloidal stability of the synthesized iron oxide nanoparticles are in part determined by the ligand(s) used in the reaction, which are typically long-chain hydrocarbons with carboxylic acid, alcohol or amine functionalities that bind to and stabilize the nanoparticles[43]. Our goal is to identify a synthetic method that reproducibly yields high quality nanoparticles specifically by eliminating the variability introduced by the composition, purity, and stoichiometry of the iron precursor. Here, we present a systematic study of the thermal decomposition of iron acetylacetonate ($Fe(acac)_3$)

in oleic acid, identify the formation of iron oleate as an intermediate compound, and characterize the resulting iron oxide nanoparticles.

One of the most popular methods of iron oxide nanoparticle synthesis is the thermal decomposition of iron oleate in a high boiling point solvent[35, 44, 45]. However, iron oleate is not commercially available and must be custom synthesized for this reaction[44]. The standard reaction to form iron oleate is deceptively simple, involving the mixing of sodium oleate with iron chloride. The resultant material, however, resists crystallization making purification challenging. Carboxylate anions can bind to metal atoms through various coordination schemes including mono-, bi-, tri-, or tetradentate interactions[99, 100], implying that different stoichiometries are possible for the combination of iron and oleic acid. Bronstein et al. have verified spectroscopically that the amount of oleate coordinated to the iron ions varies depending on the preparation method and is sensitive to factors including washing, aging and storage conditions of the prepared iron oleate compound[83]. Differences in stoichiometry of the iron precursor used to synthesize magnetic nanoparticles obviously impact the reproducibility of iron oxide nanoparticle syntheses.

Despite the challenges associated with reproducibly synthesizing an iron oleate precursor, it is an extremely advantageous material for the synthesis of iron oxide nanoparticles. Nanoparticles synthesized through the high temperature thermal decomposition of iron oleate can be made to have narrow size dispersity and excellent magnetic properties; moreover, the reaction is highly scalable[44]. An ideal

reaction would keep the advantages of the iron oleate precursor, but use only commercially available, stoichiometric compounds. Here, we explore the in situ generation of iron oleate to remove the non-stoichiometric starting material from the reaction.

Iron acetylacetonate ($Fe(acac)_3$) is commercially available as a high purity, crystalline material that is safe, air-stable, inexpensive, and has been used as an iron precursor in the thermolytic synthesis of high quality iron oxide nanoparticles using a variety of solvents and ligands[41, 81, 115]. Li et al. demonstrated the synthesis of 24 nm iron oxide particles with narrow size and shape dispersity by thermolysis of $Fe(acac)_3$ in oleic acid[41]. In this reaction, oleic acid acts as both a high boiling point solvent and a stabilizing ligand for the iron oxide nanoparticles. Li et al. postulate that the reaction proceeds with oleic acid reducing $Fe(acac)_3$ to form Fe(II) oxide particles. Using a similar synthetic approach, we propose that synthesis of iron oxide nanoparticles under such conditions proceeds via the generation of an iron oleate intermediate. This approach provides stoichiometric control over the reaction precursors, while providing a high quality nanocrystalline product from the intermediate iron oleate compound.

Here, we use Fourier transform infrared (FTIR) spectroscopy to confirm that the decomposition of $Fe(acac)_3$ in oleic acid results in the formation of an intermediate iron oleate compound (Figure 5-1). Although the creation of an iron oleate intermediate in this manner has been suggested previously[42, 116], to our knowledge, this is the first detailed spectroscopic study performed over the course

of an entire synthesis. Further, we show that thermal decomposition of the iron oleate intermediate results in the formation of wüstite ($Fe_{1-x}O$), which can be controllably converted to magnetite (Fe_3O_4) by oxidation at relatively low temperature under ambient atmosphere.

5.2 Experimental

5.2.1 Iron oxide nanoparticle synthesis via in situ synthesis of iron oleate

The one-pot synthesis method of Li et al. for the growth of 24 nm magnetite nanoparticles was adapted for the reported experiments[41]. For FTIR studies, a 100 mL three-necked round bottom flask was charged with 3.6 g (10.2 mmol) $Fe(acac)_3$ (99+%, Acros Organics, Fair Lawn, New Jersey) and 15 mL (47.3 mmol) oleic acid (technical grade, 90%, Sigma-Aldrich, St. Louis, MO). Reaction flasks were equipped with a magnetic stir bar, a reflux condenser, and a thermocouple for monitoring the reaction temperature. Reactions were performed with vigorous stirring under a nitrogen atmosphere, and heated to 320°C using a heating mantle controlled by a J-KEM 210T PID temperature controller (J-KEM, St. Louis, MO). For FTIR analysis of reaction intermediates, 19 aliquots of approximately 100 µL each were withdrawn at selected time intervals and measured neat. To understand the effect of reagent removal on nanoparticle synthesis, additional reactions without aliquot removal were also performed under the same conditions.

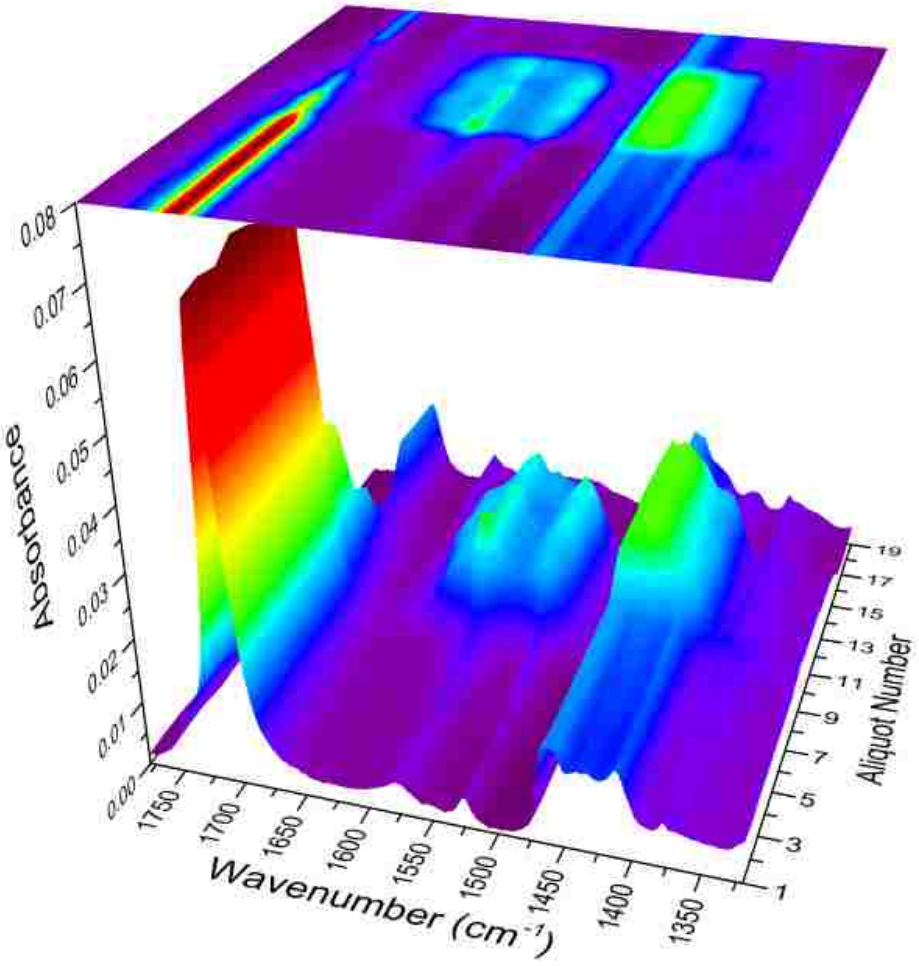

Figure 5-1. Characteristic carbonyl and carboxylate stretches are visible in the region from 1800 – 1300 cm^{-1}. Early in the reaction, the dominant peak arises from unbound oleic acid (νC=O at 1710 cm^{-1}). As the reaction progresses, oleic acid is converted to iron oleate and strong carboxylate stretches ($\nu_{asym}COO^-$ at 1578 cm^{-1}, and ν_{sym}COO- at 1444 cm^{-1}) emerge. Upon formation of particles, iron oleate is consumed and carboxylate stretches disappear.

5.2.2 Spectroscopic Characterization of Reaction Intermediates

5.2.2.1 Fourier Transform Infrared (FTIR) Spectroscopy

Infrared spectra were collected on a Bruker IFS 66vS vacuum evacuated infrared spectrophotometer (Bruker Optik GmbH, Germany). Aliquots were characterized using a grazing angle attenuated total reflectance (GATR) accessory with a fixed 65° incidence angle and a hemispherical germanium crystal (Harrick Scientific Products Inc., Pleasantville, NY). 256 scans of each sample were collected at 2 cm^{-1} resolution from 3400 cm^{-1} to 700cm^{-1} using a liquid nitrogen cooled MCT detector. Extended ATR correction was performed on the collected spectra using Opus 6.5 software assuming an index of refraction of 1.5 for the aliquots. No additional baseline corrections were performed.

5.2.3 Structural and Morphological Characterization

5.2.3.1 Powder X-ray Diffraction (XRD)

Powder diffraction samples were prepared by placing several drops of concentrated nanoparticle suspension onto a silicon substrate and allowing the solvent to evaporate. Powder *X-ray* diffractograms were collected using a Rigaku SmartLab diffractometer system with the SmartLab Guidance system control software for system automation and data collection (Rigaku, The Woodlands, TX). Cu-K-alpha radiation (40 kV, 44 mA) was used with a scintillation detector and diffracted beam monochromator. Data analysis was completed using Rigaku

PDXL analytical software with the ICDD (International Center for Diffraction Data) PDF2 database (release 2010 RDB) for phase identification.

5.2.3.2 Small Angle X-Ray Scattering (SAXS)

Concentrated solutions of samples suspended in hexanes were injected into glass capillary tubes with a 1.0 mm diameter (Charles Supper Company, Natick, MA). Samples were analyzed using a Rigaku SmartLab diffractometer system with the SmartLab Guidance system control software. Cu-K-alpha radiation (40 kV, 44 mA) was used in transmission geometry with a scintillation detector. Data analysis was performed using Rigaku NANO-Solver v. 3.5 software, assuming a spherical particle shape, and calculating a volume average diameter.

5.2.3.3 Transmission Electron Microscopy (TEM)

Samples were prepared by applying a drop of a dilute suspension of nanoparticles in hexanes onto a carbon-coated copper grid (SPI, Westchester, PA) and wicking excess liquid away with a Kimwipe. Bright field TEM studies were performed using a JEOL 1200EX TEM operating at 120 kV (JEOL USA, Inc., Peabody, MA). High resolution images were acquired using a Tecnai F30 G^2 Twin TEM with a 300 keV acceleration voltage. Size analysis of imaged particles was performed using ImageJ software[117]. The size distribution was calculated by deriving the particle diameter from the measured cross-sectional area, effectively assuming a spherical morphology, and calculating a number average and volume average diameter.

5.2.3.4 Superconducting Quantum Interference Device (SQUID) Magnetometry

Magnetization measurements were collected using a Quantum Design MPMS-7 SQUID magnetometer. Samples were prepared by depositing a small amount of the synthesized nanoparticles suspended in hexanes onto the end of a Q-tip™ cotton swab and flame-sealing the sample in an NMR tube under vacuum. Magnetization curves were recorded from -50kOe to +50kOe (-4000 kA/m – +4000 kA/m) at 293K. Data were corrected for the slight paramagnetic signal contributed by the NMR tube at high fields. Zero-field cooled (ZFC) magnetization curves were obtained by cooling the sample to 5K with no applied field, then applying a field of 10 Oe (0.8 kA/m), and recording the magnetization from 5K to 345K. With the 10 Oe field still applied, the sample was then cooled from 345K to 5K to obtain the field-cooled (FC) magnetization. The precise iron mass of each sample was determined destructively by heating the Q-tip™ in a 600°C furnace for 1 hour to incinerate the organic material and then dissolving the iron containing residue in hydrochloric acid. A phenanthroline/Fe^{2+} complex was formed in solution and spectrophotometrically quantified using the concentration of a known dilution[118, 119].

5.3 Results and discussion

5.3.1 Particle formation and growth

Hyeon et al. applied the concepts developed by LaMer and Dinegar as discussed in Chapter 1 in the “heating-up method” for the one-pot, thermolytic synthesis of

iron oxide nanoparticles[45, 120]. In this approach, thermal decomposition of the precursor leads to the increase of monomer units in solution until a critical, supersaturating concentration induces formation of nuclei, and growth proceeds by diffusion of monomer units to the particle surface. We adopt the "heating-up method" to include the in situ synthesis of iron oleate from a crystalline precursor. A simplified reaction is presented in Scheme 5-1.

Scheme 5-1. Proposed reaction scheme for the formation of iron oxide nanoparticles by the heating and decomposition of the iron precursor, $Fe(acac)_3$; the formation and consumption of an iron oleate intermediate; the formation of oleic acid-stabilized iron oxide nanoparticles.

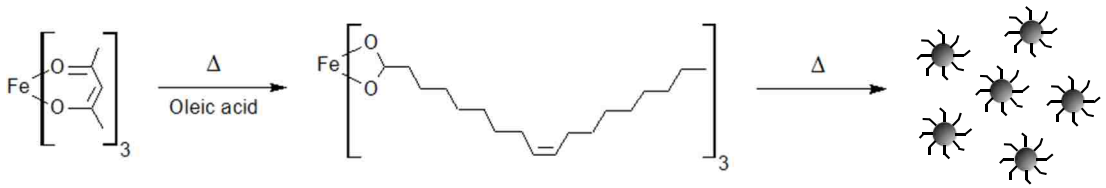

Therefore, we propose the following four step reaction sequence for the current system: 1) Conversion of $Fe(acac)_3$ to iron oleate at temperatures above the decomposition temperature of $Fe(acac)_3$, 2) High temperature decomposition of iron oleate leading to an accumulation of iron oxide precursor (stabilized by oleic acid), 3) nanoparticle nucleation at a critical concentration of the iron oxide precursor to partially relieve supersaturation, and 4) particle growth without nucleation. Evidence for this sequence of reactions was obtained through infrared spectroscopy of the reaction mixture during the course of the reaction.

5.3.2 Characterization of reaction intermediates

5.3.2.1 FTIR Spectroscopy

Fourier transform infrared spectroscopy (FTIR) was chosen as a semi-quantitative method to identify the proposed iron intermediate in sample aliquots. By comparing peaks found in the infrared spectra of reaction aliquots with those known to be characteristic of the vibrations of carboxylate ions occurring in the salts of carboxylic acids, we demonstrate that iron oleate is formed as an intermediate to iron oxide nanoparticle formation. The emergence and later disappearance of specific vibrational frequencies in the carboxylate region of the IR spectra during the reaction can be used to demonstrate the generation and consumption of an iron oleate intermediate (Figure 5-1). The full spectra of the collected aliquots (3400 – 700 cm^{-1}) are presented in Figure 5-2 with the peak assignments of the most significant figures listed in Table 5-1.

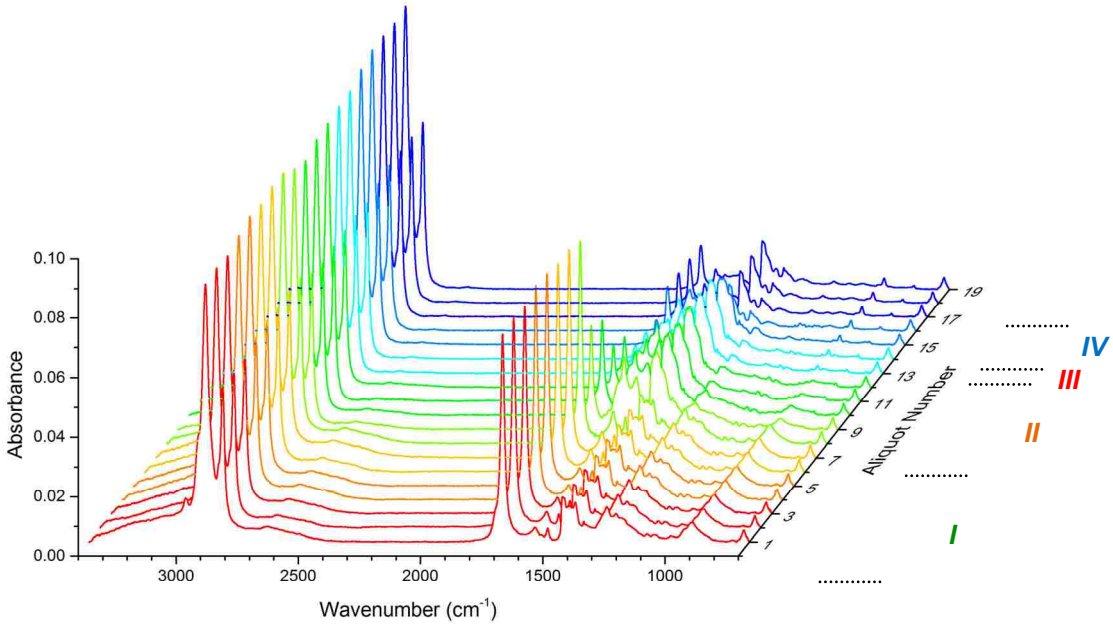

Figure 5-2. FTIR spectra of collected aliquots from 3400 cm^{-1} – 700 cm^{-1}.

Specifically, a brief review of some of the vibrations that are contributed by carboxyl and carboxylate groups in the range of 1800 – 1300 cm^{-1} is beneficial. The C=O stretching vibration (νC=O) in carboxylic acids exhibits a strong band at 1725 ± 65 cm^{-1} [112], and in free oleic acid can be found at 1710 cm^{-1}. Conversion of the carboxylic acid to an iron carboxylate gives rise to the asymmetric COO^- stretch ($\nu_{asym}COO^-$) from 1650–1510 cm^{-1} and the symmetric COO^- stretching vibrations ($\nu_{sym}COO^-$) from 1444–1280 cm^{-1} [83, 112, 121, 122]. In our analysis, we assign the peak at 1578 cm^{-1} to $\nu_{asym}COO^-$ and the peak at 1444 cm^{-1} to $\nu_{sym}COO^-$, consistent with previous studies[83]. It should be noted that C–H vibrations that superimpose on the carboxylate stretches in this region can make precise assignment of wavenumbers challenging[112]. Further, multiple coordination modes

of carboxylate moieties to iron ions may cause additional overlapping vibrations[122]. Though it is conceivable that various carboxylate compounds may be formed during the decomposition of $Fe(acac)_3$[123], the large excess of oleic acid present in the reaction warrants our belief that the carboxylate stretches are contributed predominantly by iron (III) oleate.

Table 5-1. FTIR peak assignments

	Peak (cm^{-1})	Assignment	Comments	Ref.
Phase I	3050 ± 150	–OH stretching vibration from COOH dimers	Broad, disappears with formation of iron oleate	112, 121
	2925	Asymmetric C-H stretches	Strong, constant throughout reaction	112
	2854	Symmetric C-H stretches	Strong, constant throughout reaction	112
	1710	C=O stretch of carboxylic acid	Strong, diminishes with the formation of iron oleate	83, 112, 121
	1589	C-O stretch of $Fe(acac)_3$	Moderate, disappears with the formation of iron oleate	124
	1530	CH stretch of $Fe(acac)_3$	Moderate, disappear with formation of iron oleate	124
	1300 – 1200	–OH in plane deformation	Broad, medium intensity, couples to the C–O stretching vibration, disappears with the formation of iron oleate	112, 121
	1250 ± 80	C–O stretching vibration	Moderate, couples to –OH in plane deformation, disappears with the formation of iron oleate	112
	905 ± 65	–OH out of plane deformation	"V" shaped band, disappears with the formation of iron oleate	112, 121
Phase II	1710	C=O stretch of carboxylic acid	Reaches a minimum in this phase	
	1650 – 1510	Asymmetric COO^- stretches	Reaches a maximum in this phase	83, 112, 121, 122
	1444 – 1280	Symmetric COO^- stretches	Reaches a maximum in this phase	40, 47, 48, 50
Phase III	*Nucleation*			
Phase IV	1710	C=O stretch of carboxylic acid	Intensity increases slightly following the formation of particles	

To illustrate this concept more concisely, four vibrational frequencies considered to be most relevant to this study have been plotted as a function of the reaction progress: 2854 cm^{-1}, 1710 cm^{-1}, and 1578 cm^{-1} (Figure 5-3a). The peak at 2854 cm^{-1} represents alkyl C–H stretches (νC–H), and is expected to remain constant throughout the duration of the reaction. The remaining peaks correspond to νC=O and $\nu_{asym}COO^-$, as discussed previously. An inspection of this plot makes it clear that the asymmetric carboxylate stretch we attribute to iron oleate is initially absent, increases significantly above the background, suddenly drops, then remains at a low level as the reaction terminates. This phenomenon makes it straightforward to divide the reaction into four phases, which we describe as: I. Heating and thermal decomposition of $Fe(acac)_3$, II. Accumulation and decomposition of the iron oleate intermediate, III. Particle nucleation, and IV. Particle growth.

Phase I: Heating and thermal decomposition of $Fe(acac)_3$

During phase I, the reaction mixture is heated from room temperature to 220°C, the decomposition temperature of $Fe(acac)_3$, and the point at which the reaction mixture was observed to boil (Figure 5-3b). Here, the rapid heating of the reaction ceases, despite the temperature controller applying full power to heat the reaction. For an extended period of time, we see only a gradual increase in temperature as the reaction mixture refluxes. The temperature of reflux is consistent and reproducible and is attributed to the release of acetylacetone upon reaching the decomposition temperature of $Fe(acac)_3$. Acetylacetone boils at 140°C, and would be expected to vigorously reflux at this temperature, providing cooling to the

reaction and slowing the heating. Simultaneously, a gradual decrease of the νC=O peak can be observed and is accompanied by a commensurate increase in the $\nu_{asym}COO^-$ peak, as free oleic acid begins to combine with iron liberated during $Fe(acac)_3$ decomposition and iron oleate is formed.

Phase II: Formation and decomposition of iron oleate intermediate

In phase II, the reaction temperature slowly increases from 229°C to about 250°C, despite the continued application of full heating power. At 250°C the reaction resumes its rapid heating and no further boiling is noted, as the byproducts of acetylacetone decomposition have largely escaped the reflux condenser. The time required for this evaporation can be dramatically shortened by omitting the reflux condenser from the reaction apparatus. The reaction then rapidly heats to the reaction set point of 320°C, where it is held for 40 minutes with only minor oscillations in temperature, characteristic of PID controllers. A sharp decline of the νC=O peak and the increase of $\nu_{asym}COO^-$ at the first time point (aliquot 9) indicate the coordination of unbound oleic acid to iron ions forming the iron oleate intermediate. After the initial spike, $\nu_{asym}COO^-$remains relatively constant as the concentration of iron oleate plateaus. The continued decline and near disappearance of νC=O may reflect the high temperature decarboxylation of the carboxylic acid moiety[125]. At the final time point in this phase (aliquot 15), when the reaction has been held at 320°C for 40 minutes, νC=O reaches a minimum.

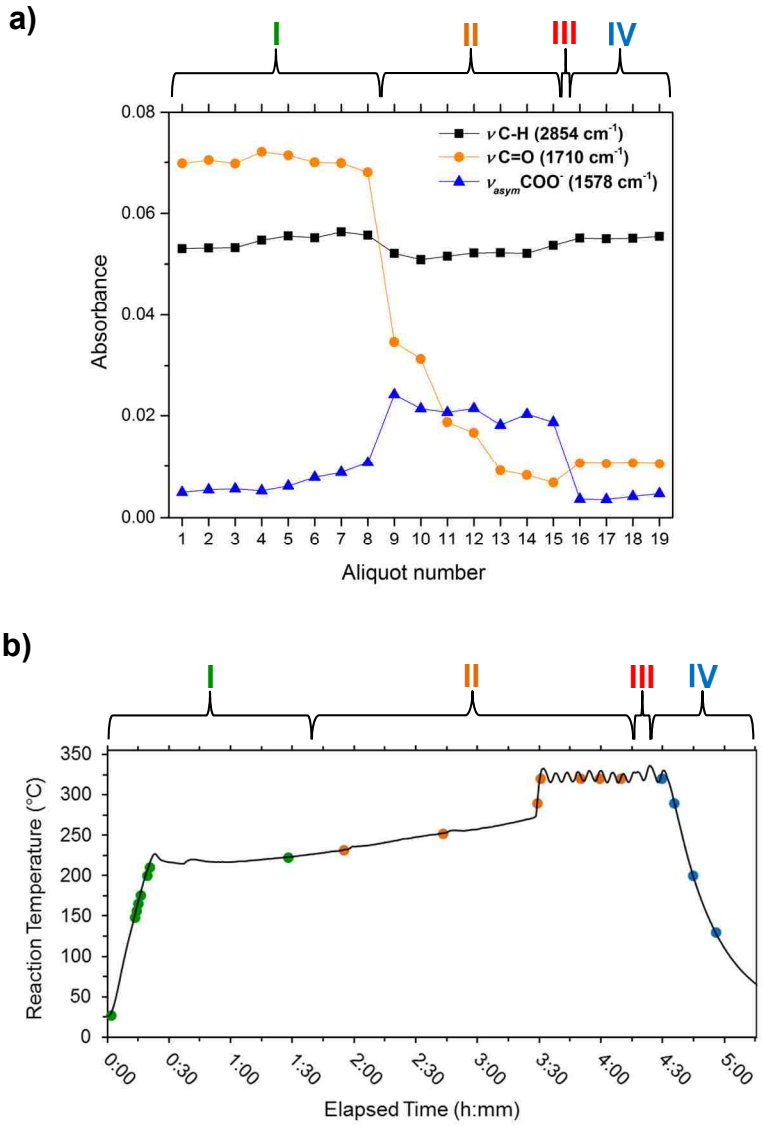

Figure 5-3. a) Selected IR absorbance of successive reaction aliquots are plotted: νC–H is presented for reference, while νC=O and ν_{asym}COO- allow four distinct phases to be identified in the reaction corresponding to (I) heating and thermal decomposition of the iron precursor, (II) formation and decomposition of iron oleate intermediate (III) particle nucleation, and (IV) nanoparticle growth. b) The corresponding reaction temperature profile. Time points for aliquot withdrawals are indicated by filled circles that have been colored to identify the reaction phase.

Phase III: Particle nucleation

Though no aliquots are withdrawn during this brief phase, nucleation of particles during this step can be inferred by analysis of aliquot 15, taken at the end of Phase II and aliquot 16, taken at the beginning of Phase IV. The spectral changes that occur between Phase II and Phase IV are accompanied by a sudden darkening of the reaction solution from a dark orange-brown color to black, indicating the formation of iron oxide nanoparticles.

Phase IV: Particle growth

This phase of the reaction, represented by aliquots 16–19, is spectroscopically characterized by a dramatic decrease in $\nu_{asym}COO^-$, and a slight increase in $\nu C{=}O$. The decrease in $\nu_{asym}COO^-$ is due to a sudden decrease in iron oleate concentration resulting from the rapid growth of nanoparticles, while the increase in $\nu C{=}O$ may be caused by the liberation of oleic acid from the iron oleate. SAXS and TEM analysis of aliquot 16 confirms the presence of large particles, approximately 21 nm in diameter. This range of spectra is characterized by diminished but fairly constant $\nu_{asym}COO^-$ peak, reflecting the near complete consumption of the iron oleate intermediate in the previous phase. The absence of the $\nu_{asym}COO^-$ peak in this region also suggests that additional changes to the particle size/shape dispersity in this regime can be attributed to ripening effects.

5.3.3 Structure and morphology of iron oxide nanoparticles

5.3.3.1 TEM and SAXS Size Analysis

A representative TEM image of particles isolated from aliquot 16 is given in Figure 5-4a, with an accompanying histogram in Figure 5-4b. The number average of particles analyzed by TEM was 18.7 nm (11.9% dispersity) with a volume average particle diameter of 19.44 nm. These measurements agree reasonably well with the volume average particle diameter of 21.0 nm (15.9% dispersity) measured with SAXS (Figure 5-5).

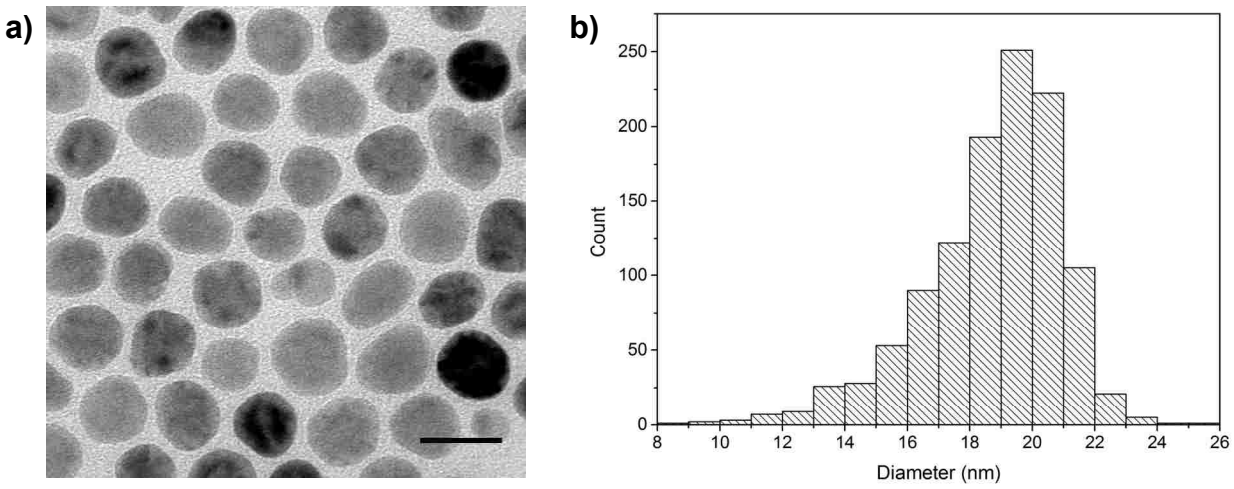

Figure 5-4. a) TEM image of particles isolated from aliquot 16 and b) the accompanying TEM size distribution. The scale bar represents 25 nm.

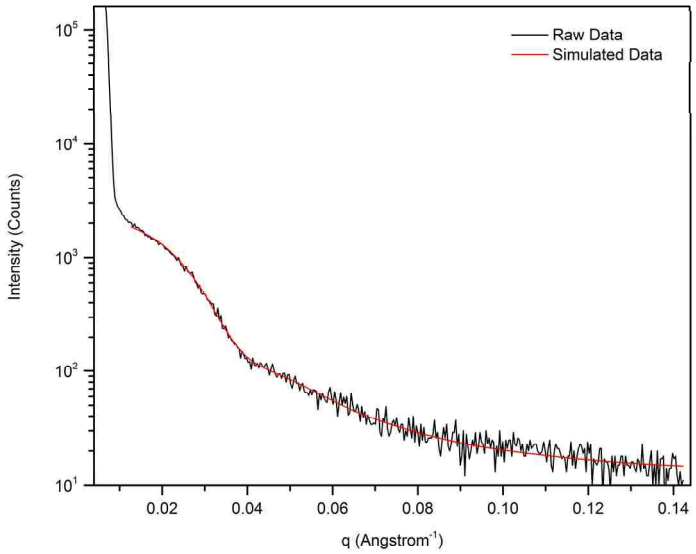

Figure 5-5. Raw SAXS data of particles isolated from aliquot 16 and the fit used to obtain the volume average diameter of 21.0 nm and dispersity of 15.9%.

A representative TEM image of particles synthesized without aliquot removal is presented in Figure 5-6a, along with an accompanying size distribution histogram in Figure 5-6b. TEM analysis of particle size resulted in a number average particle diameter of 25.8 (13.7% dispersity) and a volume average diameter of 27.0 nm. This agreed with the volume average diameter of 27.0 (12.1% dispersity) obtained by SAXS measurements (Figure 5-7).

The TEM images reveal the formation of approximately spherical particles with a size distribution skewed toward smaller sizes, indicative of Ostwald ripening. The quality of the synthesized particles is comparable to particles of a similar size synthesized using a custom synthesized iron oleate precursor[44, 126]. Optimal reaction conditions that minimize ripening effects and allow size control will be discussed in the proceeding chapters. A high resolution TEM image shows that

several of the particles are single crystalline, with parallel lattice planes extending through the particle, while others appear to be polycrystalline (Figure 5-8).

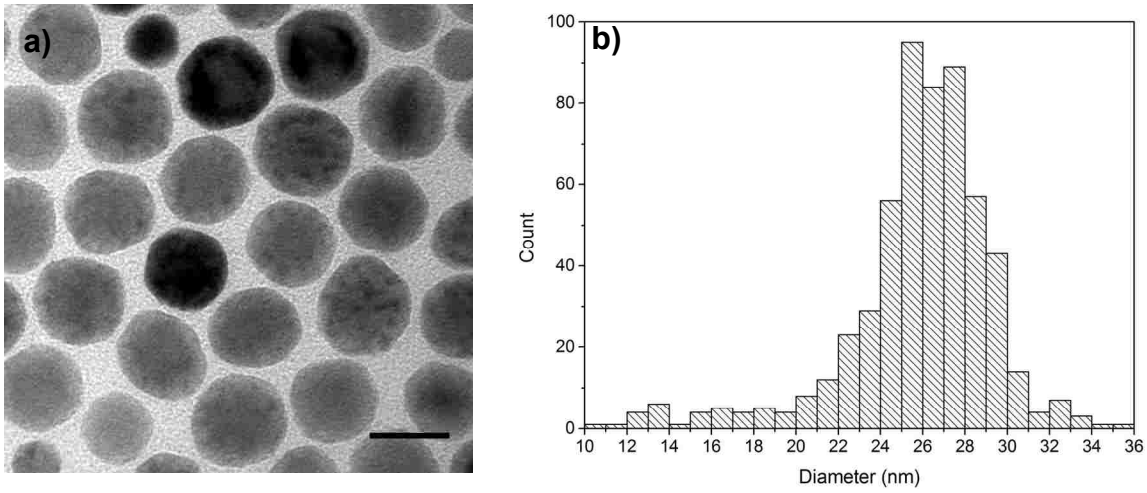

Figure 5-6. a) Representative TEM image of synthesized iron oxide nanoparticles and b) the accompanying TEM size distribution. The scale bar represents 25 nm.

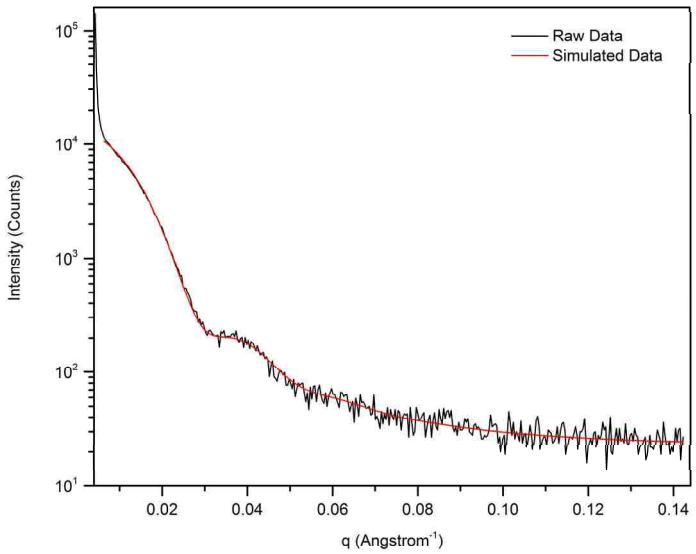

Figure 5-7. Raw SAXS data of particles isolated from a reaction with no aliquots withdrawn and the fit used to obtain the volume average diameter of 27.0 nm and dispersity of 12.2%.

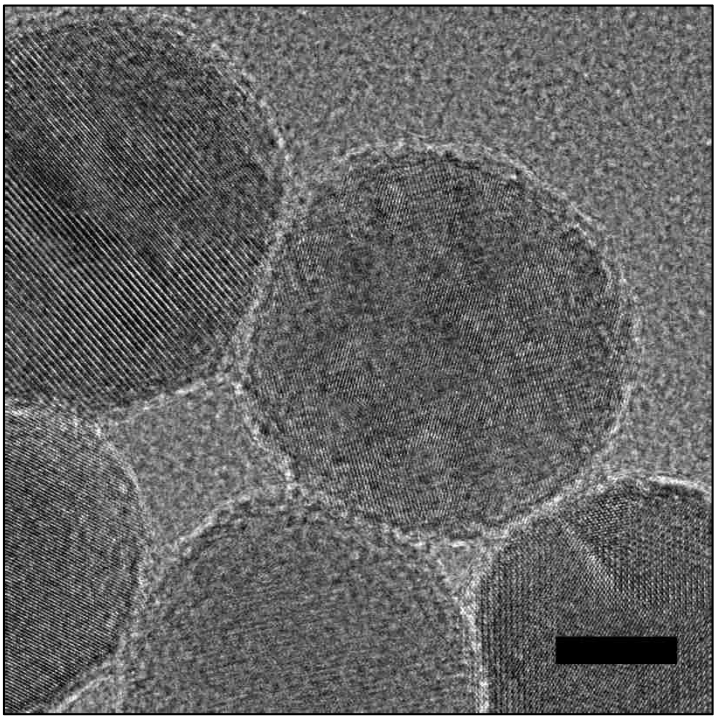

Figure 5-8. HRTEM image shows several single crystalline particles with parallel lattice planes extending through the particle, while others appear to be polycrystalline. The scale bar represents 10 nm.

5.3.3.2 XRD

XRD measurements were performed on particles isolated at the end of a typical reaction performed without aliquot withdrawal. The diffractogram obtained for the as-synthesized nanoparticles was indexed to wüstite ($Fe_{0.925}O$, ICDD 01-089-0686), and magnetite (Fe_3O_4, ICDD 01-076-7165) (Figure 5-9a). Wüstite is a non-stoichiometric ferrous iron oxide with the general formula $Fe_{1-x}O$. The formation of wüstite requires the reduction of Fe^{3+} in the precursor, which may result from the mode of decomposition of the Fe-carboxylate species. One proposed decomposition route involves one of the carboxylates leaving as a neutral radical,

which leads to the formal reduction of Fe^{3+} to Fe^{2+} [125]. At room temperature, $Fe_{1-x}O$ exhibits paramagnetic behavior and exists as a metastable compound that can be converted to α-Fe and Fe_3O_4 through disproportionation or oxidation[63, 68]. The presence of Fe_3O_4 peaks in the diffractogram indicates that some oxidation has taken place during handling and measurement. Complete conversion of $Fe_{1-x}O$ to the desired Fe_3O_4 product can be accomplished by moderate heating of the particle suspension under atmosphere[114]. As-synthesized nanoparticles were oxidized in-situ under atmosphere for six hours at 120°C and the XRD spectrum collected (Figure 5-9b). As evidenced by the XRD data, $Fe_{1-x}O$ peaks have disappeared, Fe_3O_4 peaks initially present in the as-synthesized sample have significantly increased, and several new peaks indexed to Fe_3O_4 have emerged. However, because Fe_3O_4 and Fe_2O_3 peaks overlap in the XRD spectrum, this technique alone is not sufficient to confirm the presence of magnetite. DC SQUID magnetometry was used to verify these findings, as discussed in the next section.

5.3.3.3 SQUID Magnetometry

Magnetometry was performed on particles isolated at the end of a typical reaction performed without aliquot withdrawal. The magnetization curves of unoxidized and oxidized particles at 293K are illustrated in Figure 5-10a. The magnetization per unit mass (σ_{sat}) of the oxidized particles is more than 3.5 times that of the unoxidized particles (99.6 vs. 27.2 $A \cdot m^2/kg$ Fe), indicating the conversion of $Fe_{1-x}O$ to Fe_3O_4 following the oxidation step. The unoxidized particles are, in fact, partially oxidized from exposure to air during handling, as shown in the XRD data,

explaining the modest σ_{sat} value. If the oxidized particles are assumed to be comprised completely of Fe_3O_4, the calculated σ_{sat} is 71.8 $A \cdot m^2/kg$ Fe_3O_4, 78% of bulk Fe_3O_4 at 293K[63], considerably greater than particles of a similar size synthesized using a conventional iron oleate precursor[44].

The temperature dependent ZFC and FC curves are plotted in Figure 5-10b. No definitive blocking temperature (T_B) was identified within the measured temperature range, attributable to the large size of the particles and the maximum temperature limit achievable using the current apparatus. The Verwey transition, a spontaneous increase in magnetization at ~120K that is characteristic of Fe_3O_4, is observed at 111K in this system[70] .

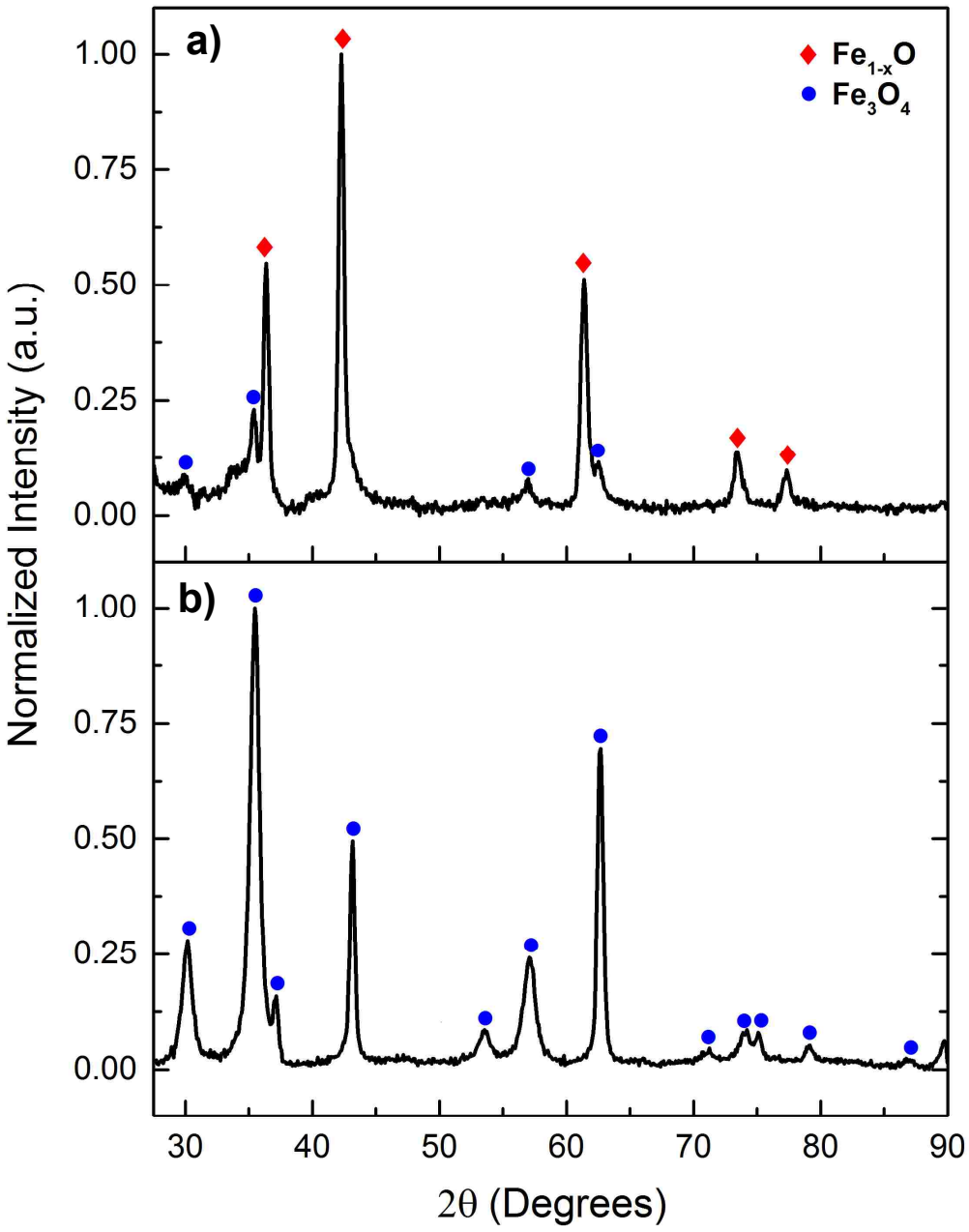

Figure 5-9. XRD diffractograms of a) as-synthesized particles composed predominantly of $Fe_{1-x}O$ with small Fe_3O_4 peaks and b) oxidized nanoparticles showing the disappearance of the $Fe_{1-x}O$ phase and the emergence and growth of Fe_3O_4 peaks.

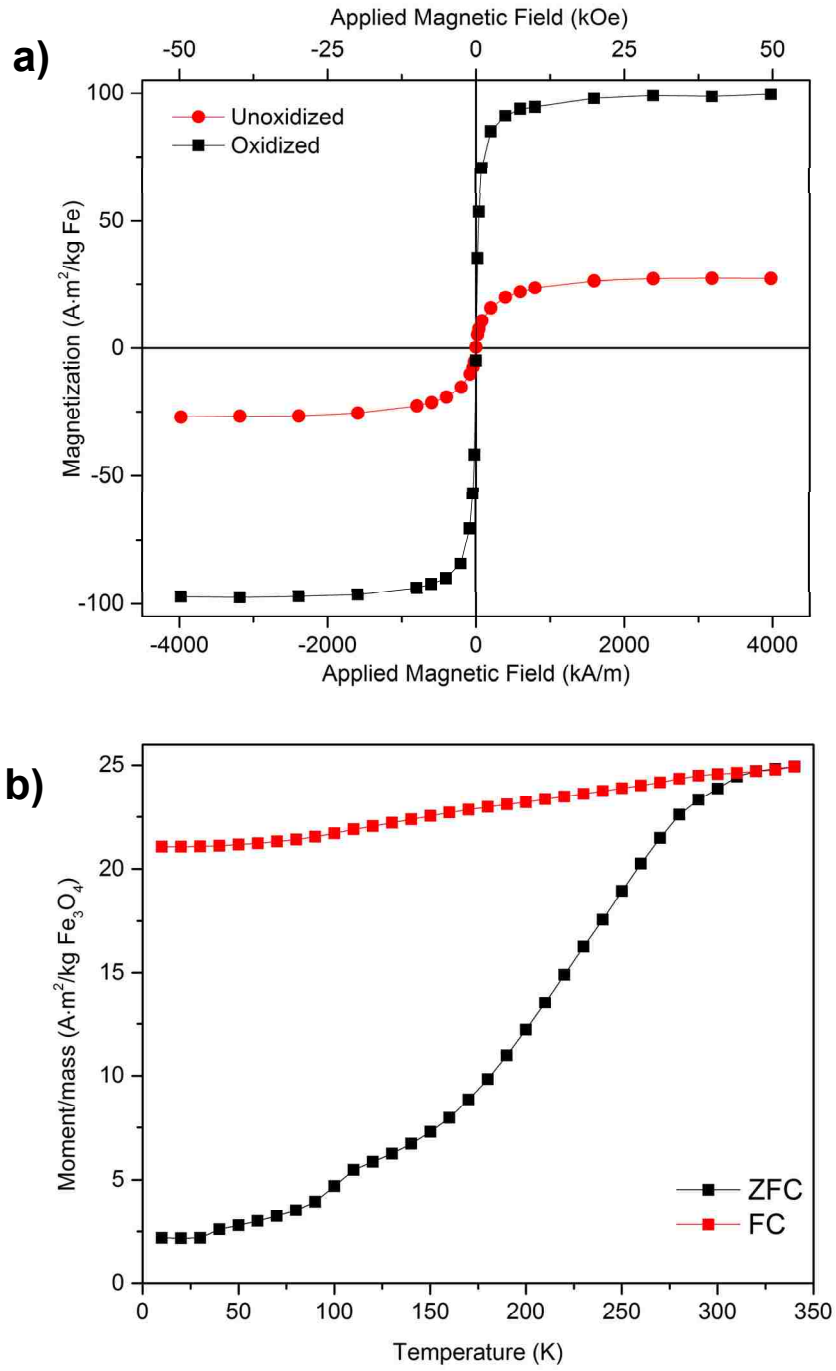

Figure 5-10. a) Magnetization curves of unoxidized and oxidized particles at 293K. The near quadrupling of the σ_{sat} reflects conversion of the $Fe_{1-x}O$ particles to Fe_3O_4 following oxidation. b) ZFC/FC magnetization curves for particles with an applied field of 10 Oe.

5.4 Conclusions

We have conclusively demonstrated that iron (III) acetylacetonate can be used as a precursor for the in situ generation of an iron oleate intermediate, and that this intermediate can be thermally decomposed in a one-pot reaction to generate high quality iron oxide nanoparticles. The reaction directly forms wüstite nanoparticles, which readily forms a magnetite shell when exposed to air at room temperature. The wüstite particles can be fully converted to magnetite through moderate heating in air. The magnetite nanoparticles formed in this fashion are highly magnetic, with saturation magnetizations of greater than 78% of bulk.

The particles synthesized using this reaction are essentially identical to those formed directly from an iron oleate precursor. The advantage is that this reaction contains only commercially available materials, used as received. No prior synthesis or purification of precursors is required, eliminating the irreproducibility introduced by the non-stoichiometric iron oleate precursor. Removing the variation in iron content of the precursor should dramatically improve batch to batch reproducibility and will be explored in the proceeding chapters.

Chapter 6 – A Mechanism for Growth of Iron Oxide Nanoparticles with Narrow Shape and Size Dispersity

6.1 Introduction

As discussed in chapter 1, controlling the size and morphology of magnetite nanoparticles is critical for their use in a number of biomedical applications. Rational design of a synthetic method that yields particles with low shape and size dispersity requires knowledge of the nucleation and growth mechanism for a given system. As a particle grows in solution, its structure changes continuously, reflecting the most kinetically preferred morphology until the thermodynamically stable phase is reached[127, 128]. By altering the ligand used in the system or tuning reaction parameters such as temperature, duration, or precursor concentration, the desired particle morphology can be achieved. Here, we demonstrate a method that produces spherical particles with low size dispersity, following transformation from kinetically preferred, irregular morphologies.

A kinetic model for the "heating-up" method was first developed by Hyeon et al. for the synthesis of small (< 10nm) nanoparticles from the decomposition of a custom synthesized iron(III) oleate precursor in octadecene[45]. The report demonstrated the utility of the LaMer mechanism in this system: burst nucleation followed by growth of uniformly sized spherical nanoparticles, and then size broadening as Ostwald ripening rapidly led to the formation of larger, cubic-shaped particles. Hyeon's experimental findings also illustrate the evolution of particle shapes for different growth processes. As particle size increased from the diffusion of

available monomer species in solution, the particles maintained a spherical shape. As the monomer species was depleted, Ostwald ripening resulted in the formation of increasingly more faceted particles with high size dispersity. Because spherical particles are required for the applications presented previously, identifying a reaction mechanism in our system that favors this morphology is highly desirable.

In Chapter 5, the thermal decomposition of $Fe(acac)_3$ in oleic acid was demonstrated to produce 27 nm particles that were approximately spherical in shape. However, the synthesized particles possessed an unacceptably high size dispersity of 12.1%. Employing the same reaction scheme, we show that increasing the reaction temperature to 350°C, just below the boiling point of oleic acid (360°C), drives the rapid formation of uniformly sized spherical particles. In addition, by developing a mechanism for growth of the nanoparticles, we are able to optimize the reaction duration to prevent unwanted ripening processes from occurring. We believe that these findings are of general utility for further understanding the growth of nanoparticles using this system.

6.2 Experimental

6.2.1 Iron oxide nanoparticle synthesis

For the reported study, a 100 mL three-necked round bottom flask was charged with 1.34 g (3.79 mmol) $Fe(acac)_3$ (99+%, Acros Organics, Fair Lawn, New Jersey) and 20 mL (63.0 mmol) oleic acid (technical grade, 90%, Sigma-Aldrich, St. Louis, MO). Reaction flasks were equipped with a magnetic stir bar and a

thermocouple for monitoring the reaction temperature. Reactions were performed with vigorous stirring under a nitrogen atmosphere, and heated to 350°C using a heating mantle controlled by a J-KEM 210T PID temperature controller (J-KEM, St. Louis, MO). For SAXS/TEM analysis, 8 aliquots of approximately 500 µL each were withdrawn at selected time intervals following nucleation.

6.2.2 Structural and Morphological Characterization

6.2.2.1 SAXS

Concentrated solutions of samples suspended in hexanes were injected into glass capillary tubes with a 1.0 mm diameter (Charles Supper Company, Natick, MA). Samples were analyzed using a Rigaku SmartLab diffractometer system with the SmartLab Guidance system control software. Cu-K-alpha radiation (40 kV, 44 mA) was used in transmission geometry with a scintillation detector. Data analysis was performed using Rigaku NANO-Solver v. 3.5 software, assuming a spherical particle shape, and calculating a volume average diameter.

6.2.3.2 Transmission Electron Microscopy (TEM)

Samples were prepared by applying a drop of a dilute suspension of nanoparticles in hexanes onto a carbon-coated copper grid (SPI, Westchester, PA) and wicking excess liquid away with a Kimwipe. Bright field TEM studies were performed using a JEOL 1200EX TEM operating at 120 kV (JEOL USA, Inc., Peabody, MA). Images were collected on a Gatan (Gatan, Pleasonton, CA) slow scan CCD

camera. Size analysis of imaged particles was performed using ImageJ software[117].

6.3 Results and discussion

6.3.1 Nanoparticle formation and growth

Aliquots were withdrawn immediately upon nucleation, which was observed by the change in color of the reaction solution from brown to black, and at periodic intervals thereafter. The aliquots were subsequently characterized with SAXS and TEM. The SAXS data are summarized in Table 6-1 and plotted in Figure 6-1, with the RAW SAXS data in Figure 6-2. TEM image and data analysis follow in Figure 6-3, Figure 6-4, and Table 6-2.

Table 6-1. Summary of SAXS data for aliquots drawn over the course of the reaction.

Aliquot number	Time after particle formation (min.)	SAXS Diameter (nm)	Size Dispersity
A1	0	20.11	17.4%
A2	0.5	22.10	14.9%
A3	5	23.48	9.6%
A4	10	23.77	8.3%
A5	20	24.34	8.5%
A6	30	24.52	6.8%
A7	60	24.94	8.0%
A8	90	25.62	7.4%

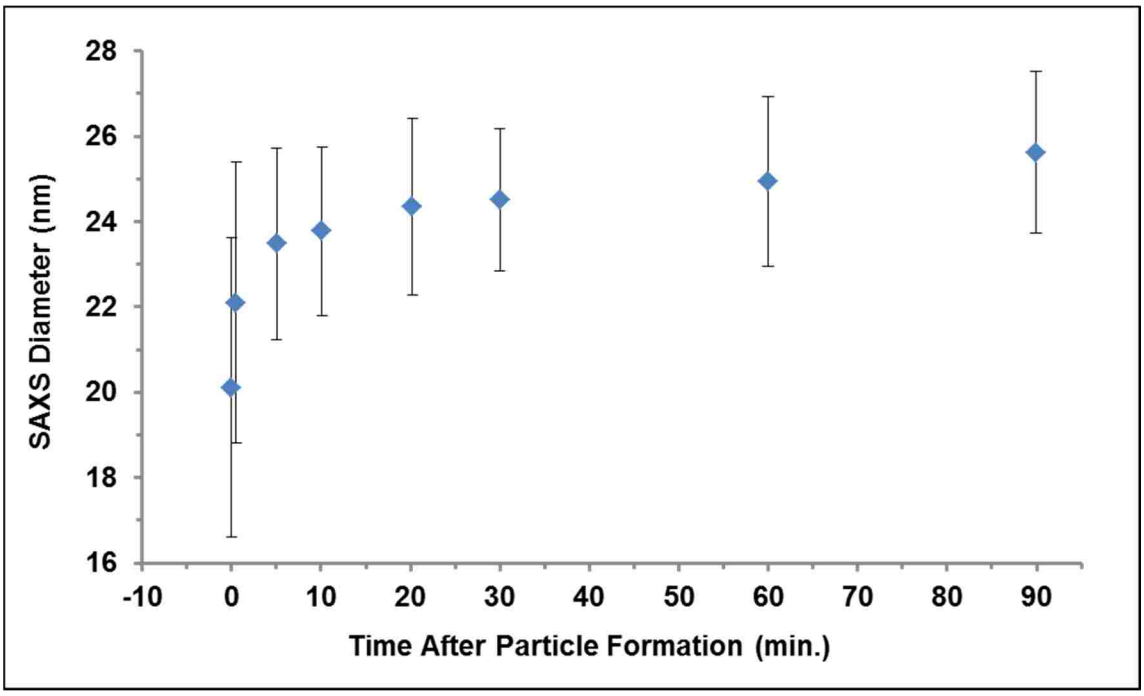

Figure 6-1. The growth of nanoparticles as measured using SAXS. Particle growth and size focusing are rapid in the first five minutes of the reaction and then slow over the remainder of the reaction.

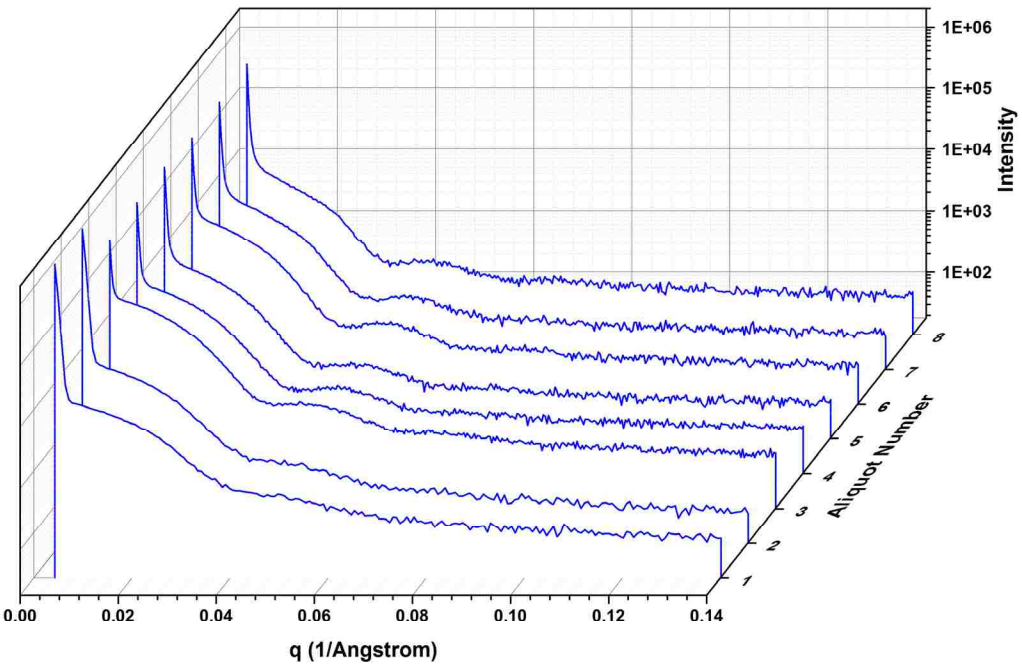

Figure 6-2. Raw SAXS data of the successive reaction aliquots.

Inspection of the SAXS data shows that the particle growth can be divided into two regions: rapid growth occurring in the first 5 minutes after nucleation, and a slower growth region from 5 – 90 minutes after nucleation. The SAXS data show that particles in the first aliquot are relatively large, with a diameter of 20.11 nm and high size dispersity of 17.4%. Within the following 30 seconds, the particle diameter increased significantly by 10%, with a 2.5% decrease in size dispersity. At the five minute time point, particle size increased by an additional 5.9% to 23.48 nm and size dispersity decreased to 9.6%. After this time point, particle growth slows until particles reach a maximum size of approximately 25 nm.

The rapid size focusing in the first few minutes of the reaction results from the high concentration of monomer species in the solution. The Gibbs-Thomson effect, which describes the relationship between the chemical potential of a particle and its radius, drives the growth of the particles to reduce the surface free energy of the system. The irregularly shaped particles observed in the early stages of the reaction gradually transform into an increasingly spherical shape, which represents a stable, minimal surface energy morphology. This is evidenced by the sustained narrowing of size dispersity measured by SAXS, with a minimum at 30 minutes following particle formation. Though SAXS measurements show that the size dispersity increased slightly as the reaction progressed further, the dispersity of the particles measured at the end of the reaction remained quite narrow at 7.4%.

The SAXS data fits are performed assuming a spherical particle shape, so TEM analysis provides a more realistic physical picture of the changing particle

morphology as the reaction progresses. TEM images of the sample aliquots are shown in Figure 6-3. The circularity of the particles was extracted from images analysis data using the formula $4\pi(\text{area}/\text{perimeter}^2)$, where a circularity of 1.0 describes a perfect circle. Assuming a Gaussian distribution of circularity values, the average values and standard deviations for each sample are provided in Table 6-2 and plotted in Figure 6.4. The trend toward increasing particle circularity is visible in Figure 6-3, with what appear to be perfectly circular particles in images taken of the last three aliquots.

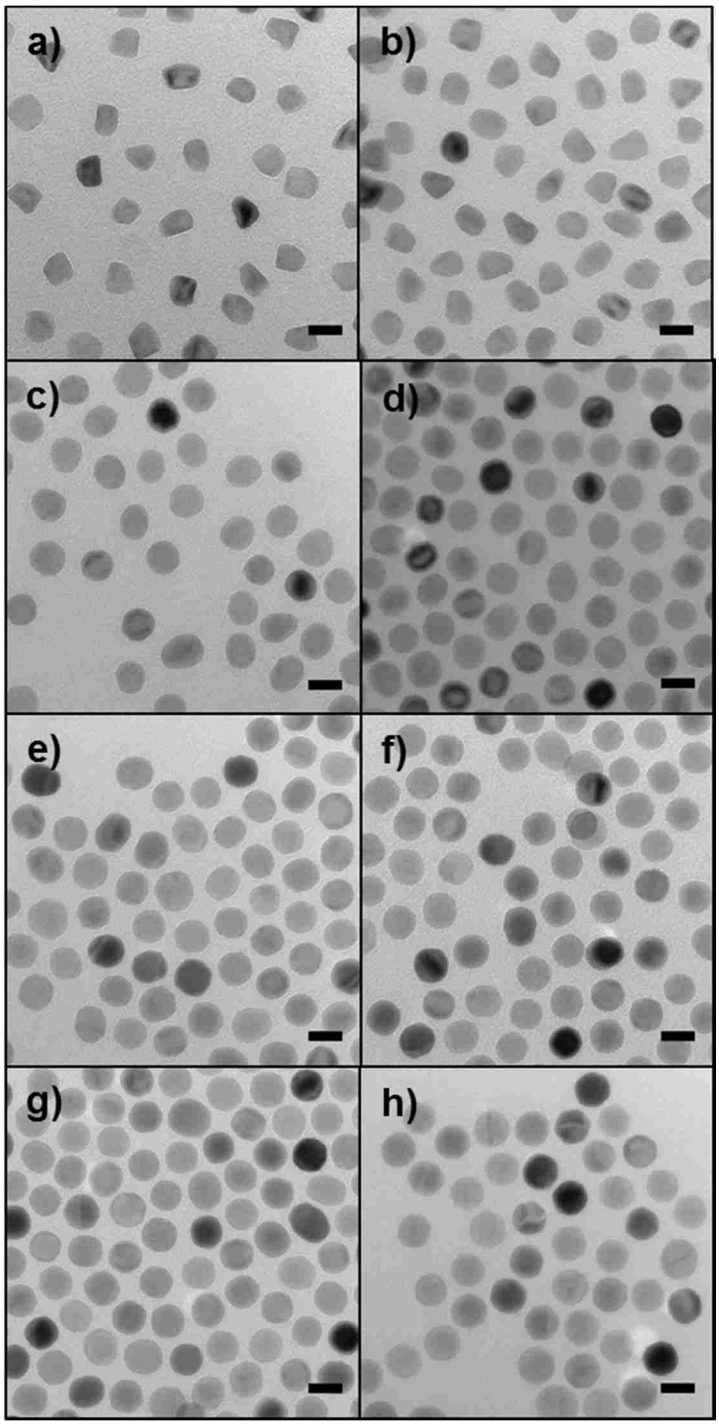

Figure 6-3. TEM images for aliquots taken during particle formation and subsequent growth: a) t = 0 min., b) t = 0.5 min., c) t = 5 min., d) t = 10 min., e) t = 20 min., f) t = 30 min., g) t = 60 min., and h) t = 90 min. Scale bars represent 20 nm.

Table 6-2. Summary of circularity data for aliquots drawn over the course of the reaction.

Aliquot number	Reaction Time (min.)	Average Circularity	Shape Dispersity	N
A1	0	0.784	7.9%	244
A2	0.5	0.813	6.5%	293
A3	5	0.849	4.6%	313
A4	10	0.863	3.2%	291
A5	20	0.871	2.6%	294
A6	30	0.875	2.6%	297
A7	60	0.877	2.9%	311
A8	90	0.877	2.6%	312

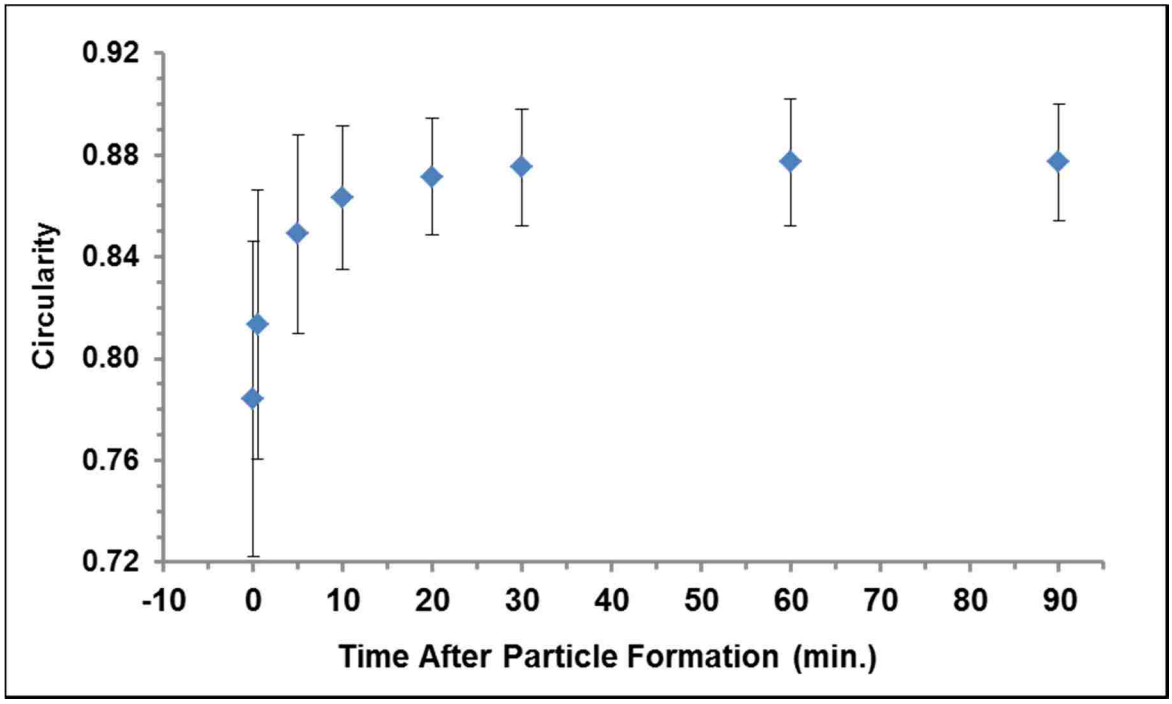

Figure 6-4. The evolution of particle circularity with reaction time. The particle shape changes most rapidly in the first five minutes of the reaction, with additional shape change slowing as the reaction progresses, with a similar trend occurring for the shape dispersity.

Analysis of the TEM images in Figure 6-3 shows that the particles formed in the first 30 seconds of the reaction have an irregular polyhedral shape with high size dispersity. The circularity of the particles increases rapidly, from 0.784 at the first time point, to 0.849 five minutes later. There is a sharp decrease in the shape dispersity during this time as well, from 7.9% to 4.6%. In agreement with the SAXS data, this trend slows as the reaction proceeds, with additional narrowing of shape dispersity stabilizing at 2.6%. Tp109he circularity calculations, however, are not close to the expected value of 1.0, but have values close to 0.87. This can be explained by considering the image analysis procedure. Slight roughness can develop around the particle edge when the grayscale image is converted to an 8-bit black and white image through the thresholding algorithm. This would naturally increase the perimeter of the particles, and the error would be exaggerated by the perimeter^2 term in the denominator of the calculation.

To further support that the particles are nearly perfectly spherical by the end of the reaction, the aspect ratio of the measured particles was also acquired from the image analysis data. Aspect ratio is the length of the major axis divided by the length of the minor axis, so a perfect circle would have an aspect ratio of 1. The measured aspect ratio of the imaged particles is shown in Table 6-3, plotted in Figure 6-5, and shows the same trend of increasing circularity and decreasing shape dispersity as the reaction progresses. Initially, the aspect ratio of the particles is 1.23 with a large dispersity of 14.1%. This value decreases rapidly in the first five minutes of the reaction, and by the 30 minute time point, the average aspect ratio decreased to a nearly perfectly circular value of 1.06. By the final time

point, the aspect ratio reached a minimum value of 1.05 with a shape dispersity of 3.5%.

Table 6-3. Summary of measured aspect ratio for aliquots drawn over the course of the reaction.

Aliquot number	Reaction Time (min.)	Aspect Ratio	Shape Dispersity	N
A1	0	1.23	14.1%	244
A2	0.5	1.23	14.1%	293
A3	5	1.14	7.9%	313
A4	10	1.10	6.4%	291
A5	20	1.09	5.5%	294
A6	30	1.06	4.7%	297
A7	60	1.06	4.7%	311
A8	90	1.05	3.5%	312

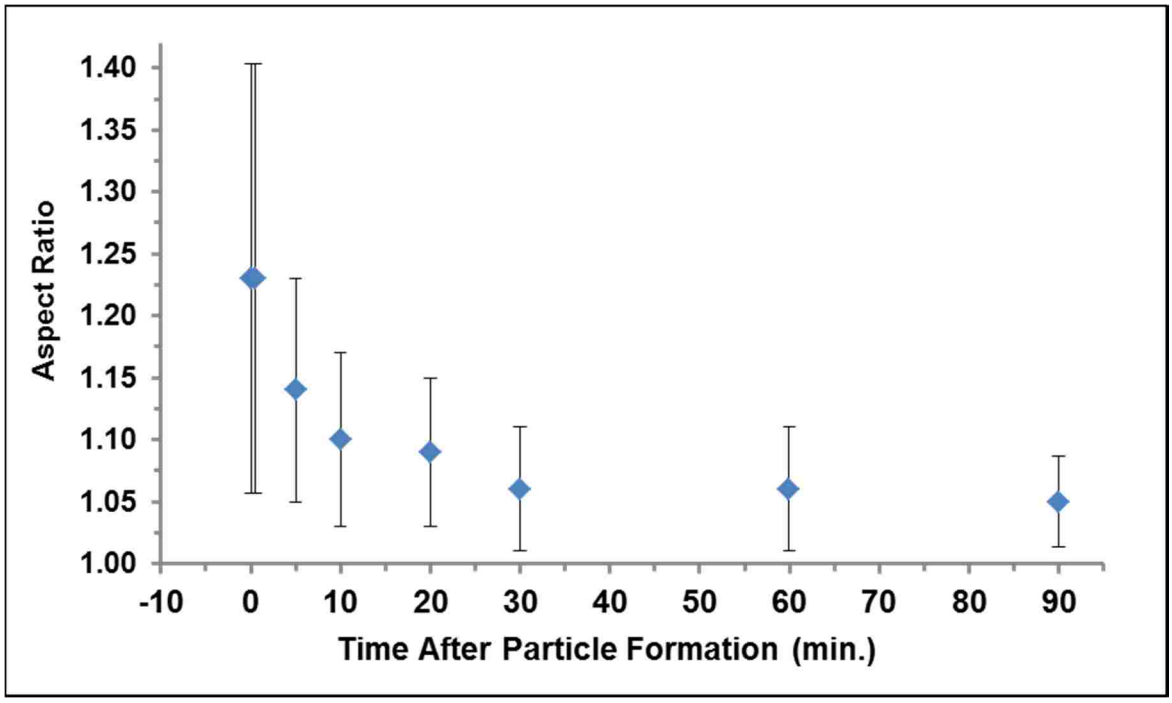

Figure 6-5. The change in the aspect ratio of the particles as the reaction progresses. At the end of the reaction, the particles have and average aspect ratio of 1.05, nearly perfectly circular.

The TEM images illustrate the evolution of particle morphology following nucleation. The first particles observed to form in this reaction are highly anisotropic, and exist for a brief period as a lower surface energy, spherical morphology is assumed. 30 minutes after nucleation, this process is complete.

6.3.2 Temperature profile

The temperature profile of the reaction is given in Figure 6-6, with time points for aliquot withdrawals following indicated with black markers. A final aliquot not shown in the temperature range plotted, was withdrawn when the reaction cooled to 120°C. The oscillations of the temperature of ±10°C about the 350°C set point are characteristic of the commercial PID temperature controller used.

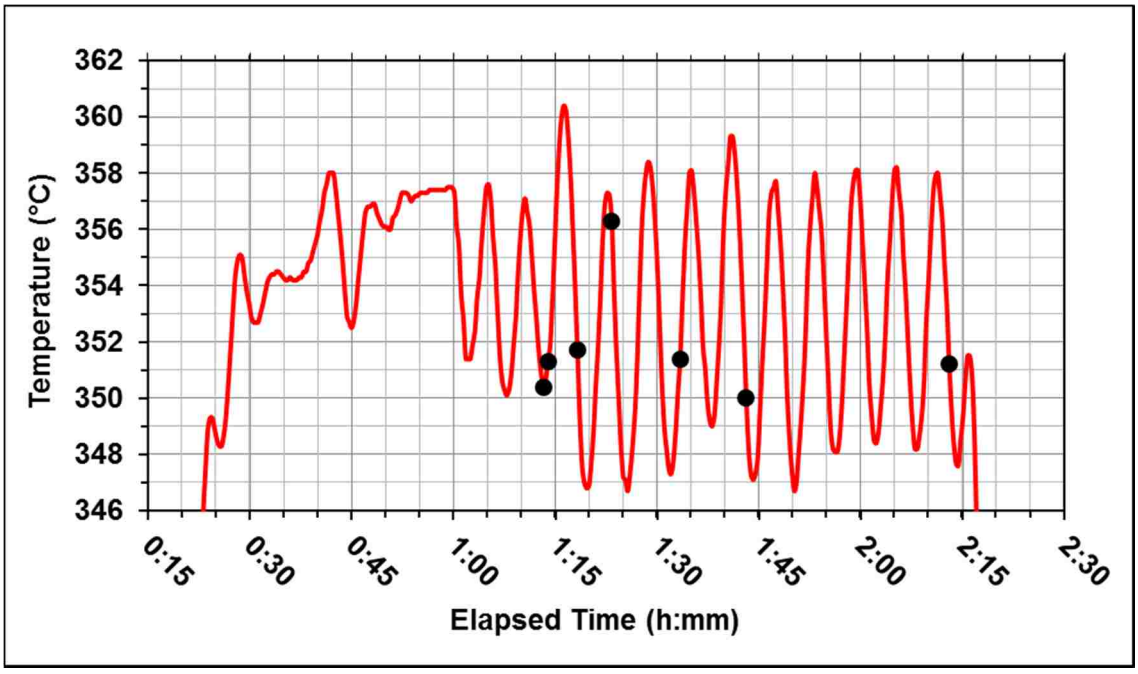

Figure 6-6. The temperature profile for the reported experiment. Time points for aliquot withdrawals following particle nucleation are indicated by black circles. A final aliquot (A*) was withdrawn when the reaction had cooled to 120°C.

6.4 Conclusions

The iron oxide nanoparticle growth study illustrated the process by which spherical particles with nearly uniform size dispersity are formed at high temperatures using the "heating-up" method. Knowledge of the growth mechanism is critical, particularly when determining the reaction parameters required for minimizing shape and size dispersity. With this approach, we have shown that a kinetically preferred morphology present in the early stages of the reaction is replaced by a spherical morphology with nearly uniform shape and size dispersity.

Chapter 7 – Exquisite Control of Particle Size Using the "Extended" LaMer Mechanism

7.1 Introduction

The properties of magnetic nanoparticles vary dramatically with size, and precise, reproducible control of size is critical if their full potential is to be realized in clinical applications. Typical approaches to achieving reproducible control of nanoparticle size have focused on the ligand used to stabilize the particles[129], or parameters reported to be influential for nucleation, such as the temperature ramp rate[44, 84]. Temperature ramp rate is a difficult parameter to maintain reproducibly between reactions, while modifying the ligand concentration in a series of closed reactions results in discrete nanoparticle sizes that do not reflect true size control over a range of particle diameters. Here, we present an approach for synthesis of nanoparticles using an open system. Precursor species are supplied to the reaction solution in a constant and quantifiable manner, providing precise control of particle sizes over a broad range. The growth of particles can then be extended for an arbitrarily long time, allowing particle size to be tuned by reaction duration. This synthetic approach reproducibly yields spherical particles with nearly uniform size dispersity.

The basic approach, which we refer to hereafter as the "Extended" LaMer mechanism, is to use a continuous addition of precursor to maintain a steady state concentration of the monomer species in solution while maintaining all other parameters constant. The result is a slow, steady growth of particles with a

predictable growth trajectory that can be altered by changing details such as addition rate and ligand concentration. Previously, homogeneous nucleation and growth of nanoparticles in an open system has been demonstrated in the double-jet precipitation of colloidal silver halides in aqueous solutions[130, 131]. However, no corresponding method has been developed for high temperature, thermolytic nanoparticle synthesis.

With respect to iron oxide nanoparticle synthesis, continuous addition of a stoichiometric iron precursor species has been limited by the properties of the compounds themselves. As we have discussed in previous chapters, conventionally prepared iron(III) oleate cannot be reliably synthesized in a reproducible way. $Fe(acac)_3$, on the other hand, while crystalline, has limited solubility in organic solvents that would lend to its slow, controlled addition to a reaction. However, we showed in Chapter 5 that iron(III) oleate can be prepared in situ from the decomposition of $Fe(acac)_3$ in oleic acid. In situ preparation of iron(III) oleate provides a means by which an iron precursor with a known quantity of iron can be prepared. Additionally, the iron(III) oleate prepared in this way requires no further manipulation such as washing that can lead to uncertainty regarding the final iron content.

By continuous addition of iron(III) oleate to a heated solvent solution, we demonstrate reproducible control of a kinetic growth mechanism that dictates spherical crystal morphology over a range of particle diameters with low size

dispersity. Further, we demonstrate the reaction parameters necessary for achieving isotropic growth of particles with time.

We believe that this approach will have general utility for a range of nanoparticle syntheses, and that the growth mechanism we identify for particles in this system will improve the overall understanding of the kinetic pathways of nanoparticle growth in a supersaturated solution.

7.2 Experimental

7.2.1 Iron(III) oleate synthesis

For these experiments, iron(III) oleate compounds were prepared in situ using methods similar to those presented previously. Briefly, three iron(III) oleate precursors were prepared using varying concentrations of $Fe(acac)_3$ in oleic acid. In a typical preparation, 15 mL (47.3 mmol) of oleic acid (technical grade, 90%, Sigma-Aldrich, St. Louis, MO), was combined with 14.16 mmol (0.94M), 9.34 mmol (0.62M), or 4.73 mmol (0.32M) $Fe(acac)_3$ (99+%, Acros Organics, Fair Lawn, New Jersey). The reagents were combined in a 100mL round bottom flask and submerged in a custom molten metal bath using Bolton 174*, a low melting point metal alloy (Bolton Metal Products, Bellefonte, PA). The reaction was stirred vigorously using a compact overhead stirrer (Caframo, Ontario, CA) under a nitrogen atmosphere. The reaction was heated to a set point of 320°C for the length of time necessary to form the iron(III) oleate complex. At the end of the

heating period, the reaction was removed from the metal bath and cooled to room temperature. Iron(III) oleate formation was confirmed using FTIR spectroscopy.

7.2.2 Characterization of iron(III) oleate

7.2.2.1 Fourier Transform Infrared (FTIR) Spectroscopy

Infrared spectra of synthesized precursors were collected on a Bruker IFS 66vS infrared spectrometer (Bruker Optik GmbH, Germany). Aliquots were characterized using a grazing angle attenuated total reflectance (GATR) accessory with a fixed 65° incidence angle and a hemispherical germanium crystal (Harrick Scientific Products Inc., Pleasantville, NY). 256 scans of each sample were collected at 2 cm^{-1} resolution from 3400 cm^{-1} to 700cm^{-1} using a liquid nitrogen cooled MCT detector. Extended ATR correction was performed on the collected spectra using Opus 6.5 software assuming an index of refraction of 1.5 for the aliquots. No additional baseline corrections were performed.

7.2.3 Iron oxide nanoparticle synthesis

To demonstrate nucleation and growth of iron oxide nanoparticles by continuous addition of iron(III) oleate precursor, and to understand the parameters that influenced particle growth rates, several types of experiments were performed. These experiments varied the concentration of the iron in the precursor solution, the addition rate of the iron precursor, and the amount of excess oleic acid in the solvent solution.

7.2.3.1 Growth of iron oxide nanoparticles by continuous addition of iron(III) oleate

To facilitate injection with a syringe, the synthesized iron(III) oleate precursors were diluted in 1-octadecene, a non-interacting, high boiling point solvent (Table 7-1). The diluted iron(III) oleate solutions were loaded into a Norm-Ject syringe, to which a 6" penetration needle was attached.

Table 7-1. Iron(III) oleate solutions were diluted with 1-octadecene to facilitate injection by a syringe.

[Iron(III) Oleate] as prepared (M)	**[Iron(III) Oleate] after dilution with octadecene (M)**
0.94	0.33
0.62	0.22
0.32	0.11

Typically, a reaction flask containing a 8.0 mmol docosane and 5.5mmol (1.1M) oleic acid was heated to 350°C in a molten metal bath with rapid stirring under a nitrogen atmosphere. For some experiments, no oleic acid was added to the reaction flask. When the reaction temperature stabilized at 350°C, the precursor was dripped into the solution at 3 mL/hr using a Chemyx syringe pump (Chemyx Inc., Stafford, TX). To explore the effect of drip rate on particle growth rate, the injection rate was varied by decreasing to 1.5 mL/hr or increasing to 6 mL/hr. The reaction was timed from the moment the first drop of precursor was injected into

the flask. Nucleation of particles was observed by an instantaneous change in the color of the reaction solution from dark brown to black. Aliquots were withdrawn from the reaction as close as possible to the nucleation event and at periodic intervals thereafter.

7.2.4 Characterization of iron oxide nanoparticles

7.2.4.1 SAXS

Concentrated solutions of samples suspended in hexanes were injected into glass capillary tubes with a 1.0 mm diameter (Charles Supper Company, Natick, MA). Samples were analyzed using a Rigaku SmartLab diffractometer system with the SmartLab Guidance system control software. Cu-K-alpha radiation (40 kV, 44 mA) was used in transmission geometry with a scintillation detector. Data analysis was performed using Rigaku NANO-Solver v. 3.5 software, assuming a spherical particle shape, and calculating a volume average diameter.

7.2.4.2 Transmission Electron Microscopy (TEM)

Samples were prepared by applying a drop of a dilute suspension of nanoparticles in hexanes onto a carbon-coated copper grid (SPI, Westchester, PA) and wicking excess liquid away with a Kimwipe. Bright field TEM studies were performed using a JEOL 1200EX TEM operating at 120 kV (JEOL USA, Inc., Peabody, MA). HRTEM images were acquired using a Tecnai G^2 F30 TEM using a 300 keV acceleration voltage (FEI, Hillsboro, OR). Size analysis of imaged particles was performed using ImageJ software[117].

7.2.4.3 Superconducting Quantum Interference Device (SQUID) Magnetometry

Magnetization measurements were collected using a Quantum Design MPMS-7 SQUID magnetometer. Samples were prepared by depositing a small amount of the synthesized nanoparticles suspended in hexanes onto the end of a Q-tip™ cotton swab and flame-sealing the sample in an NMR tube under vacuum. Magnetization curves were recorded from -50kOe to +50kOe (-4000 kA/m – +4000 kA/m) at 293K. Data were corrected for the slight paramagnetic signal contributed by the NMR tube at high fields. Zero-field cooled (ZFC) magnetization curves were obtained by cooling the sample to 5K with no applied field, then applying a field of 10 Oe (0.8 kA/m), and recording the magnetization from 5K to 345K. With the 10 Oe field still applied, the sample was then cooled from 345K to 5K to obtain the field-cooled (FC) magnetization. The precise iron mass of each sample was determined destructively by heating the Q-tip™ in a 600°C furnace for 1 hour to incinerate the organic material and then dissolving the iron containing residue in hydrochloric acid. A phenanthroline/Fe^{2+} complex was formed in solution and spectrophotometrically quantified using the concentration of a known dilution[118, 119].

7.3 Results and discussion

7.3.1 The "Extended" LaMer Mechanism

We describe the growth of nanoparticles by continuous addition of precursor species as the "Extended" LaMer mechanism (Figure 7-1). The underlying

principles of the LaMer mechanism (Figure 1-1) still apply to this method: in stage I, the monomer concentration increases in solution until a critical, supersaturation concentration is reached. In stage II, burst nucleation occurs and partially relieves the supersaturation condition, and in stage III, particle growth proceeds by diffusion of the monomer species to the particle surface. It is in this stage that a novel modification to the classical LaMer mechanism is introduced. The steady addition of monomer species in stage III facilitates the continuous growth of particles to an arbitrarily large size while maintaining low size and shape dispersity. In the classical LaMer mechanism, particle growth in this stage is initially subject to the availability of the monomer species. In a solution that has been depleted of monomer species, Ostwald ripening leads to the dissolution of small particles and the growth of larger particles. In nanoparticle synthesis, ripening is a process that is often associated with highly undesirable increases in size dispersity. However, by maintaining a sufficiently high concentration of monomer species in Stage III, ripening processes can be suppressed, resulting in a decrease, rather than an increase of the size distribution.

Focusing and broadening of the size distribution can both be explained by the Gibbs-Thomson relationship given in Equation (1-1) that describes the relationship between the chemical potential of a particle and its radius, i.e., smaller particles have a higher chemical potential than larger particles. When the concentration of the monomer species in solution is supersaturated, smaller particles grow faster than larger particles to reduce the surface free energy and size focusing occurs. In a limiting concentration of monomer, the high chemical potential of smaller

particles results in their dissolution in favor of the growth of larger particles and broadening of size dispersity results.

We demonstrate the application of the Extended LaMer mechanism to the current system with the following scheme: in stage I, iron(III) oleate is added at a constant rate to a heated solution of docosane and oleic acid. The thermal decomposition of iron (III) oleate results in the accrual of an oleic acid-stabilized iron monomer species. In stage II, a critical supersaturation concentration is reached, inducing nucleation of iron oxide nanoparticles and partially relieving the supersaturation of iron monomer species. In stage III, the continued addition of iron(III) oleate at a constant rate establishes a steady-state concentration of monomer species that allow growth of stable nuclei without an additional nucleation event. Particles can be grown to an arbitrarily large size, which can be tuned simply by changing the reaction duration. Here, we demonstrate that this approach yields steady, isotropic growth of spherical iron oxide nanoparticles with nearly uniform shape and size dispersity.

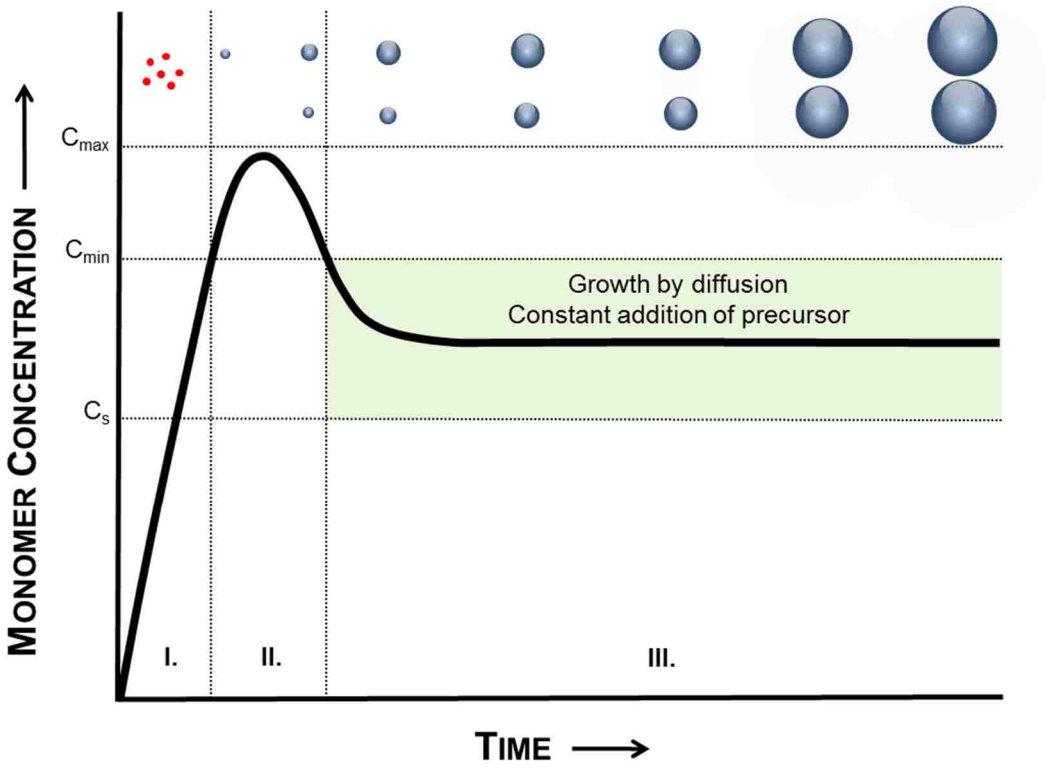

Figure 7-1. The proposed mechanism for the "Extended" LaMer Mechanism: stages I and II are identical to the original formalism devised by LaMer, but continuous addition of precursor in stage III allows steady growth of particles to an arbitrarily large size, while suppressing Ostwald ripening. The top panel shows the nucleation of particles in stage II, with an intrinsic size dispersity that is narrowed in the presence of a constant supply of precursor.

7.3.2 Characterization of iron(III) oleate

The formation of the iron(III) oleate precursor was verified by the presence of characteristic peaks in the FTIR spectrum. The decline of νC=O contributed by free oleic at 1710 cm^{-1} and the growth of strong peaks at 1613 and 1578 cm^{-1} from $\nu_{asym}COO^-$ and 1444 cm^{-1} from $\nu_{sym}COO^-$, confirm the formation of the iron(III) oleate species. Further, the intensities of the characteristic peaks provide a quantifiable measure by which reproducible synthesis of the precursor can be ensured between batches.

For the experiments presented here, three iron(III) oleate compounds with decreasing concentrations of $Fe(acac)_3$ were prepared: 0.94M, 0.62M, and 0.32M The FTIR spectra of these three iron oleate compounds is shown in Figure 7-2. The characteristic $\nu_{asym}COO^-$ and $\nu_{sym}COO^-$ peaks are strongest in the sample prepared with 0.94M $Fe(acac)_3$, and lowest in the sample prepared with 0.32M $Fe(acac)_3$, reflecting the amount of iron oleate present in the sample. As expected, the change in intensity of νC=O peak from free oleic acid is inversely proportional to the intensities of the νCOO^- peaks. The prepared iron(III) oleate compounds were subsequently used in the nanoparticle growth experiments presented in the following sections.

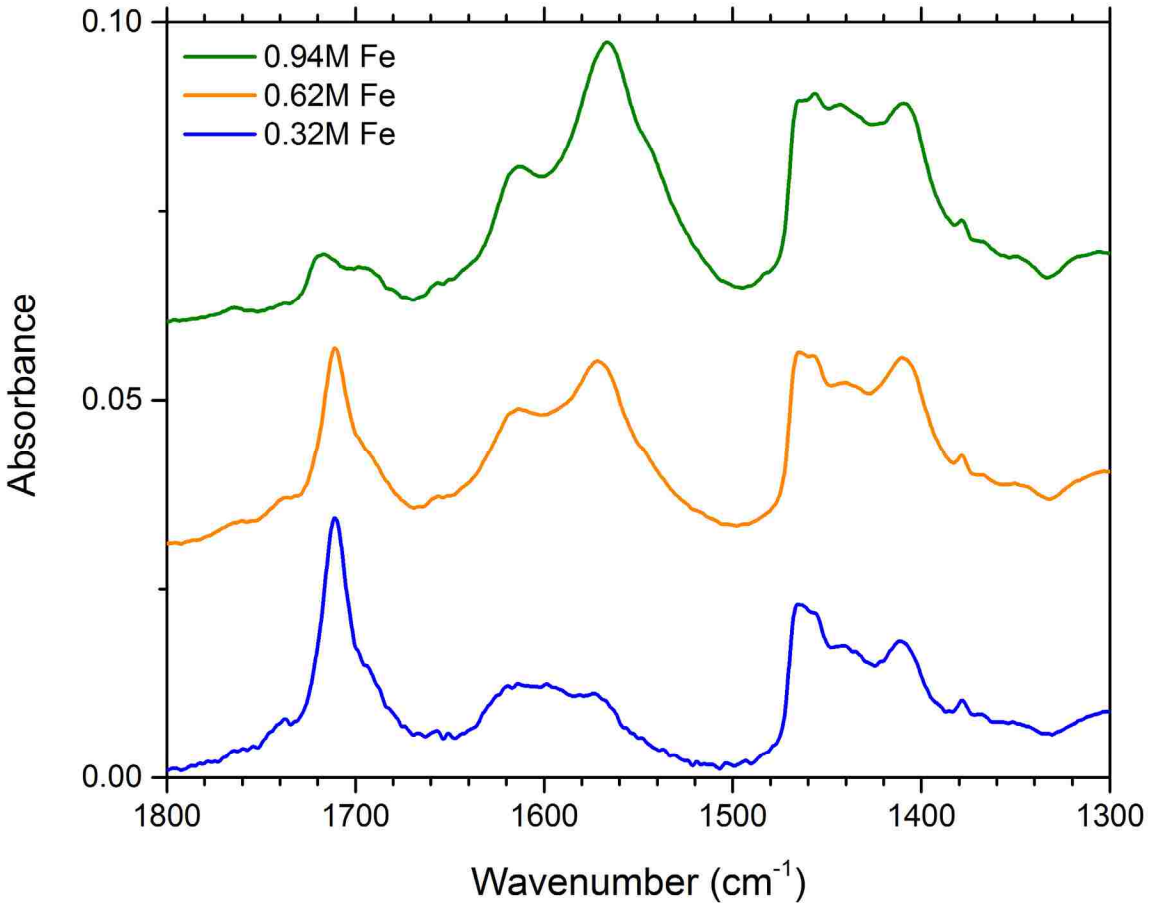

Figure 7-2. FTIR spectra of iron oleate precursor material prepared with 0.94M, 0.62M, and 0.32M $Fe(acac)_3$.

7.3.3 Nanoparticle growth with continuous addition of iron(III) oleate

For the nanoparticle synthesis, a 0.22M solution of iron(III) oleate was added to a heated solution containing 1.1M oleic acid in docosane at 3.0 mL/hr. The reaction time began when the first drop of iron fell into the solvent solution and ended when the addition was stopped five hours later. An aliquot was withdrawn when nucleation was observed and at periodic intervals thereafter. Nucleation can be visibly observed by a sudden change of the reaction solution from brown to black. SAXS data is summarized in Table 7-2 and plotted in Figure 7-3. TEM images of

selected aliquots are included in the plot of SAXS data to illustrate the particle size and morphology as the reaction progresses.

The particles sampled in the first aliquot are uniformly circular in shape, with a relatively low size dispersity of 11.8%. Approximately 15 minutes later, the particles have increased in size, and the size dispersity has decreased to 8.8%. Particle growth continues and size dispersity decreases until the 135 minute time point, when dispersity increases slightly. However, TEM analysis shows that the particles withdrawn at this time point have maintained a spherical shape. As the reaction progresses, the particles continue to grow, while the size dispersity as calculated by SAXS shows small increases. Figure 7-4 plots the change in size dispersity as a function of reaction time, illustrating the size focusing in the beginning of the reaction and the gradual trend toward increasing size dispersity at extended reaction times. However, after five hours, the size dispersity is still just 7.4%, with a standard deviation of 1.48 nm from the mean particle size of 20 nm. A high resolution TEM image of 20 nm nanoparticles shows uniformly circular particles with good crystallinity. Lattice planes extending to the surface of particles can be seen, indicating that the particles are single crystalline (Figure 7-4).

Table 7-2. Summary of SAXS data for aliquots drawn over the course of a reaction performed by continuous addition of 0.22M Fe(III) oleate at 3.0 mL/hr.

Aliquot number	Reaction Time (min.)	Fe Injected (mmol)	SAXS Diameter (nm)	Standard Dev. (nm)	Size Dispersity
A1	54.8	0.60	10.21	1.20	11.8%
A2	70.0	0.77	12.14	1.07	8.8%
A3	87.4	0.96	13.11	0.98	7.5%
A4	106.2	1.17	13.99	0.95	6.8%
A5	135.2	1.49	15.32	1.19	7.8%
A6	171.2	1.88	16.70	1.14	6.8%
A7	198.0	2.18	17.53	1.26	7.2%
A8	225.6	2.48	18.39	1.38	7.5%
A9	253.8	2.79	19.03	1.16	6.1%
A10	278.6	3.06	19.78	1.19	6.0%
A11	292.2	3.21	20.01	1.48	7.4%

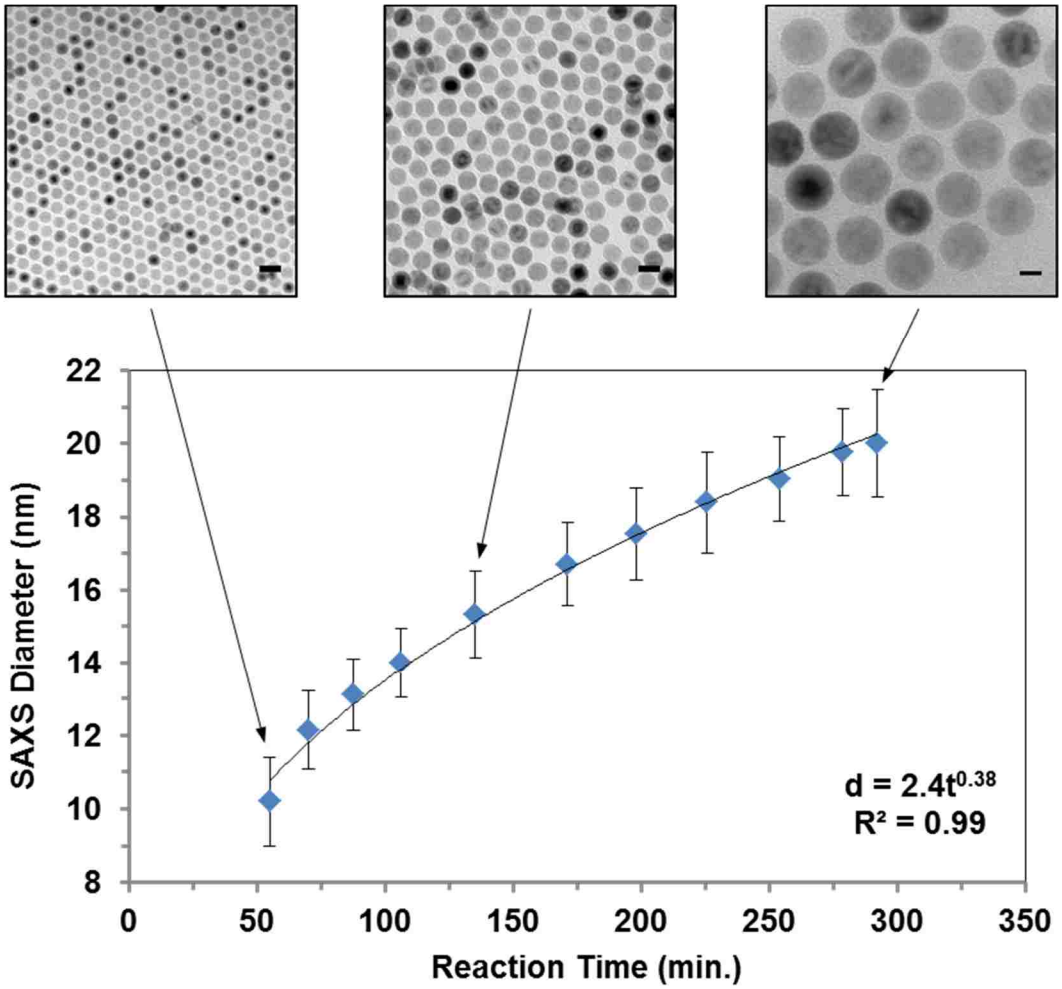

Figure 7-3. Growth curve of iron oxide nanoparticles as measured using SAXS. Isotropic growth of particles with low shape and size dispersity is observed for the duration of the reaction. Scale bars on TEM images represent 20 nm.

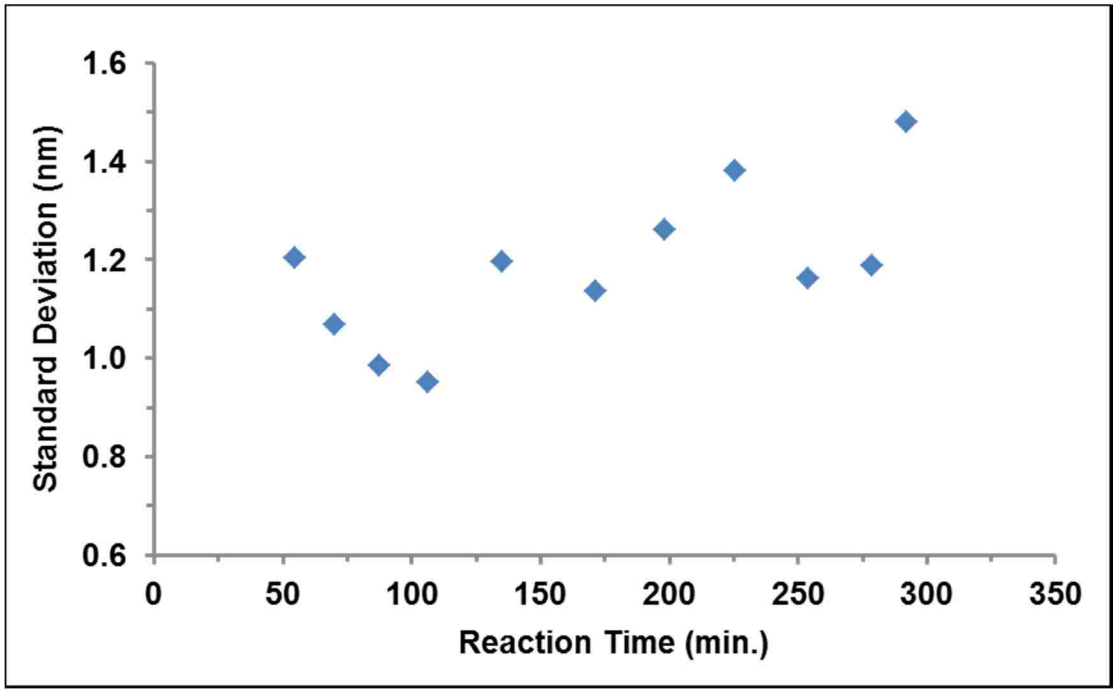

Figure 7-4. The change in standard deviation of particle size as a function of reaction time. Size focusing occurs early in the reaction, with a trend of increasing size dispersity as the reaction proceeds.

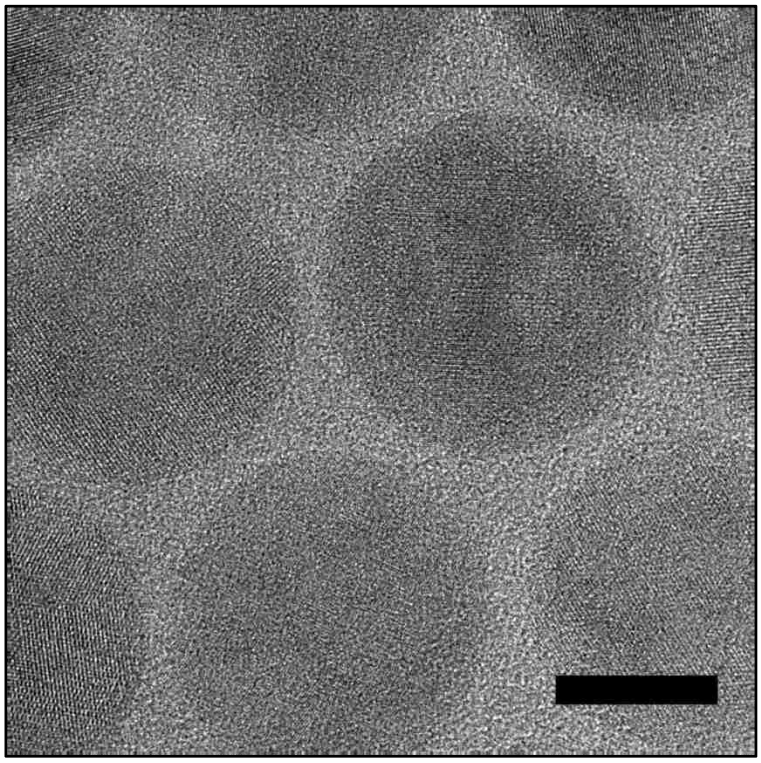

Figure 7-5. HRTEM image of 20 nm iron oxide nanoparticles. Lattice planes extend to the surface of the particle, indicating that particles are single-crystalline. The scale bar represents 20 nm.

Plotting the particle diameter as a function of reaction time allows for the growth rate to be fitted with a power law. We endeavor to identify the reaction parameters that will yield isotropic growth of spherical particles, thus a power law fit of diameter vs. reaction time should have a $t^{0.33}$ dependence. For the reaction plotted in Figure 7-3, the particle growth rate follows a $t^{0.38}$ dependence. If we consider the case of isotropic particle growth, particle volume increases linearly with time. Since $V \approx d^3$, it follows that d^3 will increase linearly with time, or that d will increase as $t^{1/3}$. As t is raised by an increasing exponential value, the growth rate of the particle actually decreases. Thus, a $t^{0.38}$ fit means that the particle volume is no longer growing linearly in time, but has decreased to $d^{2.6}$ growth with time.

Knowledge of the growth trajectory allows prediction of the maximum particle size attainable for a given reaction time, in turn providing size tenability of particle growth. Further, the power law dependence may provide insight to the mode of particle growth. Recall from Chapter 1, that $t^{0.33}$ dependence is characteristic of diffusion limited particle growth (Equation (1-16)), while a $t^{0.5}$ dependence reflects surface reaction limited growth ((1-19)). A value of the exponent between 0.33 and 0.5 suggests mixed diffusion and surface reaction control. Additional experiments in the following sections explore whether the $t^{0.33}$ dependence is intrinsic to the system or if it is subject to change as a function of reaction parameters such as iron concentration or addition rate.

7.3.4 Effect of iron concentration on nanoparticle growth

From the reaction plotted in Figure 7-3, the particle size obtained after a five hour reaction time is 20.01 nm. Following the $t^{.38}$ dependence of particle growth, a doubling of the reaction time to 10 hours would only result in the growth of particles by an additional 7 nm. It is apparent that for a given concentration of iron(III) oleate, there is a maximum particle size that can be achieved in a reasonable reaction timeframe. Increasing the iron concentration in the precursor solution is one approach by which the maximum particle size can be increased within a given timeframe.

For the experiments described in this section, a 0.22M solution of iron(III) oleate in octadecene was added to a heated solution containing 1.1M oleic acid in docosane at 3.0 mL/hr. The reaction time began when the first drop of iron fell into the solvent

solution. An aliquot was withdrawn when nucleation was observed and at periodic intervals thereafter. After approximately 2 hours, the 0.22M solution was exchanged for a 0.33M solution of iron(III) oleate in octadecene, with the same 3.0 mL addition rate. Particle growth was allowed to continue for an additional 2.5 hours, with aliquots withdrawn at periodic intervals. Aliquots were characterized using SAXS, the results of which are summarized in Table 7-3 and plotted in Figure 7-6.

The trajectory of particle growth in the first segment of the reaction using the 0.22M iron(III) oleate precursor is nearly identical to the reaction detailed in the previous section. Particles grow with a $t^{0.36}$ dependence, very close to the $t^{0.38}$ dependence observed previously. Rapid size focusing and sustained, nearly uniform size dispersity further demonstrate that the 0.22M iron(III) oleate precursor can be used for reproducible synthesis of particles for the reaction times tested here.

In the second segment of the reaction, following the increase of iron(III) oleate precursor concentration to 0.33M, the particles continue to grow with very narrow size dispersity. The increase in iron concentration appears to have induced a slight increase in the observed size dispersity from 5.7% at the end of the first segment to 7.4% in the second segment, but this increase was temporary, with additional size focusing resulting in a decrease of the size dispersity to 5.4% 15 minutes later. Though the size dispersity remains relatively low for the remainder of the reaction, it increases slightly as the reaction proceeds. The maximum standard deviation of 1.1 nm in the first segment of the reaction increases to a maximum of 1.6 nm in

the second segment of the reaction. In addition, there is another important difference in the growth rate of particles in the second segment with respect to the first. The $t^{0.36}$ dependence of particle diameter observed in the first segment decreases to a $t^{0.45}$ dependence in the second segment. The value of the exponent suggests that particle growth is surface reaction limited. This change in time dependence may simply reflect that there are not enough available sites at the particle surface to accommodate the additional monomer species in solution. This growth mode is generally not preferred in a limiting concentration of monomer species, since the Gibbs-Thomson effect results in a broadening of the size dispersity (Equation (1-25)). For the range of particle sizes shown here, this effect is not observed, most likely because the high supersaturation of monomer species in solution suppresses Ostwald ripening. Thus, increasing the precursor concentration appears to be a viable way to increase the maximum particle size for a given reaction time. In Figure 7-6, the calculated growth trajectory is plotted with dashed lines to indicate the maximum particle size that might be expected for a given reaction time. At 400 minutes, the 0.33M precursor solution would produce particles 14% large than would be attainable using the 0.22M solution.

Table 7-3. Summary of SAXS data for aliquots drawn over the course of a reaction performed by continuous addition of 0.22M Fe(III) oleate at 3.0 mL/hr followed by continuous addition of 0.33M Fe(III) oleate at 3.0 mL/hr.

Aliquot number	Reaction Time (min.)	Fe Injected (mmol)	SAXS Diameter (nm)	Standard Dev. (nm)	Size Dispersity
0.22M Fe(III) Oleate					
A1	23	0.41	11.42	1.04	9.1%
A2	43	0.64	13.71	1.12	8.2%
A3	63	0.85	15.06	1.14	7.6%
A4	90	1.13	16.78	1.11	6.6%
A5	103	1.29	17.51	1.05	6.0%
A6	114	1.41	18.07	1.14	6.3%
A7	127	1.54	18.67	1.06	5.7%
0.33M Fe(III) Oleate					
A8	143	1.68	19.16	1.42	7.4%
A9	158	1.93	20.04	1.08	5.4%
A10	180	2.29	21.47	1.18	5.5%
A11	197	2.56	22.14	1.45	6.5%
A12	217	2.89	23.11	1.64	7.1%
A13	233	3.15	23.77	1.43	6.0%
A14	254	3.51	24.68	1.60	6.5%
A15	275	3.85	25.42	1.53	6.0%

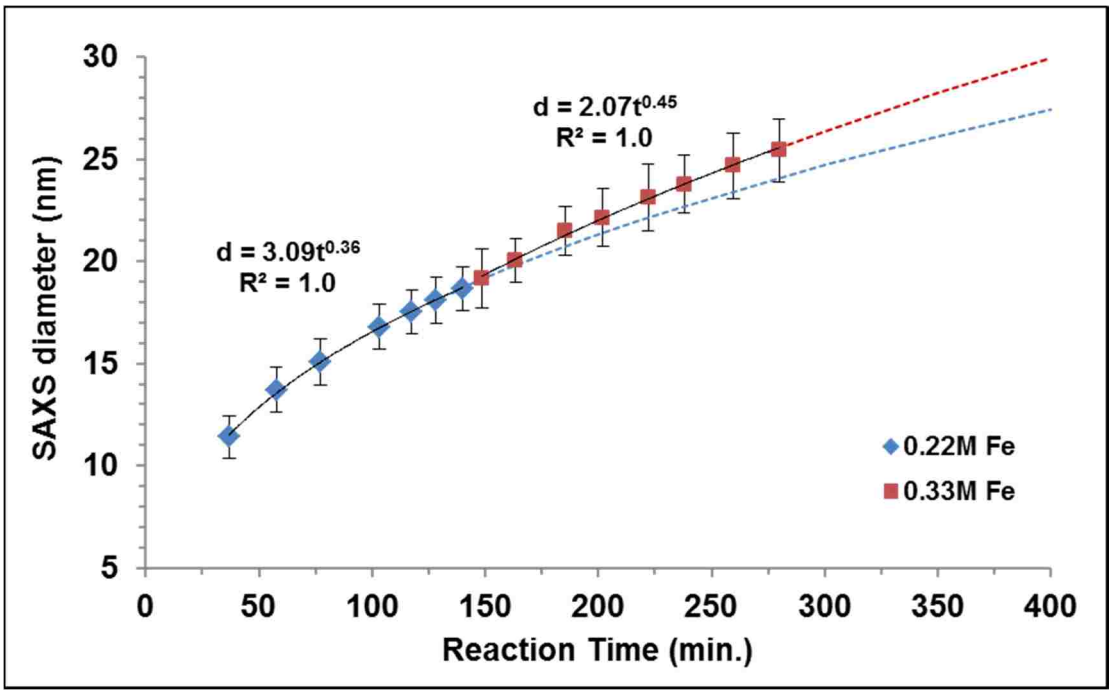

Figure 7-6. Growth curve of iron oxide nanoparticles as a 0.22M Fe solution is injected (blue) and then exchanged for a 0.33M Fe solution. Particle growth rate for the 0.22M Fe solution is slightly faster than that of the 0.33M Fe solution.

7.3.5 Nanoparticle growth with variable addition rate of iron(III) oleate

Rather than physically exchanging the iron precursor solution, which can be tedious and lead to irreproducibility in the synthesis, the effective iron concentration in solution can be more elegantly controlled by changing the injection rate. To test the effect of precursor addition rate on the corresponding growth rate of particles, a precursor solution containing 0.22M iron(III) oleate was added to the reaction flask in three separate reactions at 1.5 mL/hr, 3.0 mL/hr, and 6.0 mL/hr (Table 7-4 and Figure 7-7). The first aliquot was drawn as close as possible to observed nucleation.

The initial particle size is approximately equivalent for each addition rate, but the data show that an increased addition rate ultimately results in the formation of larger particles within a given time after nucleation. For example, in the1.5 mL/hr addition, 15 nm particles are observed 40 minutes after nucleation. In the 3.0 mL/hr reaction, 15 nm particles are observed 38 minutes after nucleation, and in the 6.0 mL/hr reaction, approximately 15 nm particles are observed 22 minutes after nucleation.

More can be revealed about the particular growth mode for each experiment by looking at the power law fit for the growth curves. The 3.0 mL/hr addition results in a growth curve with $t^{0.39}$ dependence, while the 1.5 mL addition results in a slightly slower growth trajectory, with a $t^{0.47}$ dependence. Both addition rates suggest a mix of diffusion limited and surface reaction limited particle growth, though the latter is far more pronounced for the 1.5 mL addition rate. In both cases, size focusing is observed, and the size dispersity in the range of sizes tested is very narrow. The 6.0 mL/hr addition rate still produces particles with narrow size dispersity, though the $t^{0.50}$ dependence of particle size indicates surface reaction limited growth.

To summarize this data, increasing the addition rate increases the growth rate of the particles, but the maximum growth rate achievable for a given set of conditions only occurs when there is a $t^{0.33}$ dependence, indicative of diffusion limited growth.

Table 7-4. Summary of SAXS data for three reactions in which the addition rate of 0.22M Fe(III) oleate is varied, from 1.5 mL/hr to 3.0 mL/hr to 6.0 mL/hr.

Aliquot number	Reaction Time (min.)	Fe Injected (mmol)	SAXS Diameter (nm)	Standard Dev. (nm)	Size Dispersity
1.5 mL/hr					
A1	23	0.10	11.42	1.04	9.1%
A2	43	0.11	13.71	1.12	8.2%
A3	63	0.16	15.06	1.14	7.6%
A4	90	0.22	16.78	1.11	6.6%
A5	103	0.31	17.51	1.05	6.0%
A6	127	0.40	18.67	1.06	5.7%
3.0 mL/hr					
A1	36	0.20	11.53	0.97	8.4%
A2	43	0.24	12.32	1.04	8.4%
A3	49	0.27	12.94	0.91	7.0%
A4	74	0.41	15.31	0.96	6.3%
A5	92	0.51	16.69	1.02	6.1%
6.0 mL/hr					
A1	28	0.31	10.04	1.12	11.2%
A2	36	0.40	12.92	0.89	6.9%
A3	50	0.55	14.69	1.09	7.4%
A4	77	0.85	17.45	1.08	6.2%
A5	84	0.92	18.08	1.23	6.8%

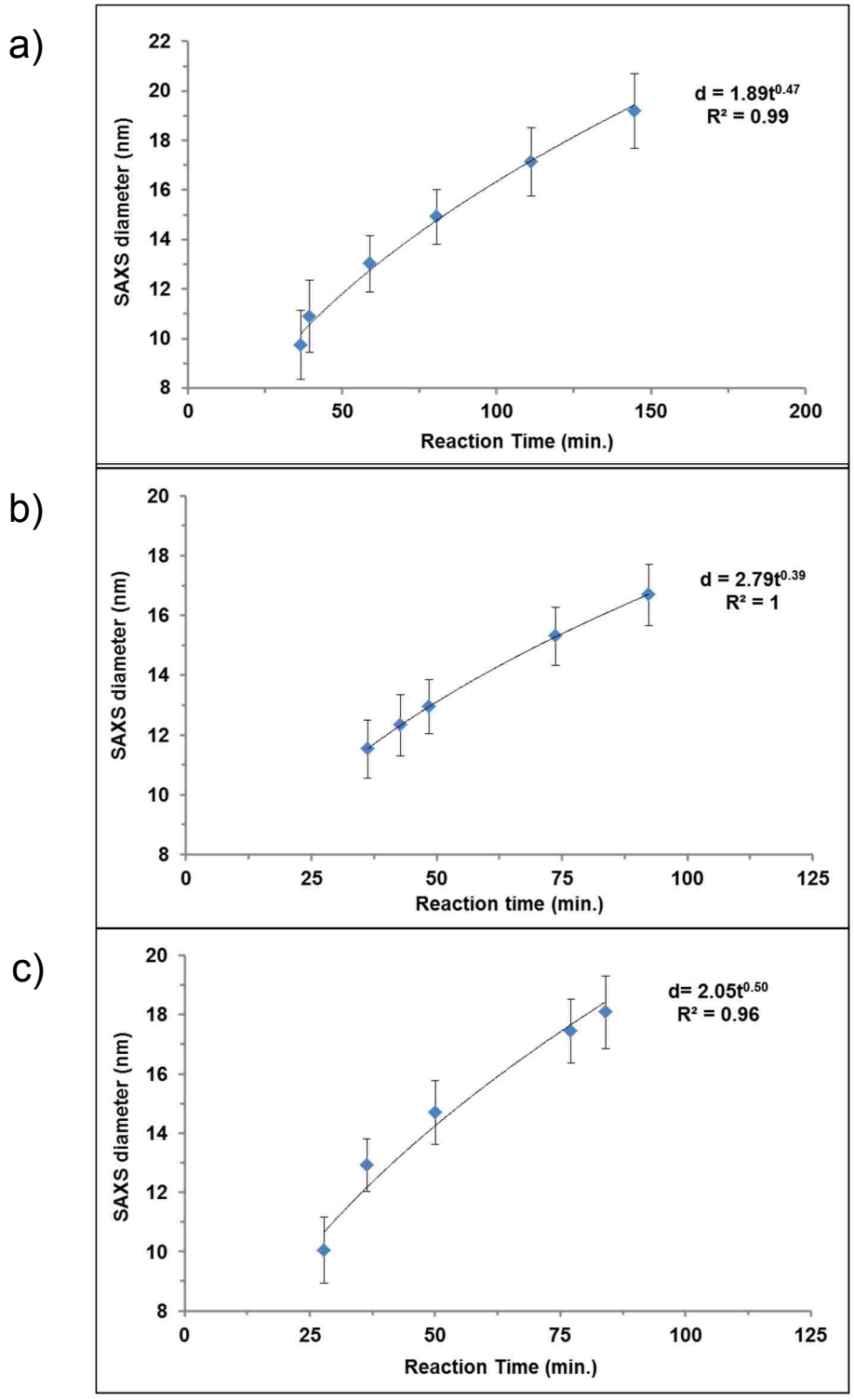

Figure 7-7. Particle growth curves using increasing precursor addition rates: a) 1.5 mL/hr, b) 3.0 mL/hr, c) 6.0 mL/hr. Particle growth is fastest at a 3.0 mL/hr addition rate and slowest at a 6.0 mL/hr addition rate.

7.3.6 Nanoparticle growth in the absence of excess oleic acid

We believe that the slow, isotropic growth of uniformly sized spherical particles in the previous experiments is due to the large excess of oleic acid. A 0.22M solution was injected into a heated reaction flask containing only 8.0 mmol docosane, the growth rate of particles dramatically increased, as shown in Table 7-5 and Figure 7-8.

Inset TEM images in Figure 7-8 show an interesting trend as the particles grow. The particles from the first aliquot are approximately spherical, with a diameter of 18 nm and a high size dispersity of 20.2%. Within 3 minutes, the particle size increases to 21.77 nm, accompanied by a substantial reduction of size dispersity to 8.2%. Rapid growth of particles continues, but as the TEM image of the aliquot drawn at 18 minutes shows, the particles have assumed a slightly more cubic shape. These particles reach nearly 50 nm in diameter after just 48 minutes, with a relatively uniform shape and size dispersity. However, when the final aliquot is withdrawn 22 minutes later, the particle size dispersity has increased quite substantially. It is evident Ostwald ripening is dominating particle growth at this step, in spite of the continuous addition of precursor. It is possible that the monomer concentration in solution was not high enough sufficient to sustain growth of particles, and that Ostwald ripening became the dominant mechanism of growth in this limit. The overall growth trajectory of this reaction had a $t^{0.49}$ dependence, suggesting surface reaction limited growth of the particles in this

system. This study shows the importance of excess of oleic acid in the slow, controlled growth of spherical nanoparticles.

Table 7-5. Summary of SAXS data for aliquots drawn over the course of a reaction performed by continuous addition of 0.22M Fe(III) oleate at 3.0 mL/hr into a solvent solution containing no oleic acid.

Aliquot number	Reaction Time (min.)	Fe Injected (mmol)	SAXS Diameter (nm)	Standard Dev. (nm)	Size Dispersity
A1	6	0.07	18.12	3.66	20.2%
A2	9	0.10	21.77	1.89	8.2%
A3	18	0.19	30.64	2.18	7.1%
A4	26	0.29	37.15	3.86	10.4%
A5	48	0.53	47.76	3.53	7.4%
A6	70	0.77	61.91	10.09	16.3%

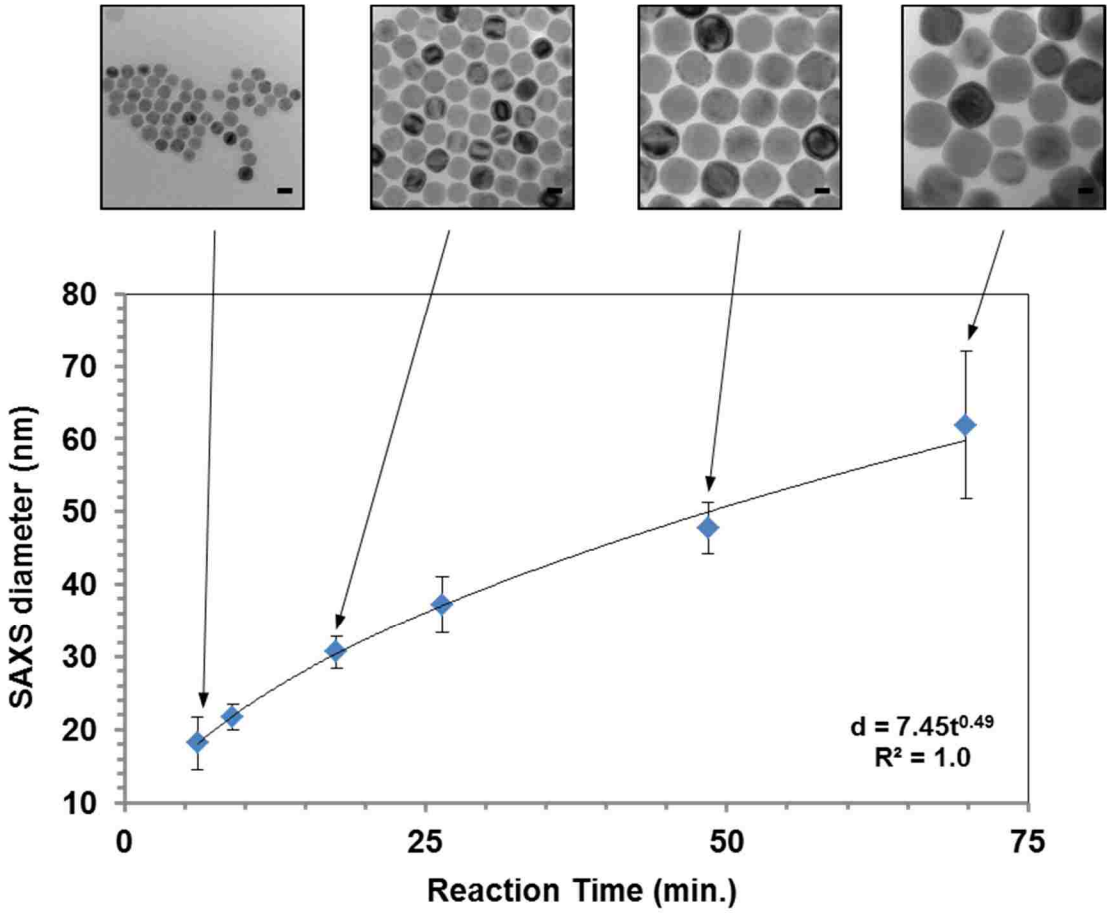

Figure 7-8. Particle growth when no oleic acid is present in the reaction flask. Growth is very rapid compared to reactions in which a large excess of oleic acid is present. Scale bars on TEM images represent 20 nm.

7.3.7 SQUID Magnetometry

SQUID magnetometry was performed on three samples from the reaction plotted in 9: aliquot 1 (10.2 nm), aliquot 5 (15.3 nm) and aliquot 11 (20.0 nm). The σ_{sat} of the synthesized particles at 293K is co-plotted with the T_B identified from ZFC/FC curves in Figure 7-9.

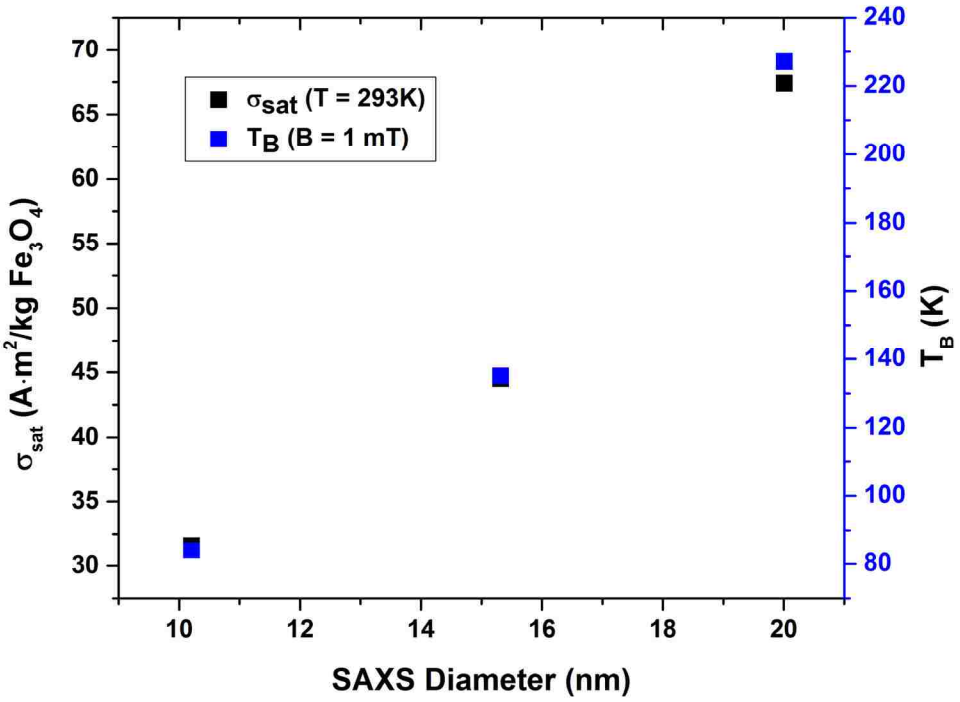

Figure 7-9. σ_{sat} and T_B for aliquot numbers 1 (10.21 nm), 5 (15.32 nm), and 11 (20.01 nm). Both properties increase with increasing particle diameter.

The measured σ_{sat} of the 10.21 nm particles is 31.6 A·m^2/kg Fe_3O_4, increases to 44.5 A·m^2/kg Fe_3O_4 for the 15.32 nm particles, and then 67.4 A·m^2/kg Fe_3O_4 for 20.01 nm particles, 73% of bulk Fe_3O_4 at 293K[63], and many times larger than the σ_{sat} reported for similarly sized particles by Park et al[44]. The trend observed here can be attributed to the increased surface area/volume ratio of small particles. Broken crystal symmetry at the particle surface[132] and spin disorder introduced by ligand binding[133, 134] have an increasingly deleterious effect on the saturation magnetization. The blocking temperature, also a size dependent effect (Equation

(1-29)), increases with increasing from 84K for 10.21 nm particles, to 135K for 15.32 nm particles, and 227K for 20.01 nm particles.

7.3.8 Temperature control

Stable temperature control was demonstrated for the reactions performed here using a custom molten metal bath with PID control using a custom National Instruments interface. The temperature profile of a typical reaction is shown in Figure 7-10. When the temperature of the reaction stabilized at the 350°C set point, injection of the iron precursor was initiated. After a period of time, nucleation of particles occurred, causing instantaneous heating of the reaction solution by ~2°C. The increase in temperature results in part from the decrease in the Gibbs free energy of the system following nucleation, but may result in part from the autocatalytic nature of the nucleation process. The temperature decrease following nucleation is the result of negative feedback from the temperature controller software, as it attempted to restore the reaction to the 350°C set point. Within several minutes, the reaction temperature stabilized to within 1°C of the set point for the remainder of the precursor addition. Once the precursor addition ended, the decreased thermal load caused increased oscillations of the reaction temperature from the set point. It was later discovered that tuning the maximum power settings at this point helped to dampen these oscillations. A significant improvement in temperature control is achieved using the custom molten metal bath with respect to the commercial instrument used previously that had oscillations of ±10°C (Figure 6-6).

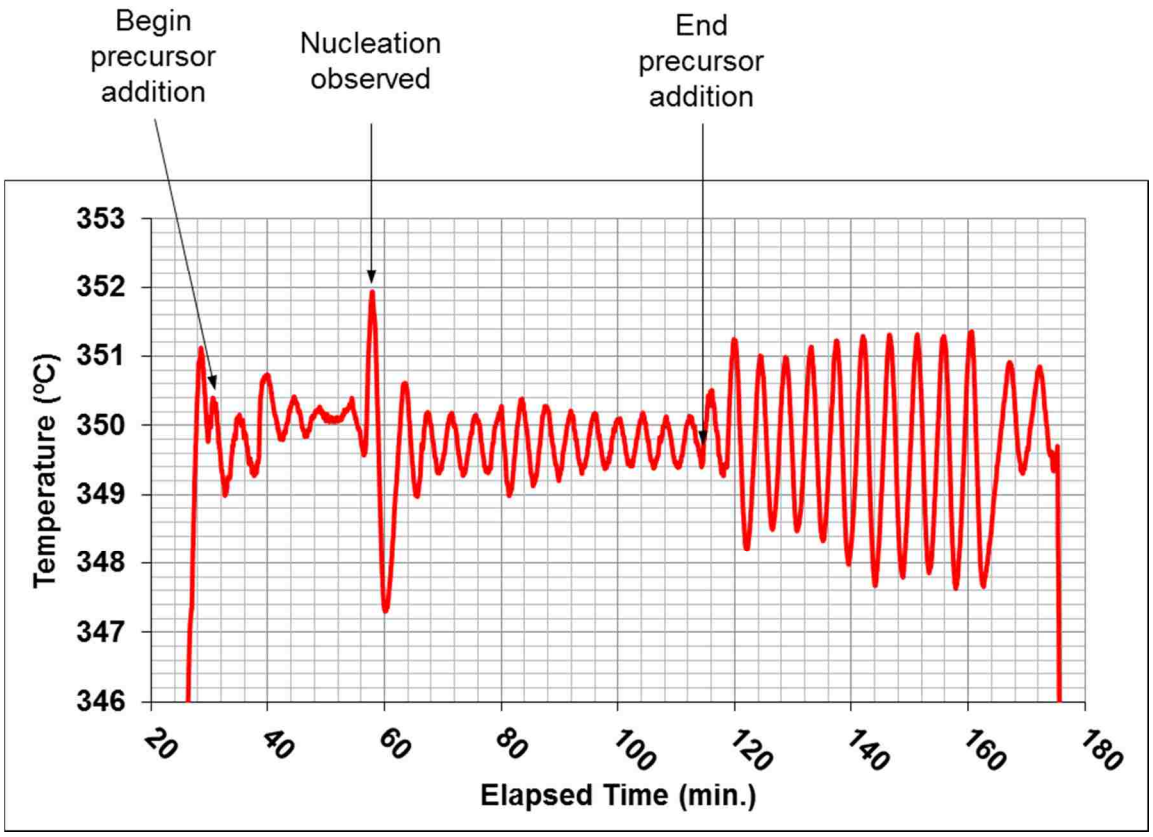

Figure 7-10. Temperature profile for a typical reaction with continuous addition of precursor. When the reaction temperature stabilized at the 350°C set point, precursor addition began. Upon nucleation of particles, a rapid increase of temperature was observed. During the addition of the precursor, temperature variations were ~1°C or less. Following the termination of precursor addition, temperature fluctuations increased to ~2°C.

7.4 Conclusions

We have demonstrated a robust approach to the synthesis of spherical iron oxide nanoparticles with narrow size dispersity using an iron(III) oleate precursor synthesized in situ. The novel preparation of the iron(III) oleate compound provides stoichiometric control over starting materials that cannot be achieved using conventional methods. Continuous addition of the precursor allows a broad

range of particles sizes to be reproducibly synthesized, with a demonstrated span of 10 – 25 nm for the system in which oleic acid was present in excess. The true upper limit of this system has yet to be determined empirically, but is expected to be far greater than 25 nm. Using a large excess of oleic acid in the reaction solution, 3.0 mL/hr addition of a 0.22M iron(III) oleate solution consistently resulted in the production of uniformly spherical particles with a standard deviation not greater than 1.1 nm of the mean particle size for all sizes measured. These parameters were determined to be optimal for isotropic, diffusion limited growth of particles with very low size dispersity.

Modifying the iron concentration in the growth solution directly or increasing the addition rate of the precursor was demonstrated to influence the maximum particle size accessible within a given timeframe. Particles with low size dispersity were produced in all cases, although deviation from the conditions outlined above changed the growth trajectory to one associated with surface reaction limited, rather than faster, diffusion limited, particle growth.

The importance of a large excess of oleic acid was demonstrated for ensuring slow growth of spherical nanoparticles. In the absence of a large excess, rapid growth of large, slightly cubic particles were synthesized. With a constant addition rate, growth of the particles remained stable to nearly 50 nm in diameter. Beyond this point, iron addition was not sufficient to suppress Ostwald ripening processes that dominated further particle growth, resulting in a significant broadening of particle sizes.

Size dependent magnetic properties were determined for several particle sizes, with σ_{sat} values 73% of bulk values for 20 nm particles, further illustrating the high quality of particles produced using this method.

Though this system was designed for small scale reactions, it is amenable to scaling for enhanced product yield. Finally, we believe that the "Extended" LaMer mechanism outlined here can be widely applied to other thermolytic nanoparticle synthesis methods.

Chapter 8 – Concluding Remarks and Outlook

The principle objective of this body of work was to design a synthetic method that would allow systematic control of iron oxide nanoparticle size over a range in which its superparamagnetic properties would be applicable for use in biomedical applications. This goal was achieved by evaluating the existing thermolytic synthetic approaches and developing a novel method that represent a major advance in the quality of magnetite nanoparticle synthesis. The achievements of each task are summarized here:

The 'Hot Injection' Method Using Anhydrous Iron Oleate

An anhydrous synthesis of the iron(III) oleate compound was developed to remove the variability in the stoichiometry of the compound that cause irreproducibility in magnetite nanoparticle synthesis. The conventionally prepared iron(III) oleate compound is affected by the presence of minuscule quantities of atmospheric water that result in the formation of polymeric complexes. These complexes are subject to dissociation and loss of iron material during subsequent washing steps. The 'hot injection' method, e.g., the rapid addition of the anhydrous precursor to a heated solvent, was used to evaluate the resulting synthetic reproducibility attainable with the anhydrous compound. The anhydrous iron(III) oleate was mixed with oleic acid to make it amenable to injection, although the use of a coordinating solvent was later thought to effect the reproducibility of this approach. The role of oleic acid on the nucleation and growth was demonstrated in experiments in which the concentration of oleic acid in solution was varied.

Nucleation times and resulting particle sizes increased with increasing oleic acid concentration, while the size dispersity decreased. This study identified a new route to preparing stoichiometric iron(III) oleate and represented a crucial step to understanding the role of excess oleic acid in achieving size control in this system.

In Situ Generation of Iron Oleate for Synthesis of High Quality Iron Oxide Nanoparticles

In this study, we conclusively demonstrated the formation of iron(III) oleate in situ following the decomposition of $Fe(acac)_3$ in oleic acid through ex situ FTIR measurements over the course of a reaction. This method describes an novel route to producing iron(III) oleate using stoichiometric quantities of starting material. Spherical, 27 nm particles with 12% size dispersity were synthesized using this method. Further, it was demonstrated for this system that as-synthesized particles are composed of wüstite, a non-stoichiometric iron oxide that is not strongly magnetic. Conversion of the particles to magnetite was achieved by oxidation of the particles at moderate temperature under ambient conditions. Phase control of synthesized particles was demonstrated by enhanced magnetic saturation, measured to be 78% of bulk Fe_3O_4.

A Mechanism for Growth of Iron Oxide Nanoparticles with Narrow Shape and Size Dispersity

Using the same system described in the previous section, we showed that increasing the reaction temperature shortened the reaction time and greatly

improved the shape and size dispersity of the resulting particles. A transformation of particle shapes was observed after nucleation, from the kinetically preferred, faceted shape to a thermodynamically stable, spherical shape. 25.6 nm particles were formed with 7.4% size dispersity, representing a substantial improvement over the previous method. For the first time, a growth mechanism for the particles in this system was identified, which allows for control of reaction duration for synthesis of particles with optimal properties.

Exquisite Control of Particle Size Using the "Extended" LaMer Mechanism

A novel method was developed for the synthesis of magnetite nanoparticles using the continuous addition of iron(III) oleate to a heated solvent solution. The iron(III) oleate used in the synthesis was prepared in situ, provides stoichiometric control over starting materials that cannot be achieved using conventional methods. Continuous addition of the precursor allows a broad range of particles sizes to be reproducibly synthesized, with a demonstrated span of 10 – 25 nm for the system in which oleic acid was present in excess.

Future Outlook

The results presented here represent a substantial improvement over the state of the art of magnetite nanoparticle synthesis. The methods presented here produce relatively large quantities of magnetite nanoparticles to be produced (hundreds of milligrams), although the process is amenable to scaling to increase product yield. However, equally as important to the clinical deployment of the particles is

modification of the particle surface that will confer aqueous stability of the particles as well as functionality required for targeted delivery to cells/tissues of interest.

Appendix A. Molten Metal Bath

The high temperatures used for our reactions necessitated the development of a new heating source that could maintain a stable set point temperature for a relatively small (< 50 mL) reaction volume. For a reaction of this size, a heating mantle sized for a 100 mL flask would typically be used and coupled to a commercial PID temperature controller. A 100 mL capacity heating mantle has an 80W output, and requires maximum power to reach temperatures in excess of 300°C. Maintaining a stable reaction temperature at 350°C proved to be very challenging using the commercial controllers we tested, often resulting in large oscillations about the set point temperature. Considering that oleic acid boils at 360°C, large temperature fluctuations could not be tolerated, as they caused the reaction to boil over.

The device design presented here employs three cartridge heaters, with a combined output of 600W, a significant increase over the maximum power attainable using a heating mantle. A control loop minimizes the difference between the reaction temperature and the set point by making adjustments in the power delivered to the cartridge heaters The improved tunability of the PID control and power settings in this system through a custom designed National Instruments interface provides superior control of reaction temperature over the commercial standard.

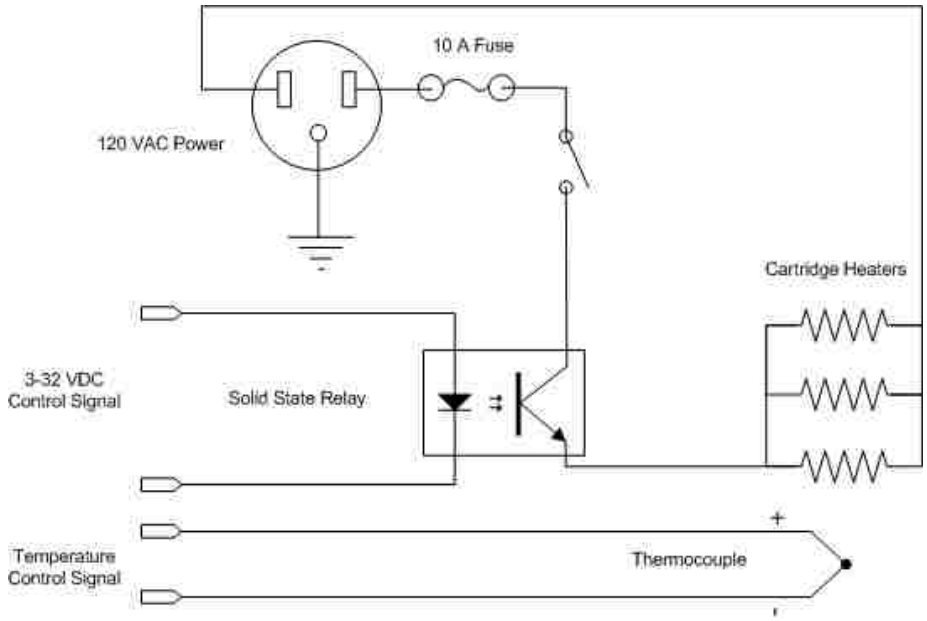

Figure A1-1. Schematic drawing of heating source used for molten metal bath. Three cartridge heaters deliver a combined 600W of power.

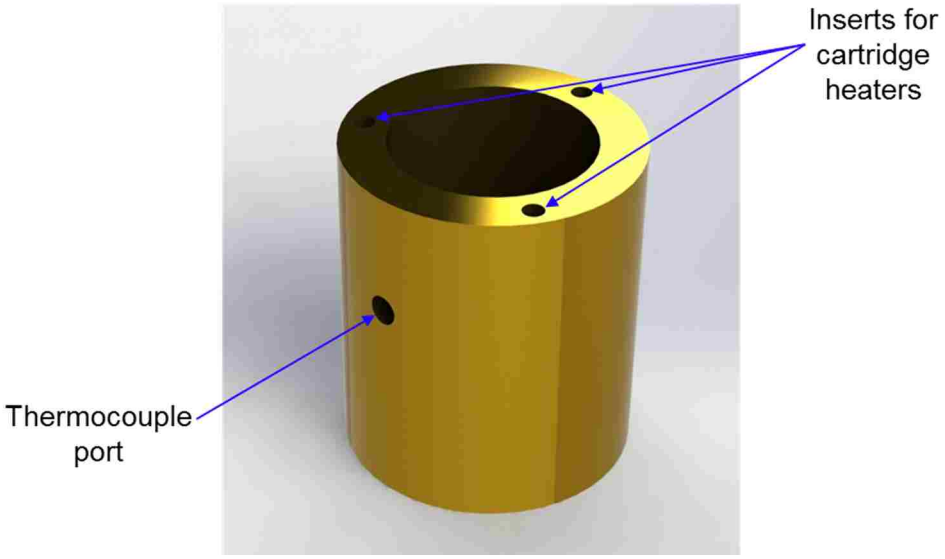

Figure A1-2. Brass heating block heated by three cartridge heaters. A low melting point alloy, Bolton 174F is contained within the core of block. The temperature of the alloy is measured with a thermocouple for feedback to the control software.

Figure A1-3. The heater block and electronics are contained within a metal housing with ports for temperature and software control.

Appendix B. Publications

Journal publications:

- E. C. Vreeland, G B. Schober, A. D. Price, T. C. Monson, N. Hudak, B. D. Fellows, R. L. Truby, and D. L. Huber, *In Situ Generation of Iron Oleate for Synthesis of High Quality Iron Oxide Nanoparticles*. Chem. Mater. Submitted.
- K. A. Homan, M. Souza, R. Truby, G. P. Luke, C. Green, E. Vreeland, and S. Emelianov, *Silver Nanoplate Contrast Agents for in Vivo Photoacoustic Imaging*. ACS Nano, 2011. **6**(1): p. 641 – 650.
- E. J. Cooley*, et al.*, *Evaluation of Arsenazo III as a Contrast Agent for Photoacoustic Detection of Micromolar Calcium Transients*, in Proc. SPIE, San Francisco, 2010, p. 75761J1 – 75761J8.

Articles in preparation:

- E. C. Vreeland, A. D. Price, G. B. Schober, B. D. Fellows, T. C. Monson, and D. L. Huber, *Size Tunable Iron Oxide Nanoparticle Synthesis Using the 'Extended LaMer' Method*.
- J. A. Crisp, E. C. Vreeland, S. A. Ivanov, and D. L. Huber, *Synthesis and Characterization of an Anhydrous Iron(III) Carboxylate: a Precursor to the Reproducible Synthesis of Iron Oxide Nanoparticles.*

Book chapter:

- K. Homan, S. Mallidi, E. Cooley, and S. Emelianov, *Combined Photoacoustic and Ultrasound Imaging of Metal Nanoparticles In Vivo*, in *Nanoimaging*, B. A. Goins and W. T. Phillips, Editors. 2011, Pan Stanford Publishing: Singapore.

Patent disclosures:

- T. C. Monson, J. M. Leger, E. C. Vreeland, *Low Temperature Synthesis of Dispersed Barium Titanate Nanoparticles*, U. S. Patent Application No. 61703345. Washington, DC: U.S. PTO, 2012.
- D.W. Branch, E. J. Cooley, G. T. Smith, C. D. James, J. M. McClain, *Microfluidic Device for Acoustic Cell Lysis*, U.S. Patent Application No. 872.919. Washington, DC: U.S. PTO, 2010.

REFERENCES

(1) Richards, R. M., Introduction to Nanotechnology. In *Nanoscale Materials in Chemistry*, 2nd ed.; Klabunde, K. J.; Richards, R. M., Eds. John Wiley & Sons, Inc.: Hoboken, 2009; pp 1-13.

(2) Whitesides, G. M., *Small* **2005,** *1*, (2), 172-179.

(3) Brinker, C. J.; Scherer, G. W., *Sol-gel science: the physics and chemistry of sol-gel processing*. Access Online via Elsevier: 1990; pp.

(4) Leutwyler, W. K.; Bürgi, S. L.; Burgl, H., *Science* **1996,** *271*, 933.

(5) Sun, S.; Murray, C. B.; Weller, D.; Folks, L.; Moser, A., *Science* **2000,** *287*, (5460), 1989-1992.

(6) Li, X.; Wang, X.; Xiong, Q.; Eklund, P. C., *Nano Lett.* **2005,** *5*, (10), 1982-1986.

(7) Huber, D. L., *Small* **2005,** *1*, (5), 482-501.

(8) Lieber, C. M., *MRS Bull.* **2003,** *28*, (07), 486-491.

(9) Watt, J.; Cheong, S.; Toney, M. F.; Ingham, B.; Cookson, J.; Bishop, P. T.; Tilley, R. D., *ACS Nano* **2009,** *4*, (1), 396-402.

(10) Ciuparu, D.; Lyubovsky, M. R.; Altman, E.; Pfefferle, L. D.; Datye, A., *Catalysis Reviews* **2002,** *44*, (4), 593-649.

(11) Calabrese Barton, S.; Gallaway, J.; Atanassov, P., *Chem. Rev.* **2004,** *104*, (10), 4867-4886.

(12) Krishna, S., *Infrared physics & technology* **2005,** *47*, (1), 153-163.

(13) Yavuz, C. T.; Mayo, J.; Suchecki, C.; Wang, J.; Ellsworth, A. Z.; D'Couto, H.; Quevedo, E.; Prakash, A.; Gonzalez, L.; Nguyen, C., *Environ. Geochem. Health* **2010,** *32*, (4), 327-334.

(14) Homan, K. A.; Souza, M.; Truby, R.; Luke, G. P.; Green, C.; Vreeland, E.; Emelianov, S., *ACS Nano* **2011,** *6*, (1), 641-650.

(15) Mirkin, C. A.; Letsinger, R. L.; Mucic, R. C.; Storhoff, J. J., *Nature* **1996,** *382*, (6592), 607-609.

(16) Whitesides, G. M., *Nat Biotech* **2003,** *21*, (10), 1161-1165.

(17) Wolf, L. K., Sweating the Small Stuff: Concerns Grow Over Nanoparticle Characterization and Purity. *Chem. Eng. News* May 28, 2012, 2012, pp 48-50.

(18) Baalousha, M.; Lead, J. R., *Nature nanotechnology* **2013,** *8*, (5), 308-309.

(19) Lead, J.; Holgate, S., *Nature nanotechnology* **2013,** *8*, (2), 72-72.

(20) Lopez-Serrano, A.; Olivas, R. M.; Landaluze, J. S.; Camara, C., *Analytical Methods* **2014,** *6*, (1), 38-56.

(21) Latorre, M.; Rinaldi, C., *PR Health Sciences Journal* **2009,** *28*, (3).

(22) Connolly, J.; St Pierre, T. G., *J. Magn. Magn. Mater.* **2001,** *225*, (1–2), 156-160.

(23) Häfeli, U., *Scientific and clinical applications of magnetic carriers*. Springer: 1997; pp.

(24) Adolphi, N. L.; Huber, D. L.; Jaetao, J. E.; Bryant, H. C.; Lovato, D. M.; Fegan, D. L.; Venturini, E. L.; Monson, T. C.; Tessier, T. E.; Hathaway, H. J.; Bergemann, C.; Larson, R. S.; Flynn, E. R., *J. Magn. Magn. Mater.* **2009,** *321*, (10), 1459-1464.

(25) Jillavenkatesa, A.; Dapkunas, S. J.; Lin-sien, H. L., NIST recommended practice guide special publication 960-1 Particle size characterization. In National Institute of Standards and Technology: 2001.

(26) Gilbert, R.; Hess, M.; JONES, R.; STEPTO, R., *Pure Appl. Chem* **2009,** *81*, (2), 351-353.

(27) de Carvalho, J. F.; de Medeiros, S. N.; Morales, M. A.; Dantas, A. L.; Carriço, A. S., *Appl. Surf. Sci.* **2013,** *275*, (0), 84-87.

(28) Ying, J. Y.; Sun, T., *J. Electroceram.* **1997,** *1*, (3), 219-238.

(29) Koch, C., *Annu. Rev. Mater. Sci.* **1989,** *19*, (1), 121-143.

(30) Leslie-Pelecky, D. L.; Rieke, R. D., *Chem. Mater.* **1996,** *8*, (8), 1770-1783.

(31) Mantovan, R.; Lamperti, A.; Georgieva, M.; Tallarida, G.; Fanciulli, M., *J. Phys. D: Appl. Phys.* **2010,** *43*, (6), 065002.

(32) Strobel, R.; Pratsinis, S. E., *Adv. Powder Technol.* **2009,** *20*, (2), 190-194.

(33) Iskandar, F., *Adv. Powder Technol.* **2009,** *20*, (4), 283-292.

(34) Kang, Y. C.; Park, S. B.; Kang, Y. W., *Nanostruct. Mater.* **1995,** *5*, (7-8), 777-791.

(35) Lu, A. H.; Salabas, E. L.; Schüth, F., *Angew. Chem. Int. Ed.* **2007,** *46*, (8), 1222-1244.

(36) Langevin, D., *Annu. Rev. Phys. Chem.* **1992,** *43*, (1), 341-369.

(37) Gupta, A. K.; Gupta, M., *Biomaterials* **2005,** *26*, (18), 3995-4021.

(38) Li, S.; Qin, T.; Gaowu, W.; Pei, W.; Ren, Y.; Zhang, Y.; Esling, C.; Zuo, L., *J. Am. Ceram. Soc.* **2009,** *92*, (3), 631-635.

(39) Pinna, N.; Grancharov, S.; Beato, P.; Bonville, P.; Antonietti, M.; Niederberger, M., *Chem. Mater.* **2005,** *17*, (11), 3044-3049.

(40) Duan, L.; Jia, S.; Wang, Y.; Chen, J.; Zhao, L., *Journal of Materials Science* **2009,** *44*, (16), 4407-4412.

(41) Li, D.; Jiang, D.; Chen, M.; Xie, J., *Mater. Lett.* **2010,** *64*, 2462 - 2464.

(42) Yu, W. W.; Falkner, J. C.; Yavuz, C. T.; Colvin, V. L., *Chem. Commun.* **2004**, (20), 2306-2307.

(43) Bronstein, L. M.; Atkinson, J. E.; Malyutin, A. G.; Kidwai, F.; Stein, B. D.; Morgan, D. G.; Perry, J. M.; Karty, J. A., *Langmuir* **2011**, 484-499.

(44) Park, J.; An, K.; Hwang, Y.; Park, J. G.; Noh, H. J.; Kim, J. Y.; Park, J. H.; Hwang, N. M.; Hyeon, T., *Nat. Mater.* **2004,** *3*, (12), 891-895.

(45) Kwon, S.; Piao, Y.; Park, J.; Angappane, S.; Jo, Y.; Hwang, N.; Park, J.; Hyeon, T., *J. Am. Chem. Soc.* **2007,** *129*, (41), 12571-12584.

(46) LaMer, V. K.; Dinegar, R. H., *J. Am. Chem. Soc.* **1950,** *72*, (11), 4847-4854.

(47) Cao, G.; Wang, Y., Zero-Dimensional Nanostructures: Nanoparticles. In *Nanostructures and Nanomaterials: Synthesis, Properties, and Applications*, 2nd ed.; World Scientific Publishing Co. Ptc. Ltd.: Hackensack, 2011; pp 61-141.

(48) Kwon, S. G.; Hyeon, T., Kinetics of Colloidal Chemical Synthesis of Monodisperse Spherical Nanocrystals. In *Nanoscale Materials in Chemistry*, John Wiley & Sons, Inc.: 2009; pp 127-153.

(49) Sugimoto, T., Chapter 1 - Nucleation. In *Monodispersed Particles*, Sugimoto, T., Ed. Elsevier: Amsterdam, 2001; pp 1-85.

(50) Sugimoto, T., Chapter 2 - Growth. In *Monodispersed Particles*, Sugimoto, T., Ed. Elsevier: Amsterdam, 2001; pp 86-117.

(51) Viswanatha, R.; Sarma, D. D., Growth of Nanocrystals in Solution. In *Nanomaterials Chemistry*, Rao, C. N. R.; Muller, A.; Cheetham, A. K., Eds. Wiley-VCH GmbH & Co. KGaA: Weinheim, 2007; pp 139-170.

(52) Lifshitz, I. M.; Slyozov, V. V., *J. Phys. Chem. Solids* **1961,** *19*, (1-2), 35-50.

(53) Wagner, C. Z., *Z. Elktrochem. Angew. P.* **1961,** *65*, 581-591.

(54) Livingston, J., *Trans. Met. Soc. AIME* **1959,** *215*, 566.

(55) Ardell, A. J.; Nicholson, R. B., *Acta Metall.* **1966,** *14*, (10), 1295-1309.

(56) Oskam, G.; Nellore, A.; Penn, R. L.; Searson, P. C., *The Journal of Physical Chemistry B* **2003,** *107*, (8), 1734-1738.

(57) Wong, E. M.; Bonevich, J. E.; Searson, P. C., *The Journal of Physical Chemistry B* **1998,** *102*, (40), 7770-7775.

(58) McCarty, J.; Malukhin, G.; Poojary, D.; Datye, A.; Xu, Q., *The Journal of Physical Chemistry B* **2005,** *109*, (6), 2387-2391.

(59) Xu, Q.; Kharas, K. C.; Croley, B. J.; Datye, A. K., *ChemCatChem* **2011,** *3*, (6), 1004-1014.

(60) Challa, S. R.; Delariva, A. T.; Hansen, T. W.; Helveg, S.; Sehested, J.; Hansen, P. L.; Garzon, F.; Datye, A. K., *J. Am. Chem. Soc.* **2011,** *133*, (51), 20672-20675.

(61) Sugimoto, T., *Adv. Colloid Interface Sci.* **1987,** *28*, (0), 65-108.

(62) Goldfarb, R. B.; Fickett, F. R., NBS Special Publication 696. In NBS, Ed. Boulder, 1985.

(63) Cullity, B. D.; Graham, C. D., *Introduction to Magnetic Materials*. Wiley-IEEE Press: 2009; pp 151-163.

(64) Jeong, U.; Teng, X.; Wang, Y.; Yang, H.; Xia, Y., *Adv. Mater.* **2007,** *19*, (1), 33-60.

(65) Laurent, S.; Forge, D.; Port, M.; Roch, A.; Robic, C.; Vander Elst, L.; Muller, R. N., *Chem. Rev.* **2008,** *108*, (6), 2064-2110.

(66) Brown, W. F., *Physical Review* **1963,** *130*, (5), 1677-1686.

(67) Néel, L., *C. R. Acad. Sci.* **1947,** *224*, 1488-1490.

(68) Cornell, R. M.; Schwertmann, U., Crystal Structure. In *The Iron Oxides: Structure, Properties, Reactions, Occurrence and Uses*, 2 ed.; WILEY-VCH GmbH & Co. KGaA: Weinheim, 2003; pp 9-38.

(69) Thapa, D.; Palkar, V.; Kurup, M.; Malik, S., *Mater. Lett.* **2004,** *58*, (21), 2692-2694.

(70) Walz, F., *J. Phys.: Condens. Matter* **2002,** *14*, (12), R285.

(71) Haneda, K.; Morrish, A., *Le Journal de Physique Colloques* **1977,** *38*, (C1), C1-321-C1-323.

(72) Butler, R. F.; Banerjee, S. K., *Journal of Geophysical Research* **1975,** *80*, (29), 4049-4058.

(73) Flynn, E. R.; Bryant, H. C.; Bergemann, C.; Larson, R. S.; Lovato, D.; Sergatskov, D. A., *J. Magn. Magn. Mater.* **2007,** *311*, (1), 429-435.

(74) Bryant, H.; Adolphi, N. L.; Huber, D. L.; Fegan, D. L.; Monson, T. C.; Tessier, T. E.; Flynn, E. R., *J. Magn. Magn. Mater.* **2011,** *323*, (6), 767-774.

(75) Wang, Y.-X.; Hussain, S.; Krestin, G., *European Radiology* **2001,** *11*, (11), 2319-2331.

(76) Simonsen, C. Z.; Østergaard, L.; Vestergaard-Poulsen, P.; Røhl, L.; Bjørnerud, A.; Gyldensted, C., *J. Magn. Reson. Imaging* **1999,** *9*, (2), 342-347.

(77) Adolphi, N. L.; Butler, K. S.; Lovato, D. M.; Tessier, T. E.; Trujillo, J. E.; Hathaway, H. J.; Fegan, D. L.; Monson, T. C.; Stevens, T. E.; Huber, D. L.; Ramu, J.; Milne, M. L.; Altobelli, S. A.; Bryant, H. C.; Larson, R. S.; Flynn, E. R., *Contrast Media Mol. Imaging* **2012,** *7*, (3), 308-319.

(78) Adolphi, N. L.; Huber, D. L.; Bryant, H. C.; Monson, T. C.; Fegan, D. L.; Lim, J. K.; Trujillo, J. E.; Tessier, T. E.; Lovato, D. M.; Butler, K. S., *Phys. Med. Biol.* **2010,** *55*, 5985.

(79) Flynn, E.; Bryant, H., *Phys. Med. Biol.* **2005,** *50*, (6), 1273.

(80) Jaetao, J. E.; Butler, K. S.; Adolphi, N. L.; Lovato, D. M.; Bryant, H. C.; Rabinowitz, I.; Winter, S. S.; Tessier, T. E.; Hathaway, H. J.; Bergemann, C., *Cancer Research* **2009,** *69*, (21), 8310.

(81) Guardia, P.; Pérez, N.; Labarta, A.; Batlle, X., *Langmuir* **2009,** *26*, (8), 5843-5847.

(82) Park, J.; Lee, E.; Hwang, N. M.; Kang, M.; Kim, S. C.; Hwang, Y.; Park, J. G.; Noh, H. J.; Kim, J. Y.; Park, J. H., *Angew. Chem.* **2005,** *117*, (19), 2932-2937.

(83) Bronstein, L.; Huang, X.; Retrum, J.; Schmucker, A.; Pink, M.; Stein, B.; Dragnea, B., *Chem. Mater.* **2007,** *19*, (15), 3624-3632.

(84) Guardia, P.; Pérez-Juste, J.; Labarta, A.; Batlle, X.; Liz-Marzán, L. M., *Chem. Commun.* **2010,** *46*, (33), 6108-6110.

(85) Pavia, D. L.; Lampmann, G. M.; Kriz, G. S., *Introduction to Spectroscopy*. 3 ed.; Thompson Learning, Inc.: 2001; pp 415.

(86) Bragg, S. W. H.; Bragg, S. W. L., *X rays and Crystal Structure*. G. Bell and Sons, Ltd.: London, 1915; pp 229.

(87) Kittel, C., *Introduction to Solid State Physics*. 7 ed.; John Wiley & Sons, Inc.: Hoboken, 1996; pp 688.

(88) Langford, J. I.; Wilson, A. J. C., *J. Appl. Crystallogr.* **1978,** *11*, (2), 102-113.

(89) Sasaki, A., *The Rigaku Journal* **2005,** *22*, (1), 31-38.

(90) McElfresh, M., Fundamentals of Magnetism and Magnetic Measurements. In Quantum Design: 1994.

(91) Varma, R.; Bhargava, H., *Rev. Roum. Chim.* **1979,** *24*, (4), 537-542.

(92) Roca, A. G.; Morales, M. P.; O'Grady, K.; Serna, C. J., *Nanotechnology* **2006,** *17*, (11), 2783.

(93) Shavel, A.; Rodríguez-González, B.; Spasova, M.; Farle, M.; Liz-Marzán, L. M., *Advanced Functional Materials* **2007,** *17*, (18), 3870-3876.

(94) Halbreich, A.; Roger, J.; Pons, J. N.; Geldwerth, D.; Da Silva, M. F.; Roudier, M.; Bacri, J. C., *Biochimie* **1998,** *80*, (5–6), 379-390.

(95) Pankhurst, Q. A.; Pollard, R. J., *Journal of Physics: Condensed Matter* **1993,** *5*, (45), 8487.

(96) Shavel, A.; Rodríguez-González, B.; Spasova, M.; Farle, M.; Liz-Marzán, L. M., *Adv. Funct. Mater.* **2007,** *17*, (18), 3870-3876.

(97) Sun, S.; Zeng, H., *J. Am. Chem. Soc.* **2002,** *124*, (28), 8204-8205.

(98) Roca, A.; Morales, M.; O'Grady, K.; Serna, C., *Nanotechnology* **2006,** *17*, (11), 2783.

(99) Dzhardimalieva, G.; Pomogailo, A. D., *Russ. Chem. Rev.* **2008,** *77*, 259.

(100) Lu, Y.; Miller, J. D., *J. Colloid Interface Sci.* **2002,** *256*, (1), 41-52.

(101) Earnshaw, A.; Figgis, B.; Lewis, J., *J. Chem. Soc. A* **1966**, 1656-1663.

(102) Catterick, J.; Thornton, P.; Fitzsimmons, B. W., *J. Chem. Soc., Dalton Trans.* **1977**, (15), 1420-1425.

(103) Murray, C.; Norris, D.; Bawendi, M. G., *J. Am. Chem. Soc.* **1993,** *115*, (19), 8706-8715.

(104) Murray, C. B.; Kagan, C.; Bawendi, M., *Annu. Rev. Mater. Sci.* **2000,** *30*, (1), 545-610.

(105) Park, J.; Joo, J.; Kwon, S. G.; Jang, Y.; Hyeon, T., *Angew. Chem. Int. Ed.* **2007,** *46*, (25), 4630-4660.

(106) de Mello Donegá, C.; Liljeroth, P.; Vanmaekelbergh, D., *Small* **2005,** *1*, (12), 1152-1162.

(107) Qi, B.; Ye, L.; Stone, R.; Dennis, C.; Crawford, T. M.; Mefford, O. T., *J. Phys. Chem. C* **2013,** *117*, (10), 5429-5435.

(108) Bronstein, L. M.; Huang, X.; Retrum, J.; Schmucker, A.; Pink, M.; Stein, B. D.; Dragnea, B., *Chemistry of Materials* **2007,** *19*, (15), 3624-3632.

(109) Cornell, R. M.; Schwertmann, U., Characterization. In *The Iron Oxides: Structure, Properties, Reactions, Occurences and Uses*, 2nd ed.; Wiley-VCH Verlag GmbH & Co. KGaA: Weinheim, 2003; pp 139-183.

(110) Roeges, N. P. G., Normal Vibrations and Absorption Regions of CX_3. In *A Guid to the Complete Interpretation of Infrared Spectra of Organic Structures*, John Wiley & Sons: Chichester, 1998; pp 10-47.

(111) Roeges, N. P. G., Normal Vibrations and Absorption Regions of Oxy Compounds. In *A Guide to the Complete Interpretation of Infrared Spectra of Organic Structures*, John Wiley & Sons: Chichester, 1998; pp 258-276.

(112) Roeges, N. P. G., Normal Vibrations and Absorption Regions of C(=X)Y. In *A Guide to the Complete Interpretation of Infrared Spectra of Organic Structures*, John Wiley & Sons: Chichester, 1998; pp 137-203.

(113) Pankhurst, Q. A.; Connolly, J.; Jones, S.; Dobson, J., *J. Phys. D: Appl. Phys.* **2003,** *36*, R167.

(114) Hou, Y.; Xu, Z.; Sun, S., *Angew. Chem.* **2007,** *119*, (33), 6445-6448.

(115) Huang, J. H.; Parab, H. J.; Liu, R. S.; Lai, T. C.; Hsiao, M.; Chen, C. H.; Sheu, H. S.; Chen, J. M.; Tsai, D. P.; Hwu, Y. K., *J. Phys. Chem. C* **2008,** *112*, (40), 15684-15690.

(116) Redl, F. X.; Black, C. T.; Papaefthymiou, G. C.; Sandstrom, R. L.; Yin, M.; Zeng, H.; Murray, C. B.; O'Brien, S. P., *J. Am. Chem. Soc.* **2004,** *126*, (44), 14583-14599.

(117) Rasband, W. S. *ImageJ*, U. S. National Institutes of Health: Bethesda, 1997 - 2012.

(118) ASTM, Standard test method for iron in trace quantities using the 1,10-phenanthroline method. In *ASTM Standard E394 - 09*, West Conshohocken, PA, 2000.

(119) Huber, D. L.; Venturini, E. L.; Martin, J. E.; Provencio, P. P.; Patel, R. J., *J. Magn. Magn. Mater.* **2004,** *278*, (3), 311-316.

(120) Kwon, S. G.; Hyeon, T., *Small* **2011,** *7*, (19), 2685-2702.

(121) Shevchenko, L. L., *Russ. Chem. Rev.* **1963,** *32*, (4), 201.

(122) Deacon, G. B.; Phillips, R. J., *Coord. Chem. Rev.* **1980,** *33*, (3), 227-250.

(123) Ismail, H. M., *J. Anal. Appl. Pyrolysis* **1991,** *21*, (3), 315-326.

(124) Slabzhennikov, S. N.; Ryabchenko, O. B.; Kuarton, L. A., *Russ. J. Coord. Chem.* **2003,** *29*, (7), 484-488.

(125) Pérez, N.; López-Calahorra, F.; Labarta, A.; Batlle, X., *PCCP* **2011,** *13*, (43), 19485-19489.

(126) Lak, A.; Ludwig, F.; Scholtyssek, J. M.; Dieckhoff, J.; Fiege, K.; Schilling, M., *Magnetics, IEEE Transactions on* **2013,** *49*, (1), 201-207.

(127) Watt, J.; Young, N.; Haigh, S.; Kirkland, A.; Tilley, R. D., *Adv. Mater.* **2009,** *21*, (22), 2288-2293.

(128) Cheong, S.; Watt, J. D.; Tilley, R. D., *Nanoscale* **2010,** *2*, (10), 2045-2053.

(129) Guardia, P.; Batlle-Brugal, B.; Roca, A.; Iglesias, O.; Morales, M.; Serna, C.; Labarta, A.; Batlle, X., *J. Magn. Magn. Mater.* **2007,** *316*, (2), e756-e759.

(130) Berry, C., *Photographic Science and Engineering* **1976,** *20*, (1), 1-4.

(131) Sugimoto, T., *J. Colloid Interface Sci.* **1992,** *150*, (1), 208-225.

(132) Goya, G. F.; Berquo, T. S.; Fonseca, F. C.; Morales, M. P., *J. Appl. Phys.* **2003,** *94*, (5), 3520-3528.

(133) Berkowitz, A. E.; Lahut, J. A.; Jacobs, I. S.; Levinson, L. M.; Forester, D. W., *Phys. Rev. Lett.* **1975,** *34*, (10), 594-597.

(134) Kodama, R. H.; Berkowitz, A. E.; McNiff, J. E. J.; Foner, S., *Phys. Rev. Lett.* **1996,** *77*, (2), 394-397.